UC Berkeley
UC Berkeley Electronic Theses and Dissertations

Title

Shining a Light on Plasmonic Photoelectrochemical Carbon Dioxide Reduction

Permalink

https://escholarship.org/uc/item/8f77c696

Author

Creel, Erin

Publication Date

2019

Peer reviewed|Thesis/dissertation

Shining a Light on Plasmonic Photoelectrochemical Carbon Dioxide Reduction

By

Erin B. Creel

A dissertation submitted in partial satisfaction of the

requirements for the degree of

Doctor of Philosophy

in

Chemistry

in the

Graduate Division

of the

University of California, Berkeley

Committee in charge:

Professor Bryan D. McCloskey, Co-chair
Professor Richard Saykally, Co-chair
Professor Peidong Yang
Professor Alexis T. Bell

Summer 2019

Shining a Light on Plasmonic Photoelectrochemical Carbon Dioxide Reduction

Abstract

Shining a Light on Plasmonic Photoelectrochemical Carbon Dioxide Reduction

by

Erin B. Creel

Doctor of Philosophy in Chemistry

University of California, Berkeley

Professor Bryan D. McCloskey, Co-chair

Professor Richard J. Sakyally, Co-chair

Electrochemical carbon dioxide (CO_2) reduction is one possible component of the effort to mitigate atmospheric CO_2 concentration and develop a reliable renewable fuel source. However, CO_2 reduction suffers from the high overpotentials needed to overcome sluggish kinetics, low selectivity for desired products, and unfavorable competition with water reduction (hydrogen evolution reaction (HER)). Challenges limiting energy efficiency and selective product formation must be addressed to make CO_2 reduction a viable energy storage solution.

Plasmonic catalysis may bypass the shortcomings in traditional "dark" catalysis for multi-electron reductions because of its ability to couple light energy into surface chemistry. Surface plasmon resonance (SPR) in nanostructured metals has been shown to increase reaction rates or alter selectivity in a variety of reactions, including gas-phase CO_2 reduction. However, the effect of SPR on the coulombic efficiency and selectivity of electrochemical CO_2 reduction product(s) has not been extensively explored despite the promising improvements in selectivity seen in purely plasmonic photocatalytic (without voltage bias) CO_2 reduction. In this dissertation, I explore the effect of SPR on aqueous electrochemical CO_2 reduction.

Incorporating illumination into any electrochemical system poses electrochemical cell geometry and temperature regulation challenges. In order to promote experiment reproducibility and enable direct comparison of photoelectrochemistry (PEC) studies across various laboratories, I outline a few best practices. The temperature of the electrochemical cell affects not only the reaction rate but also reaction selectivity in reactions with multiple products, and illumination may increase the temperature of the electrochemical cell components dramatically. Thus, the temperature of the electrochemical cell must either be regulated or reported. The materials, electrolyte, and path length from the surface to the photoelectrode vary between PEC cells. Each of these factors influences the light attenuation, necessitating that the light flux be measured at the surface of the photoelectrode so that conditions can be repeated in different cells. Additionally, a careful comparison of the photoelectrode before and after PEC is required for adequate stability characterization because both photoexcitation and applied voltage can affect the composition and morphology of materials.

1

Incorporating illumination into an electrochemical carbon dioxide reduction (CO_2R) system poses additional challenges due to the requirements of supplying a gas (CO_2) to the reaction vessel and detecting trace amounts of both gaseous and soluble products. Parallel electrodes reduce the potential gradients across their surfaces, front illumination of the photoelectrode allows more photoexcited charge carriers to reach the electrtrochemically active surface, small catholyte and anolyte volumes allows decreased electrolysis times necessary to detect trace soluble products, continuous CO_2 sparging maintains CO_2 saturation of the electrolyte and carries evolved gaseous products to an in-line gas chromatograph (GC), a temperature control system maintains a constant catholyte temperature so that the effects of temperature and illumination can be decoupled, a membrane separating the catholyte and anolyte to prevent soluble CO_2R products from being oxidized at the anode. The CO_2R product distribution and current density of silver foil electrodes is indistinguishable between this PEC cell and a conventional compression electrochemical CO_2R cell.

The newly developed front-illumination electrochemical CO_2R cell allows for the full characterization of the electrochemical CO_2R performance of an illuminated and unilluminated electron-beam-deposited thin film polycrystalline silver electrode. The as-deposited electrode increases in absorption, decreases in elctrochemical surface area (ECSA), and broadens in particle size distribution over 45 min of elctrochemical CO_2R, but these properties are then stable for hours of CO_2R. The electrode exhibits a SPR absorption peak at 351 nm and was illuminated with a 365 nm light-emitting diode (LED). At small applied overpotentials (-0.8 to -0.6 Volts versus the reversible hydrogen electrode (V_{RHE})), illuminating the thin film Ag electrode increases the production rate of carbon monoxide (CO) and decreases the hydrogen (H_2) production rate. This may be the first time that one reaction is enhanced while another is simultaneously suppressed by a plasmonic effect. Illuminating the Ag electrode decreases the overpotential required to generate CO selectively. The plasmonic effect suppresses the total reaction rate when the electrolyte is saturated with inert Ar rather than CO_2. This may be the first electrochemical reaction that is suppressed through a photoeffect. The CO_2 reduction product that is promoted with plasmon excitation depends on the applied voltage. At larger cathodic potentials (-1.1 to -0.8 V_{RHE}), methanol and formate production rates are increased while CO and H_2 production rates remain the same. This is the first demonstration of potential-dependent selectivity in any plasmon-enhanced reaction. The photoeffect is proportional to absorption and scales linearly with light intensity, two strong indicators that the activity is photonic rather than thermal in nature.

The nanofeatures on the silver thin film electrode are not intentionally controlled, but it still exhibited remarkable photoactivity and selectivity for CO_2R. Perhaps if the nanofeatures were rationally designed with specific sizes, shapes, and compositions, the photoactivity could be increased or the selectivity altered. Solution-based, electrochemical, and lithographic approaches to nanosynthesis are explored for creating nanopatterned electrodes. Though nanofeature-modified electrode stability has limited the investigation of these well-defined photoelectrodes, there may be additional strategies that have not yet been explored for stabilization.

There is still more work needed to understand the mechanism for plasmon-enhanced electrochemical CO_2R and increase the energy efficiency of plasmonic CO_2R, but this work clearly demonstrates the unique selectivity achievable through the combination of plasmonics

and electrochemistry. Plasmonics may also be a valuable tool in other multi-electron, multi-product electrochemical reactions such as nitrogen (N_2) reduction.

To my husband, Andy

Contents

Acknowledgements

A very special thank you to my husband, Andy Creel, for learning about plasmons, accompanying me on wacky adventures, being a shoulder to lean on and an ear to confide in, and his eternal love and support.

I would like to acknowledge the support of my family in my educational endeavors from pre-K through the 22nd grade. Thank you to my mom, Lesa Brahm, for fostering my love of learning and being a strong, intelligent female role model. Thank you to my dad, Steven Brahm, for encouraging me to "go all out" in everything I do and always believing in my ability to do and achieve more. Thank you to my brother Christopher Brahm for teaching me to find the joy in every situation and to express myself clearly and creatively. Thank you to my brother James Brahm for all the little things such as his support of my marriage and graduate school career, history lessons, and computer coding assistance. Thank you to my grandparents, Jim annd JoAnn Brahm, for teaching me the value of hard work, always believing in my potential, and keeping me company via phone calls on my walks or bus rides around Berkeley.

Thank you to my advisor, Bryan McCloskey, for his scientific guidance and mentorship, advocacy on my behalf, and seeing my Ph.D. potential even in my lowest moments of graduate school. I literally would not have made it through graduate school without his support. Thank you also to my other advisors—Raffaella Buonsanti, Robert Kostecki, Rich Saykally, and Jeffrey J. Urban—for their support in my Ph.D.

Thank you to Elizabeth Corson for teaching me about gas plumbing, her dedication to data organization, being a wonderful partner in science (experiments, writing, and presentations), giving me rides home, and for being a great friend.

Many thanks to "my undergrad," Davis Perez, for his eternal optimism and enthusiasm for all science, gluing skills, tolerance of my music, life discussions, and especially reaching items in high places.

Thank you to Team BLAGS (Alex Aaring, Andy Creel, Matthew Kolaczkowski, Lauren Nowak, and Iris Young) for enduring friendship, tons of puns, enlightening discussions, incredible patience, and following Giggles to the moon!

Thank you to my past and present BASIS team, the Steering Committee members, and the CRS staff for their shared love and enthusiasm for science outreach.

I would like to thank my undergraduate advisors and mentors for setting me on my path to become a professional scientist. Thank you to Dr. Todd Deutch for exposing me to photoelectrochemistry and modeling how to be triply dedicated to science, saving the world, and family. Thank you to Dr. Robert Bachman for encouraging and enabling me to pursue chemistry research and to all the chemistry professors at Sewanee for encouraging me to

pursue graduate school and giving me the tools to be successful once there.

Thank you to many wonderful teachers—especially Judy Manlove, Jan Herman, and Lady Emrich—who have challenged me academically, instilled a lifelong love of learning, and opened my eyes to the wonders of science.

List of Figures

List of Tables

List of Symbols

Notation	Description	Page List
ΔG	Gibss free energy change	3
Ω	Ohm (unit of electrical resistance)	55
C_2H_4	ethylene	2–4, 33, 37
C_2H_6	ethane	37
CH_3CH_2OH	ethanol	2–4
CH_3OH	methanol	2–4
CH_4	methane	1–4, 33, 37
$E°$	standard electrochemical reduction potential	2, 3
e^-	electron	3
E_F	Fermi level energy	10, 13, 65
E_a	activation energy	3
F	Faraday's constant, 96485 C mol^{-1}	3, 57
H^+	proton	2, 3
H_2SO_4	sulfuric acid	20
$HCOO^-$	formate (deprotonated formic acid)	3, 4
HCOOH	formic acid	2, 3
K_2CO_3	potassium carbonate	18, 35, 46, 49, 55, 56, 71–75, 77–80, 90
$KHCO_3$	potassium bicarbonate	20, 31–35, 42, 46, 54, 55, 72
$NaClO_4$	sodium perchlorate	46, 49, 56

Notation	Description	Page List
pH	$-\log[\mathrm{H}^+]$	2, 5, 35, 41, 46, 55

Acronyms

Notation	Description	Page List
^{1}H NMR	proton nuclear magnetic resonance	23, 37, 44, 57, 58
AFM	atomic force microscopy	22, 42, 44, 45, 55
AP-XPS	ambient pressure x-ray photoelectron spectroscopy	21
ATR	attenuated total reflectance	92, 93
CA	chronoamperometry	71–73, 77, 79, 87
CO_2R	carbon dioxide reduction	1–6, 17, 22–25, 32, 34, 36–38, 47, 48, 62, 72, 79–81, 83, 89, 91–93
CPU	central processing unit	25, 56
CTAB	cetyltrimethylammonium bromide	62, 63
CV	cyclic voltammetry	42, 46, 56, 58, 72, 87
DFT	density functional theory	3–5
DIET	desorption induced by electronic transitions	46, 91
DMSO	dimethyl sulfoxide	57, 58
e-beam	electron beam	41, 54, 72–74, 81, 82, 84, 86
EC	electrochemistry	17, 26, 31–33, 35, 91

Notation	Description	Page List
ECSA	elctrochemical surface area	2, 21, 42–44, 58, 88
EQE	external quantum efficiency	18, 19
FDTD	finite-difference time-domain	15, 82, 83
FEP	fluorinated ethylene propylene	35
FID	flame ionization detector	37, 39, 56
FT	Fourier transform	92, 93
FWHM	full width at half maximum	10
GC	gas chromatograph	2, 23, 24, 26, 31, 35–39, 44, 56, 57
GC-MS	gas chromatograph - mass spectrometer	26
HER	hydrogen evolution reaction	1, 2, 40, 41, 46, 53, 89, 91, 92
HETP	height equivalent of a theoretical plate	37
IL-TEM	identical location transmission electron microscopy	21
IQE	internal quantum efficiency	18, 19, 22
IR	infrared	19, 92, 93
LED	light-emitting diode	2, 29, 36, 39, 44, 49, 51–53, 56, 90
LSV	linear sweep voltammetry	18, 73–80, 88, 89
MFC	mass flow controller	35
MFM	mass flow meter	35
MS	mass spectrometer	26
NIR	near-infrared	55
NIST	National Institute of Standards and Technology	55, 57
OCV	open circuit voltage	71
PC	photochemistry	17, 59

Notation	Description	Page List
PEC	photoelectrochemistry	1, 2, 17, 19, 21–36, 74, 76, 77, 79, 80, 89, 91, 93
PEEK	polyether ether ketone	26, 55
PEM-FC	polymer electrolyte membrane fuel cell	21
PID	proportional-integral-derivative	18, 26, 27, 29, 35, 36, 56
RDS	rate determining step	3
RMS	root mean square	44
RTD	resistance temperature detector	29
S/V	electrode surface area to electrolyte volume ratio	23, 24, 26
SAM	self-assembled monolayer	74, 76
SCCM	standard cubic centimeters per minute	24, 32, 35, 56
SEM	scanning electron microscopy	22, 42, 44, 55, 70, 71, 87
SERS	surface-enhanced Raman spectroscopy	92, 93
SHE	standard hydrogen electrode	2
SPR	surface plasmon resonance	1, 2, 6–8, 11–16, 40, 46, 53, 59
STM	scanning tunneling microscopy	21
TCD	thermal conductivity detector	37–39, 56
TEC	thermoelectric cooler	35
TEM	transmission electron microscope	21, 22, 63–68
TMS	tetramethylsilane	58
TNI	transient negative ion	46, 50, 91
UV	ultraviolet	19, 40, 42, 55, 67, 69, 80, 88

Notation	Description	Page List
V_{RHE}	Volts versus the reversible hydrogen electrode	2, 6, 30, 32–34, 39, 41, 42, 44–46, 50–54, 71–74, 76, 77, 79, 80, 88
XPS	x-ray photoelectron spectroscopy	55

Chapter 1

Introduction

Anthropogenic emissions of greenhouse gases, primarily carbon dioxide (CO_2), since the mid 18th century have increased the atmospheric concentration of CO_2, methane (CH_4), and nitrous oxide (N_2O) gases to the highest levels in the last 800,000 years. The largest source of greenhouse gas emissions is the burning of fossil fuels (coal, oil, and natural gas). The increased concentration of greenhouse gases has increased the total radiative forcing, colloquially known as the greenhouse effect, of the global energy system. The resulting increase in the energy trapped on Earth has lead to observations of increased air and ocean temperatures, decreased snow and ice cover, higher rates of sea level rise, and acidification of the ocean.[1]

As the problems with climate change become more evident, the push for energy technologies that have zero carbon emissions at the energy production source grows. Solar photovoltaics and wind turbines, the two most popular of these zero-emission technologies, suffer from a severe downside: they both use intermittent energy sources whose electricity supply profile does not match the energy demand profile. This engenders the need for emission-free energy storage technologies such as water electrolysis, large batteries, pumped hydro, thermal, and CO_2 reduction to capture excess energy production for a time when the supply does not meet the electricity demand. The latter method, CO_2 reduction, actually has a negative carbon footprint because CO_2 is consumed in the process. While there are several methods of CO_2 reduction, this work will focus on aqueous heterogeneous catalysis of (photo)electrochemical CO_2 reduction.

1.1   Electrochemical CO_2 Reduction

The basic premise of aqueous (photo)electrochemical CO_2 reduction is that electricity (and sunlight) are used to convert CO_2 and water (H_2O) to chemical fuels or feedstocks in a (photo)electrochemical cell (Figure 1.1). In aqueous heterogeneous electrochemical CO_2 reduction (henceforth referred to as simply "carbon dioxide reduction (CO_2R)"), electrical energy drives electrons from the cathode in an electrochemical cell to CO_2 molecules dissolved in a water-based, ionically conducting electrolyte. To provide a source of electrons for CO_2R, electrical energy also drives an oxidation reaction, typically oxygen evolution from water, at the interface between the electrolyte and the anode. The more than sixteen possible products
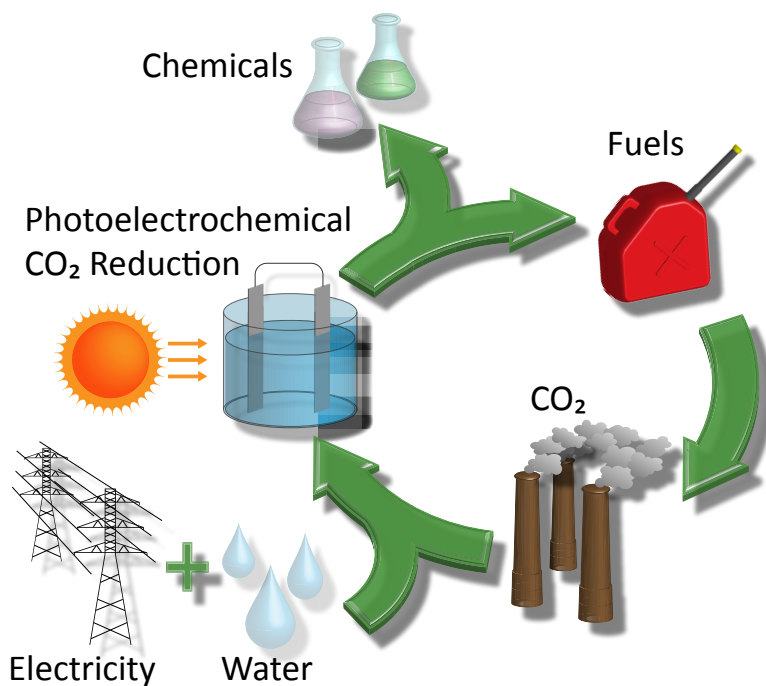
Figure 1.1: Carbon loop of photoelectrochemical CO$_2$ reduction. In photoelectrochemical CO$_2$ reduction, waste CO$_2$ (e.g. from flue gas or atmospheric capture) is reduced in an electrochemical cell using energy inputs of electricity and sunlight to make chemical feedstocks or carbon-based fuels that can be burned again to release CO$_2$ to begin the cycle again.

of the CO$_2$R reaction in water include gaseous products such as carbon monoxide (CO), methane (CH$_4$), and ethylene (C$_2$H$_4$) and liquid products such as formic acid (HCOOH), methanol (CH$_3$OH), and ethanol (CH$_3$CH$_2$OH).[2,3] For any product, the general CO$_2$R reaction is

$$x\text{CO}_2 + \frac{y}{2}\text{H}_2\text{O} \rightarrow \text{C}_x\text{H}_y\text{O}_z + \frac{2x + y/2 - z}{2}\text{O}_2 \tag{1.1}$$
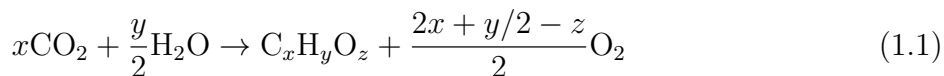
The major challenges of CO$_2$R in aqueous electrolyte are curtailing hydrogen evolution reaction (HER)—an unwanted side reaction—, improving energy efficiency, increasing CO$_2$ utilization, and achieving selectivity toward a desirable product. Suppressing HER is challenging because water, the source of protons (H$^+$) in CO$_2$R, is present at much higher concentrations than CO$_2$. The mole fraction of CO$_2$ in water in equilibrium with 1 atm partial pressure of CO$_2$ is 7×10^{-4}.[4] Even when high current rates or increasing pH force HER to occur by water reduction rather than proton reduction,[5] the large excess of water has a probabilistic advantage in the competition with CO$_2$ for surface sites on the cathode. Additionally, the reduction of H$^+$ to H$_2$ occurs at a similar thermodynamic potential as the reduction of CO$_2$. The electrochemical half reactions for common CO$_2$R products and for HER are listed in Equation 1.2 along with their standard reduction potentials ($E°$) relative to the standard hydrogen electrode (SHE) in water at pH = 0 at 25 °C.[6]

Carbon monoxide:	$CO_2 + 2\,(H^+ + e^-) \rightarrow CO + H_2O$	$E^\circ = -0.104$
Formic acid:	$CO_2 + 2\,(H^+ + e^-) \rightarrow HCOOH$	$E^\circ = -0.181$
Formaldehyde:	$CO_2 + 4\,(H^+ + e^-) \rightarrow HCHO + H_2O$	$E^\circ = -0.142$
Methanol:	$CO_2 + 6\,(H^+ + e^-) \rightarrow CH_3OH + H_2O$	$E^\circ = 0.016$
Methane:	$CO_2 + 8\,(H^+ + e^-) \rightarrow CH_4 + 2\,H_2O$	$E^\circ = 0.169$ (1.2)
Ethanol:	$2CO_2 + 12\,(H^+ + e^-) \rightarrow CH_3CH_2OH + 3\,H_2O$	$E^\circ = 0.084$
Ethylene:	$2\,CO_2 + 12\,(H^+ + e^-) \rightarrow C_2H_4 + 4\,H_2O$	$E^\circ = 0.079$
Hydrogen:	$2\,(H^+ + e^-) \rightarrow H_2$	$E^\circ = 0$
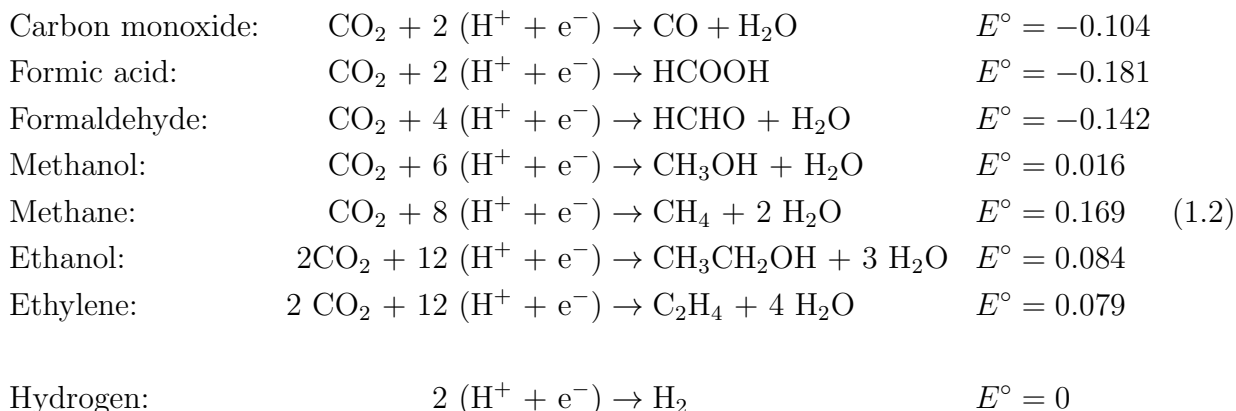
where the Gibbs free energy change (ΔG) of the reaction is

$$\Delta G^\circ = -n\mathrm{F}E^\circ \tag{1.3}$$

n is the number of electrons involved in the reaction, and $^\circ$ indicates standard conditions (25 °C, 1 atm, 1 M concentration). Achieving selectivity among these products in challenging because all of the CO_2R reactions have a standard reduction potential between -0.2 and 0.2 V. Many CO_2R reactions not only share similar thermodynamics but also share kinetic similarities with a common rate determining step (RDS) in the reaction mechanism.

1.1.1 CO_2 Reduction Mechanisms

Knowing the CO_2R mechanism including key intermediates and the energetics of each step can give valuable insights into how to alter the reaction selectivity. Insights into the mechanism can be gained from a variety of studies such as product analysis with different reactants, DFT, and isotope labeling. Proposed reaction pathways for several CO_2R products are shown in Figure 1.2. All the products depicted in Figure 1.2 except formate ($HCOO^-$) share the carbonyl species ($*{=}CO$) as a common intermediate. One of the main reasons for low selectivity for many-electron reduction products is that the proton and electron transfer to surface adsorbed CO to form CHO is the RDS, the step with the highest activation energy (E_a).[7,8] All subsequent steps are energetically downhill. Thus, it is difficult to selectively promote one of these subsequent steps over the others.

Evidence for the formation of CHO being the RDS includes DFT calculations and the co-production of the products that share this RDS. DFT calculations performed at a simulated constant potential using an explicit solvent approach predict the lowest energy intermediates and the energetic barriers between them. The DFT-predicted free energy landscape for reduction of CO_2 to CH_4 on a Cu(2 1 1) surface has the highest energy barrier for formation of CHO (Figure 1.3). Hydrogenation of adsorbed CO is also predicted to have the highest energy barrier in the reduction of CO_2 to ethylene. For both formic acid and CO production, the mechanistic step with the greatest overpotential is predicted to be the formation of a carboxyl species (frame 2 in Figure 1.3) through adsorption of CO_2 and a proton-electron pair. Formic acid is produced by adding a second proton-electron pair to the adsorbed
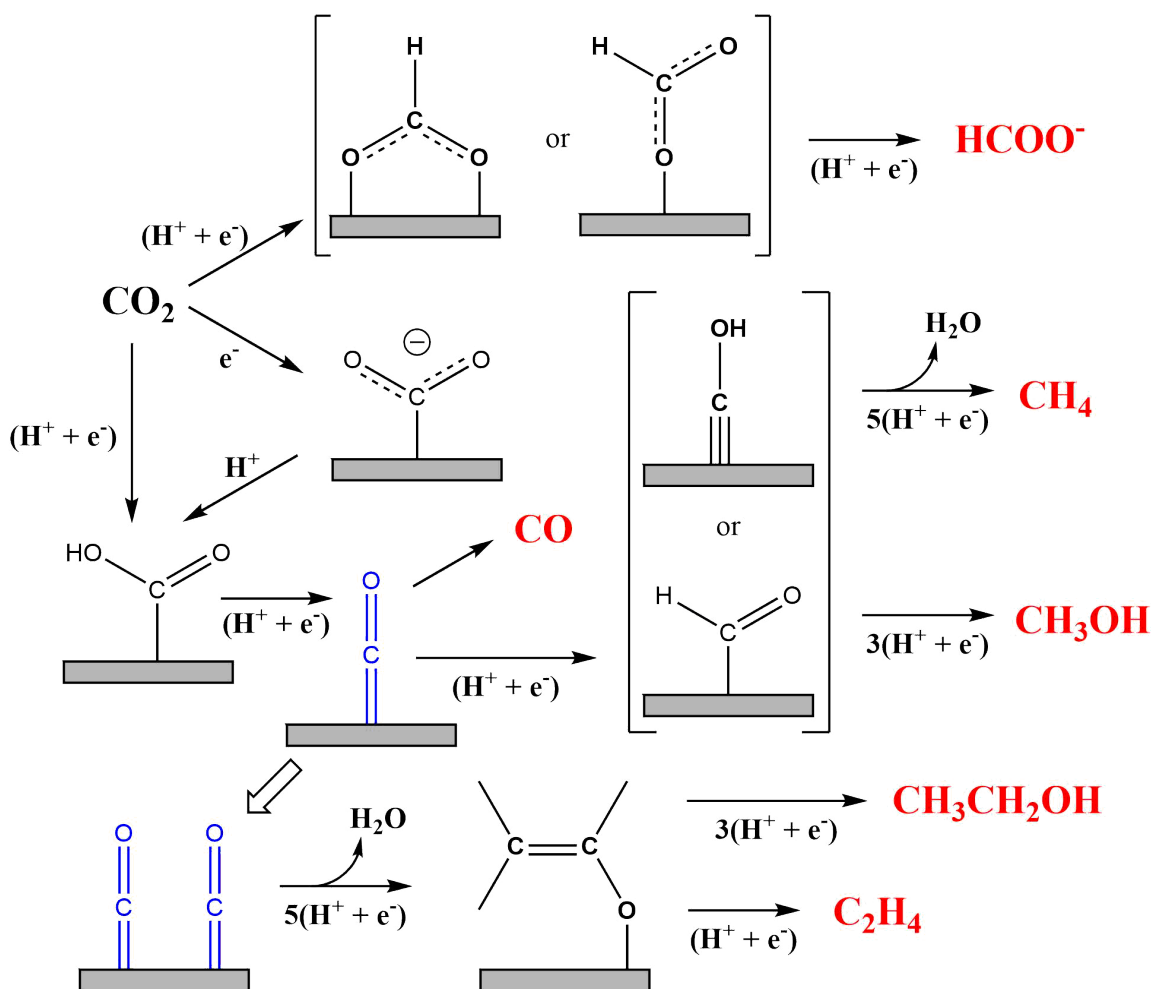
Figure 1.2: Proposed CO$_2$R pathways showing key intermediates for the products in red—formate (HCOO$^-$), carbon monoxide (CO), methane (CH$_4$), methanol (CH$_3$OH), ethanol (CH$_3$CH$_2$OH), and ethylene (C$_2$H$_4$)—based on experimental results and density functional theory (DFT) calculations on copper electrodes. The key carbonyl intermediate (*=CO) is shown in blue. Figure adapted from Kortlever et al.[7]

carboxyl species. CO is produced by removing water from the carboxyl species (frame 3 in Figure 1.3).[8]

1.1.2 Heterogeneous Electrochemical CO$_2$ Reduction Catalysts

One way to alter the CO$_2$R product selectivity is to change the surface binding energy of reaction intermediates. According to the Sabatier principle, the surface binding energy of reactants to heterogeneous catalysts should be strong enough to allow the species to react but not so strong as to poison the catalyst surface and decrease activity. Thus, plots of reactant binding strength versus activity generally give a "volcano" shape with the highest activity surfaces in the center. Given the importance of CO as an intermediate in multielectron
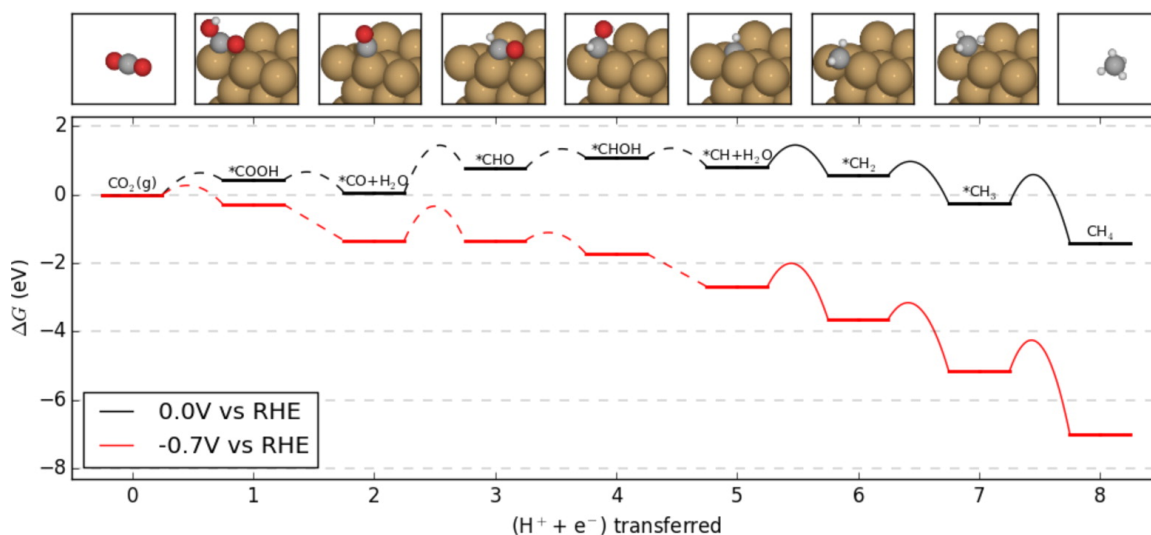
Figure 1.3: DFT-predicted mechanism for methane production on the Cu($2\,1\,1$) surface. Reprinted with permission from Shi et al.[8] Copyright 2014 American Chemical Society.

CO_2R, a volcano plot for CO binding strength (Figure 1.4) can give insight into the best CO_2R catalysts. Copper, gold, and silver all have intermediate binding strength for CO and thus have high CO_2R activity. Gold and silver have a binding strength lower than the thermodynamic chemical adsorption energy of CO and thus favor the desorption rather than further reduction of CO. Therefore, gold and silver produce primarily CO. On the other hand, copper favors the adsorption of CO and thus produces a variety of multielectron products. Platinum and nickel are poor CO_2R catalysts because they are poisoned by CO and primarily generate H_2 (Figure 1.4a).

The relationship between onset potential and CO binding strength clarifies the CO binding strength relationship to selectivity further. The overall CO_2R onset volcano shows similar trends to the CO_2R current density volcano, highlighting the importance of CO binding strength on CO_2R activity. On the other hand, the onset potential for methane or methanol does not show a volcano-like relationship with CO binding strength. There are two distinct regimes of methane/methanol onset potential: weak-CO-binding metals (gold, silver, and zinc) and strong-CO-binding metals (copper, nickel, platinum, and iron). The weak-CO-binding metals have high methane/methanol onset potentials while the strong-CO-binding metals that favor CO adsorption over desorption exhibit similar onset potentials Figure 1.4b. Metals with high methanol onset potentials primarily reduce CO_2 to CO at moderate potentials, while metals with lower onset potentials produce a wide variety of products.

Even the metals that exhibit remarkable selectivity for CO as a product of CO_2R still produce a significant amount of H_2 at low overpotentials. For example, silver does not generate CO at Faradaic efficiencies of > 90 % at ambient temperature and pressure until approximately 1 V overpotential in near-neutral-pH aqueous electrolyte.[2,10]
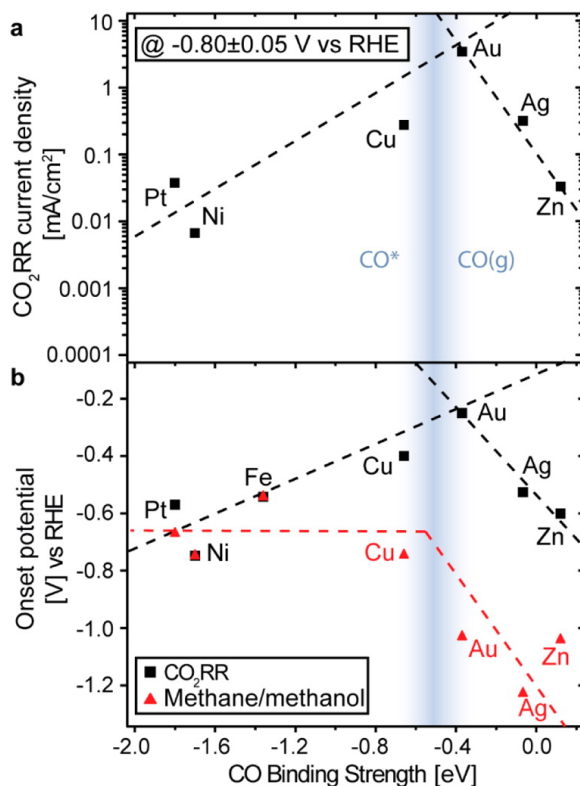
Figure 1.4: Volcano plot for CO binding strength versus (a) total CO_2R activity at -0.8 Volts versus the reversible hydrogen electrode (V_{RHE}) and (b) onset potentials for overall CO_2R activity and for methane or methanol. Dashed lines serve to guide the eye. Reprinted with permission from Kuhl et al.[9] Copyright 2014 American Chemical Society.

1.2   Surface Plasmon Resonance

The intrinsic "dark" selectivity activity of metal cathodes for CO_2R could be improved through excitation of surface plasmon resonance (SPR) because of its ability to couple light energy into surface chemistry.[11] SPR in nanostructured metals has been shown to increase reaction rates in a variety of reactions,[12–15] including gas-phase CO_2R.[16,17] We will explore the role of SPR in altering the onset potential and selectivity in electrochemical CO_2R in this dissertation.

SPR is an incident-light-stimulated resonant oscillation of conduction electrons at the interface between two materials of negative and positive permittivity, commonly between a metal and its surrounding medium (Figure 1.5). This interaction is beneficial in catalysis because it creates strong electric fields at the interface and couples light energy into the catalytic material. The unique excited electron dynamics in SPR may alter the selectivity from ground state electron dynamics.

In Section 1.2.3, I will discuss the factors that determine the wavelength of the SPR which indirectly determines the energy to which electrons are excited. First, I discuss some
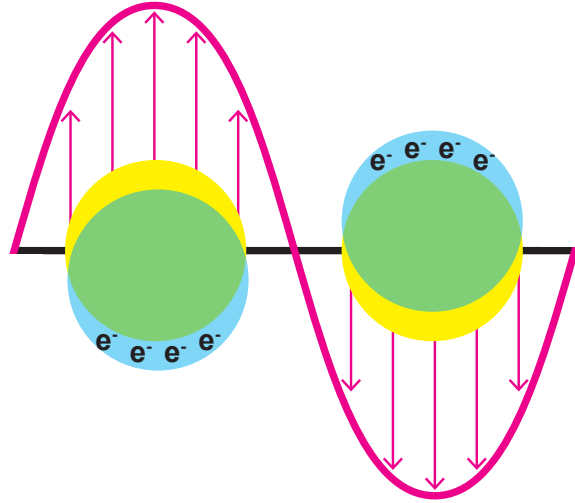
Figure 1.5: Schematic illustration of a localized surface plasmon resonance.

introductory SPR concepts.

1.2.1 Drude Plasma Frequency of a Free Electron Gas

The most fundamental equation used in plasmonics is the Drude plasmon frequency (Equation 1.9) for a bulk conductor, which can be derived by considering a net uncharged plasma slab (Figure 1.6) in which the negative charges (electrons) are displaced slightly by distance x.

$$A = yz$$
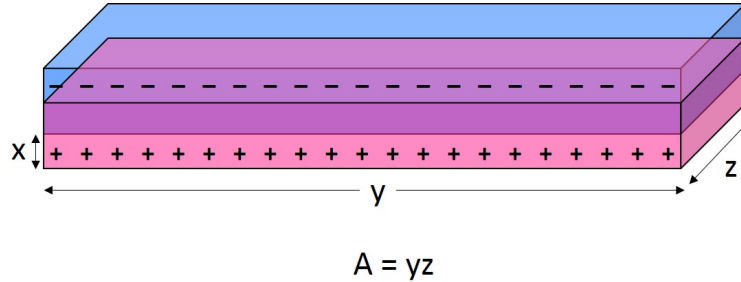
Figure 1.6: Schematic representation of the longitudinal collective oscillation of the conduction electrons in a metal.

By considering the plasma slab as a capacitor, the electric field $\boldsymbol{E}$ generated by this charge separation can be calculated

$$\boldsymbol{E} = \frac{Q}{\varepsilon_0 A} \tag{1.4}$$

where Q is the charge in the positive and negative regions in the slab, ε_0 is the permittivity of free space, and A is the cross sectional area of the planes. Q can be rewritten in terms of the charge density ρ and the volume V of the charged regions as

$$Q = \rho V = (n_e e)(Ax) \tag{1.5}$$

7

where n_e is the electron density and e is the charge of an electron. Thus the electric field can be rewritten as

$$\boldsymbol{E} = \frac{(n_e e)(Ax)}{\varepsilon_0 A} = \frac{n_e e x}{\varepsilon_0} \tag{1.6}$$

The force on the electrons is $-e\boldsymbol{E}$. From the electric field and Newton's second law, we can write

$$\boldsymbol{F} = m_e \frac{\partial^2 x}{\partial t^2} = -e \frac{n_e e x}{\varepsilon_0} = -\frac{n_e e^2}{\varepsilon_0} x \tag{1.7}$$

where m_e is the effective mass of an electron. Putting this equation in standard form for a simple harmonic oscillator, $\frac{\partial^2 x}{\partial t^2} + \omega^2 x = 0$ where ω is the angular frequency of oscillation,

$$\frac{\partial^2 x}{\partial t^2} + \frac{n_e e^2}{\varepsilon_0 m_e} x = 0 \tag{1.8}$$

Thus, the Drude oscillation frequency of free electrons in a plasma is[18]

$$\omega_p = \sqrt{\frac{n_e e^2}{\varepsilon_0 m_e}} \tag{1.9}$$

We use the Drude plasma frequency to derive the SPR condition for a spherical nanoparticle with free electrons in Section 1.2.2.

1.2.2 Surface Plasmon Resonance Condition

The frequency-dependent dielectric function $\varepsilon(\omega) = \varepsilon_1 + i\varepsilon_2$ of a material describes its interaction with light. The real part ε_1 determines the change in the electric field inside the material. For $\varepsilon_1 > 0$, the electric field inside the material decreases relative to the incident electric field. For $\varepsilon_1 < 0$, the electric field inside the material increases relative to the incident electric field. The imaginary part ε_2 describes absorption by the medium (e.g., interband transitions). SPR occurs in the bulk conductor where the real part of the dielectric function is zero ($\varepsilon_1 = 0$). This is derived from solving Maxwell's equations for a gas of free electrons in an oscillating electric field and obtaining the dielectric function

$$\varepsilon(\omega) = 1 - \frac{\omega_p^2}{\omega^2 - i\Gamma\omega} \tag{1.10a}$$

$$\varepsilon_1(\omega) \approx 1 - \frac{\omega_p^2}{\omega^2} \tag{1.10b}$$

$$\varepsilon_2(\omega) \approx 1 - \frac{\omega_p^2}{\omega^3}\Gamma \tag{1.10c}$$

where ω_p is the Drude plasma frequency given by Equation 1.9, ω is the angular frequency of the electric field, $\Gamma = \frac{\nu_F}{\ell}$, ν_F is the Fermi velocity, and ℓ is the mean free path. $\ell = 52$ nm for Ag. Metal clusters larger than 10 nm have the same dielectric functions as the bulk metal.[19]

By the electrostatic approximation, the polarizability α of a homogeneous isotropic sphere is

$$\alpha = 4\pi a^3 \frac{\varepsilon - \varepsilon_m}{\varepsilon + 2\varepsilon_m} \tag{1.11}$$

where a is the radius of the sphere, ε is the complex dielectric function of the sphere, and ε_m is the dielectric constant of the medium. The factor of 2 in front of ε_m comes from $\frac{L+1}{L}$ where L gives the order of the partial wave with $L = 1$ corresponding to the dipole field, $L = 2$ corresponding to the quadrupole field, etc.[19] This strictly dipole polarizability is valid only for particles < 100 nm where the quasi-static approximation (electric field is uniform across the entire particle) applies.[20]

A resonant maximum polarizability occurs as the denominator approaches zero, giving $\varepsilon_1 = -2\varepsilon_m$ (the Fröhlich condition) with the assumption that $\varepsilon_2 \ll 1$ or is fairly constant in the regime of the resonance (which is valid for most metals). Using the approximation for ε_1 (Equation 1.10b) for free electron metals, we find the dipole resonance position

$$-2\varepsilon_m = \varepsilon_1 = 1 - \frac{\omega_p^2}{\omega_{\text{res}}^2} \tag{1.12}$$

Solving for the resonant frequency ω_{res} gives

$$\omega_{\text{res}} = \frac{\omega_p}{\sqrt{1 + 2\varepsilon_m}} \tag{1.13}$$

Assuming that $\varepsilon_m = 1$ for the dielectric of air, we have

$$\omega_{\text{res}} = \frac{\omega_p}{\sqrt{3}} \tag{1.14}$$

Also at the Fröhlich condition, the scattering cross section C_{sca} and absorption cross section C_{abs} experience resonant behavior.

$$C_{\text{sca}} = \frac{k^4}{6\pi} |\alpha|^2 = \frac{8\pi}{3} k^4 a^6 \left| \frac{\varepsilon - \varepsilon_m}{\varepsilon + 2\varepsilon_m} \right|^2 \tag{1.15a}$$

$$C_{\text{abs}} = k\text{Im}[\alpha] = 4\pi k a^3 \text{Im} \left| \frac{\varepsilon - \varepsilon_m}{\varepsilon + 2\varepsilon_m} \right| \tag{1.15b}$$

where $k = 2\pi/\lambda$ and α is the absorption coefficient in Beer's Law[20]

$$I(l) = I_0 e^{-\alpha l} \tag{1.16}$$

where I is the intensity of light passing through a sample of thickness l and I_0 is the intensity of light incident on the sample. Thus, for small particles where $a \ll \lambda$, absorption is much more efficient than scattering. The efficiency Q of absorption and scattering is given by the absorption and scattering normalized by the cross-section of the nanosphere[21]

$$Q = \frac{C}{\pi a^2} \tag{1.17}$$

The absorption and scattering efficiencies for 20 and 100 nm gold and silver nanospheres are given in Figure 1.7. As expected, the extinction (absorption + scattering) efficiency for

the 20 nm nanospheres is dominated by absorption while the extinction spectra for the 100 nm nanospheres is dominated by scattering. The broader peaks for the 100 nm nanospheres indicates increased damping and thus shorter plasmon excitation lifetimes, suggesting that scattering plays a large role in linewidth.[22] According to the uncertainty principle

$$\Delta E \Delta t \geq \frac{\hbar}{2} \tag{1.18}$$

the Heisenberg uncertainty in energy E is inversely proportional to the uncertainty in time t. The full width at half maximum (FWHM) is commonly referred to as the linewidth Γ, and

$$\Delta E = \frac{\Gamma}{2} \tag{1.19}$$

Thus,

$$\Gamma \approx \frac{\hbar}{\tau} \tag{1.20}$$

where τ is the plasmon excitation lifetime taken as Δt. The dielectric functions of real metals do not match the theoretical dielectric function for a free electron gas due to electronic interband transitions. While an explanation for the differences in the dielectric functions of different metals is outside the scope of this work, the spectra illustrate that the plasmonic medium dramatically impacts the plasmonic properties.

1.2.3 Tunability

The resonance position can be tuned by changing the plasmonic material, surrounding dielectric material, size of the plasmonic particle, distance to other plasmonic particles, or the shape of the plasmonic particle.

Plasmonic Material

From the Drude plasma frequency given in Equation 1.9, the resonance frequency decreases as we decrease the number of free electrons in the plasmonic material. In fact, a clear red shift is seen as we move from metals to doped metal oxides (Figure 1.8).

The material also determines the losses in the plasmon oscillation. Though non-noble transition metals have high concentrations of free electrons, they have lower conductivity than the noble metals (silver, copper, and gold). The noble metals have full d-bands, so the conductivity stems from the valence electrons in the sp-band. Because non-noble metals have empty states in the d-bands, both the sp- and d-bands contain valence electrons. Because d-orbitals overlap much less than s-orbitals in bonding, the d electrons experience much higher effective mass than a free electron, giving a high density of states at the Fermi level energy (E_F). While the s-electrons contribute much more to the conductivity because of their greater freedom to move, the s-electrons have a shorter relaxation time due to the high density of states available for scattering. This increased scattering decreases the conductivity and increases Ohmic losses in the plasmonic material.[24]
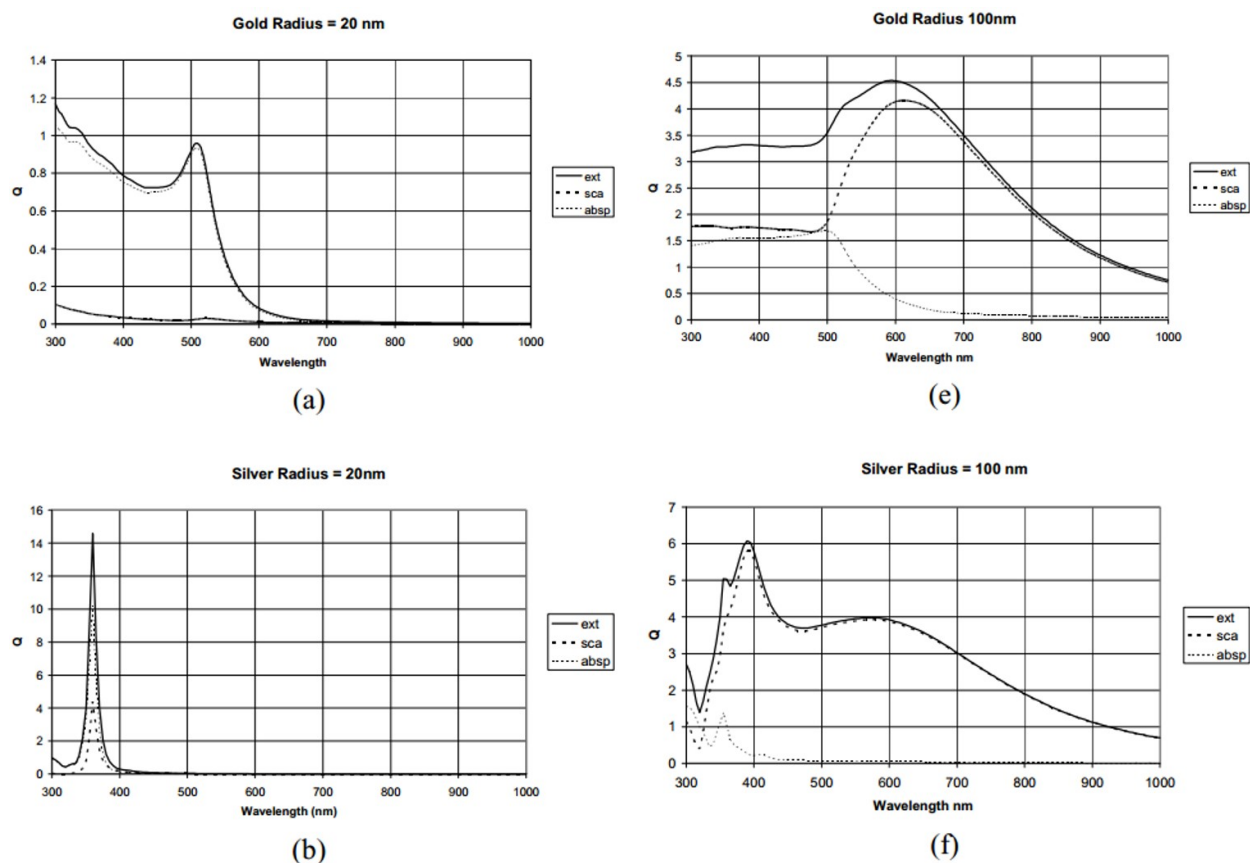
Figure 1.7: Mie-calculated absorption (absp), scattering (sca), and extinction (ext = absorption + scattering) efficiencies for Au and Ag nanospheres. Reprinted with permission from Centeno et al.[21] Copyright 2011 IEEE.

Dielectric Constant of the Surroundings

From Equation 1.13, we see that the plasmon resonance frequency red shifts as we increase the dielectric constant of the surrounding medium. We would expect a plot of $1/\omega_{\text{res}}^2$ or λ_{res}^2 vs. $2\varepsilon_m$ to be linear, which has been experimentally verified by measuring the SPR absorbance peak of tetraoctylammonium-bromide-capped Au nanoparticles suspended in solvents with a wide range of refractive indices (Figure 1.9).[25]

Particle Size

Particle size effects are difficult to determine theoretically because multipolar resonances must be included for particles greater than about 20 nm in diameter. For a classical approximation, as the particle size increases, the separation of charges increases, thus reducing the restoring force of the plasma oscillation and redshifting the SPR. For example, the dipole absorption peak (longest wavelength peak) of colloidal Ag nanocubes suspended in ethanol shifts to longer wavelengths with increasing cube edge length (Figure 1.10b).
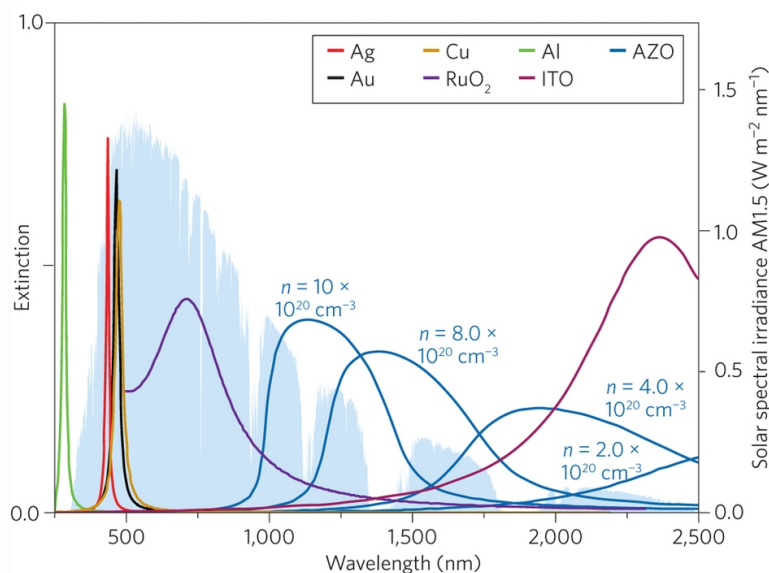
Figure 1.8: Extinction spectra of metal and metal oxide nanostructures with the solar irradiance spectrum in the background. Reprinted with permission from Clavero[23] Copyright 2014 Springer.
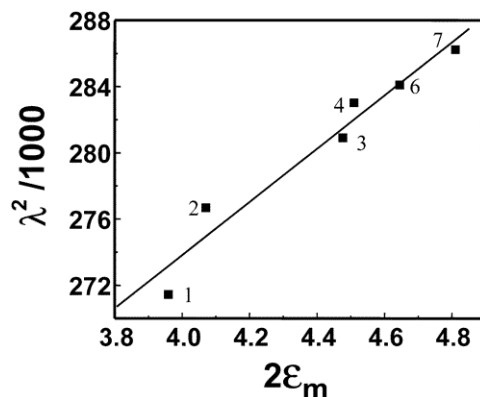
Figure 1.9: Dependence of the plasmon resonance wavelength λ of 6 nm tetraoctylammonium bromide-capped 6 nm Au nanoparticles on the dielectric of the surrounding medium. Reprinted with permission from Thomas et al.[25] Copyright 2014 American Chemical Society.

Particle Shape

The resonance position and number of resonant peaks depends strongly on the shape of the nanoparticle. In general, sharper corners on nanoparticles result in a red-shifted SPR position because there is increased charge accumulation at the corners, resulting in increased charge separation and consequently a weaker restoring force. The number of peaks is determined by the symmetry of the particle.[27] This also explains the red shift in SPR for larger nanoparticles. For example, a Ag nanowire exhibits two plasmon absorption peaks corresponding to the excitation of the transverse and longitudinal mode of the nanowire. A Ag nanosphere is
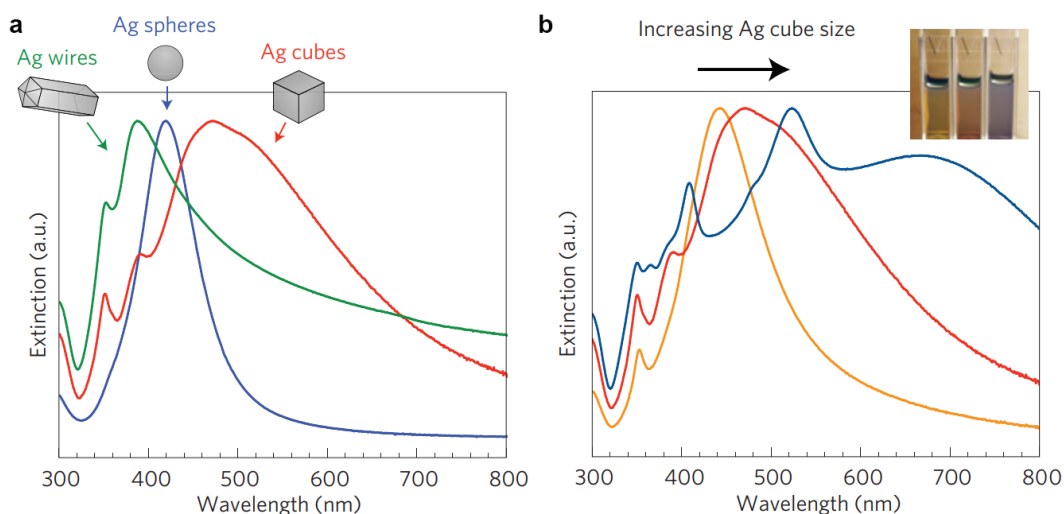
Figure 1.10: Extinction spectra for various silver nanoparticle sizes and shapes. (a) Ag wire (90 nm in diameter), sphere (38 nm in diameter), and cube (79 nm edge length) nanoparticles. (b) Ag nanocubes of various sizes (56 nm, 79 nm and 129 nm edge lengths correspond to orange, red and blue spectra respectively) with inset showing the cubes dispersed in ethanol. Reprinted with permission from Linic et al.[26] Copyright 2011 Springer.

perfectly symmetrical and only exhibits a single plasmon absorption peak. A Ag cube exhibits three plasmon absorption peaks with the primary peak appearing at longer wavelengths than the nanosphere absorption peak (Figure 1.10a).

1.2.4 SPR Timeline

When photons matching the resonance frequency interact with the plasmonic nanoparticle, they excite a collective oscillation of the conduction electrons, which is SPR. The oscillation is coherent for ~ 10 fs, and it is during this time that the local electric fields around the nanoparticle are greatly enhanced due to the SPR-induced charge separation on the surface of plasmonic nanostructures (Panel 1 of Figure 1.11). SPR can decay radiatively via emission of a photon or nonradiatively through excitation of an electron-hole pair ("hot" carriers). In a small nanoparticle, the nonradiative pathway is dominant and the hot electrons are excited from energies $E_F - h\nu < E < E_F$ (leaving hot holes at these energies) to energies $E_F < E < E_F + h\nu$ (Panel 2 of Figure 1.11). These carriers have a short lifetime (~ 10 fs) before they start to relax through electron-electron scattering and form an electron distribution characteristic of a thermal distribution at an elevated temperature (Panel 3 of Figure 1.11). This rapid establishment of a thermal electron distribution is the reason for the "hot" moniker to distinguish electron excitation in metals from that in band gap materials. ~ 1 ps after illumination, the electronic temperature has reached thermal equilibrium with the lattice, and the nanoparticle lattice releases the excess energy in the system as localized heating (Panel 4 of Figure 1.11).[28]
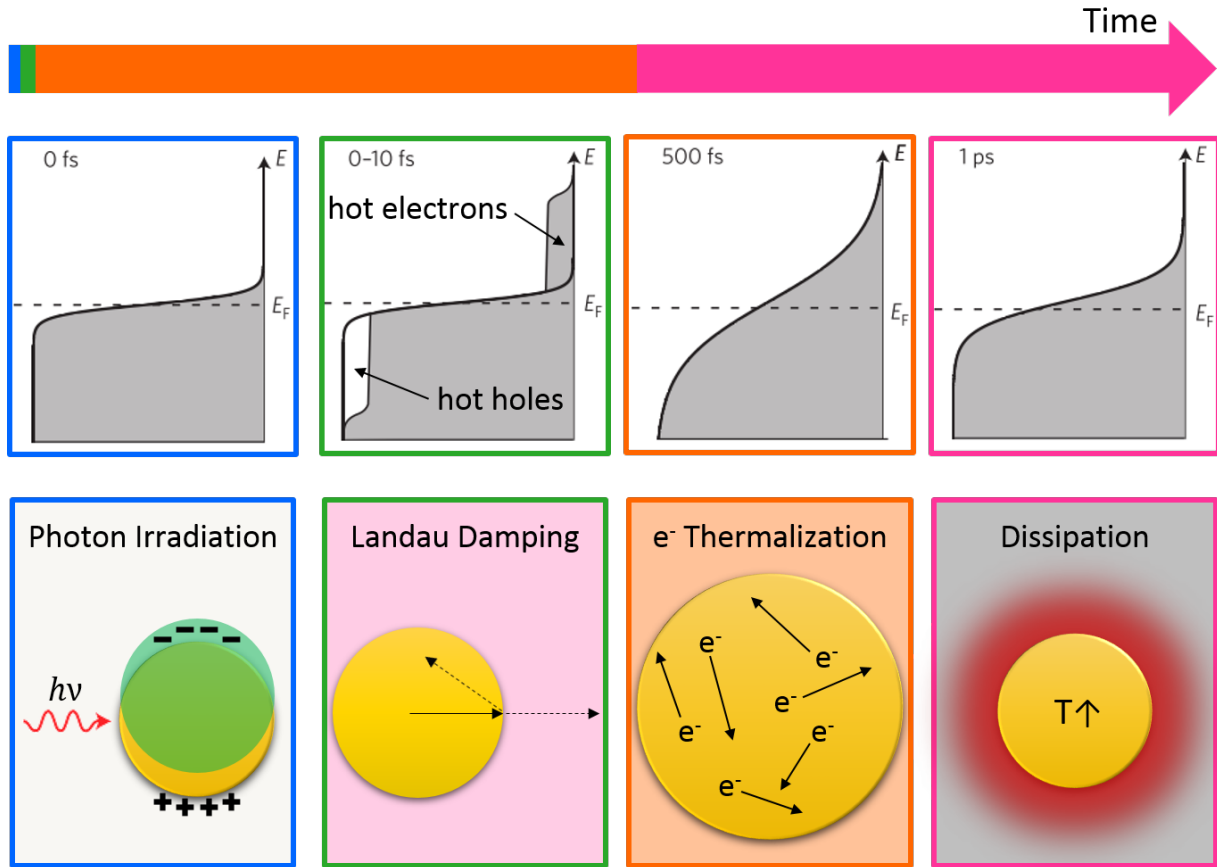
Figure 1.11: Time evolution of SPR decay. (TOP) Time axis showing color-coded approximate time scales of each stage of the decay. (MIDDLE) Electronic energy distributions with the shaded areas indicating occupied electronic states. (BOTTOM) Cartoon depiction of the physical process at each stage of the decay. Adapted from Linic et al. [28]

1.2.5 Surface Plasmon Resonance for Catalysis

Plasmonics can be used to enhance catalytic reactions through the strong local electric fields generated by the collective oscillation of conduction electrons (Figure 1.12) or the excited electrons and holes generated by Landau damping.

Plasmonic Catalysis with Strong Electric Fields

The effect of time-dependent potentials $V(t)$ on an isolated, time-independent system with Hamiltonian $\hat{H}_0$ can be described with the Hamiltonian $\hat{H} = \hat{H}_0 + V(t)$. Atoms in a time-dependent uniform electric field $\boldsymbol{E}$ experience the potential

$$V(t) = -\boldsymbol{\mu_d} \cdot \boldsymbol{E} = -\boldsymbol{\mu_d} \cdot E\hat{e}\cos(\omega t) \tag{1.21}$$
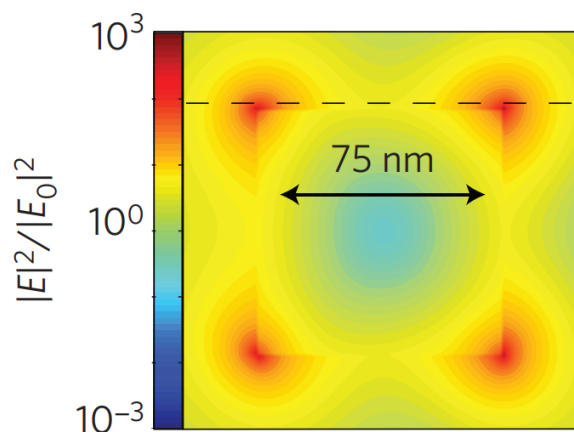
Figure 1.12: Spatial distribution of the SPR-induced enhancement of electric field intensity expressed as a ratio of the square of the magnitude of electric field generated $|E|^2$ to the square of the magnitude of the incident electric field $|E_0|^2$ at a 75 nm Ag nanocube. The finite-difference time-domain (FDTD) simulation were performed at the SPR peak wavelength (420 nm). Reprinted with permission from Linic et al.[26] Copyright 2011 Springer.

where $-\boldsymbol{\mu_d}$ is the electric dipole moment, E is the amplitude of the electric field, $\hat{e}$ is the unit vector of the field propagation direction, and ω is the angular frequency. For a system perturbed by a periodic harmonic potential, time-dependent perturbation theory is used to derive Fermi's Golden Rule which states that the transition rate between an initial state $|i\rangle$ and a final state $|f\rangle$ is

$$R_{i\rightarrow f}(t) = \frac{2\pi}{t}|\langle f|V|i\rangle|^2\delta(\omega_{fi} - \omega) \tag{1.22}$$

where $\omega_{fi} = \frac{E_f - E_i}{\hbar}$, E_f is the energy of the final state, E_i is the energy of the intial state, and $\hbar$ is the reduced Planck's constant. Thus, the transition rate for an electron in a harmonic electric field is proportional to the square of the field amplitude. This interaction between an electron and an electromagnetic wave is called an electric dipole transition.

The strong local electric fields produced by SPR increase electronic transition rates for any reaction, plasmonic or otherwise, occurring in the volume where the electric fields are enhanced. This boost in reaction rates, proportional to the square of the electric field amplitude, can be quite significant because the electric fields at the surface of plasmonic nanostructures can be several orders of magnitude larger than the incident electric field from irradiation (Figure 1.12). The plasmonic enhancement in reaction is potent in surface catalytic processes because the catalytic reactions and the strong electric fields are co-located at the surface of the nanostructures.

Plasmonic Catalysis with Hot Electrons or Holes

The nonradiative decay mechanisms for SPR is absorption where the energy of the photon is transferred to an electron in the plasmonic material. This energy transfer results in an

electron excited to an unoccupied higher energy electronic state and a hole in the vacated state. As mentioned in Section 1.2.4, the plasmonically exited electrons and holes are referred to as "hot" because they thermalize rapidly, leading to the establishment of a electronic distribution typical of an elevated temperature system. Excited electrons and holes have more energy than their ground state counterparts, allowing them to overcome energy barriers for reduction and oxidation reactions, respectively. Thus, the plasmonic hot electrons and holes can be used to drive a variety of catalytic reactions.

The exact mechanism for SPR catalysis via hot electrons is subject to much debate, but a discussion of several of the possible mechanisms are discussed in Chapter 4.

Chapter 2

Best Practices for Photoelectrochemical Conversion[1]

We have chosen a photoelectrochemistry (PEC) approach to carbon dioxide reduction (CO_2R) because PEC approaches to water splitting and CO_2 reduction have already demonstrated great potential via high energy efficiencies or reaction selectivity that differs from the unilluminated electrode. However, despite the promise of PEC, inconsistent methodologies render direct comparison of system performance challenging. It is vital that researchers control and report temperature and light flux accurately so that results are comparable across the field. Like other catalytic systems, PEC active surfaces are subject to morphology changes and delamination. Here, we highlight a few common pitfalls in analysis and experimental measurement of PEC reactions and share our thoughts on best practices.

2.1   Temperature Control

The strong light absorption of water can lead to dramatic heating of the PEC cell.[29,30] PEC cells are susceptible to heating whether the light source is a broadband incandescent bulb or even a monochromatic beam. Increasing the electrolyte temperature typically exponentially decreases the solubility of gaseous reactants, by the van't Hoff equation, and significantly alters the product distribution, as shown by Corson et al.[31] It is thus imperative in PEC to use a temperature controlled cell with precision of at least 1 K, especially when comparing illuminated and unilluminated activity and product distributions.

Temperature control is a technique that is commonly employed in photochemistry (PC) to compare thermal and photocatalytic rates but is not always used in PEC. While most PEC studies do not explore the changes in activity and selectivity with temperature variation, temperature control is still beneficial even in dark electrochemistry (EC). Activity can change during dark EC when the temperature is varied by just 1 or 2 K (Figure 2.1). As building temperatures differ between labs and even from day to day in a single lab, cell temperature control should be employed for more consistent "room temperature" conditions.

Effective cell temperature control requires incorporation of a temperature probe in contact

---

[1]This chapter describes joint work with Elizabeth Corson.
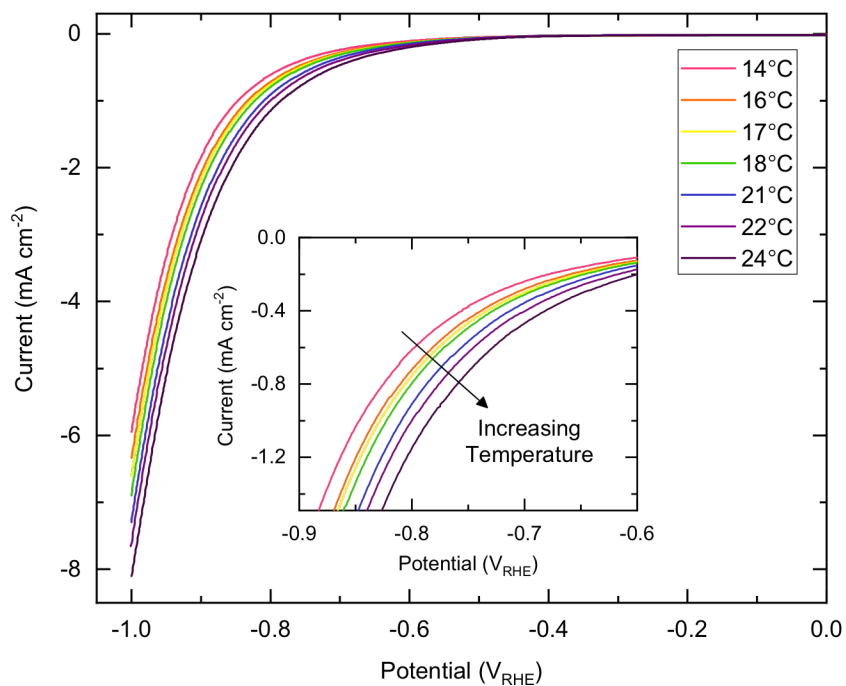
Figure 2.1: linear sweep voltammetry (LSV) at 100 mV s^{-1} at a silver electrode in CO$_2$-saturated K$_2$CO$_3$ electrolyte at various temperatures. CO$_2$ flows continuously through the cell at 5 sccm. Inset is the same data in a smaller potential range to demonstrate activity increase with increasing temperature.

with the electrolyte, ideally as close to the working electrode as possible, a cooling method, and a proportional-integral-derivative (PID) controller. The selection and sizing of the cooling method depends on the cell geometry and the maximum light intensity desired, as this will be defined by the maximum heat removal capability of the system. One cooling method is a solid-state Peltier element with a heatsink and fan.[31] While complete cell submersion in a water bath would make light incorporation difficult, a circulating bath connected to a cooling jacket or integrated heat-transfer channels within the cell can be designed to allow electrode illumination.[32]

2.2 Light Flux Measurement

Quantifying the intensity and spectral properties of the light *at the electrode surface* is important both when simulating solar illumination and calculating the light utilization efficiency of a photoelectrode. Here, we discuss common challenges and methods for quantifying the light intensity on the photoelectrode. There are two ways to measure the quantum efficiency of light utilization for a photoelectrode: external quantum efficiency (EQE) and internal

quantum efficiency (IQE).

$$EQE = \frac{\text{photogenerated electrons}}{\text{incident photons}} \tag{2.1a}$$

$$IQE = \frac{\text{photogenerated electrons}}{\text{absorbed photons}} \tag{2.1b}$$

Both EQE and IQE quantify how effectively the photoelectrode uses light to generate current and both require accurate measurement of incident light intensity on the photoelectrode. We suggest that IQE should always be reported because it deconvolutes a material's ability to separate and collect photoexcited electrons and holes from its absorption. The material's optical properties should be reported separately. Electronic properties of a material are a fundamental part of the material properties while optical properties can be increased or decreased dramatically with electrode surface structuring or coatings to control the reflectivity.

When measuring the incident light intensity, it is important to measure the light incident on the photoelectrode, not the PEC cell. Glass, quartz, water, common electrolytes, and gas bubbles can all have significant reflection or absorption, making the light intensity incident on the photoelectrode significantly less than the light intensity incident on the photoelectrochemical cell (Figure 2.2). Researchers should also bear in mind that the optical properties of all materials are temperature-dependent.[29] While photoelectrochemical device research incorporates short path lengths through electrolyte and anti-reflective coatings on cell windows,[29] most laboratory-scale photoelectrochemical cells are not designed with maximum light transmission to the photoelectrode in mind. Thus, the light attenuation may be significant. Low light intensity may impact the signal to noise ratio between the photocurrent and background "dark" current. Additionally, it may be difficult to control the temperature of electrochemical cells that are not designed for high light transmission due to the high light intensity needed to achieve a measurable photocurrent.

The light attenuation through the electrochemical cell walls and electrolyte becomes especially important with broad-spectrum illumination because the light transmission of cell components is wavelength dependent and often has especially low transmission in the ultraviolet (UV) or infrared (IR) regions of the spectrum (Figure 2.2b). While glass is often replaced with quartz for ultraviolet transmission, the effect of the absorption of water[30] or the electrolyte salt is not commonly accounted for.

Light power incident on the cell can be measured with a power meter, thermopile, or photodiode then corrected to find the light power incident on the photoelectrode using the transmission of the cell components. For broad-spectrum illumination, it is important to measure the light spectrum rather than just the light intensity because of the wavelength dependence of the photoactivity and the wavelength dependence of the optical properties of the cell components. The method for correcting spectral mismatch between a lamp and solar irradiance described by Döscher et al.[30] is also suitable for correcting for decreased transmission of cell components.

Additionally, researchers should confirm that the cell components intended to define the illumination and active area of a photocathode (e.g. epoxy or o-rings) are opaque for all of the light spectrum (not just the visible) that will be used for illumination. A UV-
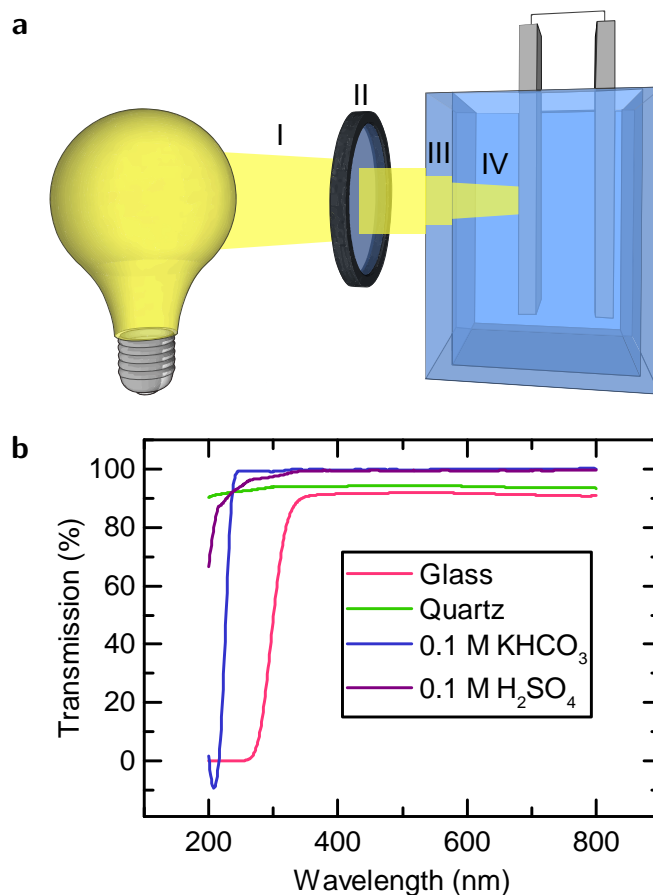
Figure 2.2: Light intensity attenuation from the light source to the photoelectrode surface. (a) Light intensity per unit area decreases (I) as a function of distance from a non-colimated source, (II) when passing through optical lenses or filters, (III) when passing through electrochemical cell walls, and (IV) when passing through electrolyte. (b) Transmission spectra of a 1 mm thick glass slide, 2 mm thick quartz window, 1 cm path length through 0.1 M $KHCO_3$, and 1 cm path length of 0.1 M sulfuric acid H_2SO_4. Transmission spectra of glass and quartz are measured relative to air. Transmission spectra of salt solutions are measured in a quartz cuvette relative to a quartz cuvette filled with ultrapure water.

transmissive epoxy could result in the photoactive area of an electrode being much larger than the electrochemically active area.[30]

2.3   Electrode Stability Characterization

The activity and performance of electrocatalysts depends on the specific surface morphologies and structural features (e.g., high index planes, step edges). Active catalysts can delaminate from the electrode surface or undergo dramatic morphological, composition, phase, and activity changes under reaction conditions[33] or when exposed to light or voltage.[34] Commercialization

of PEC processes will require stable operation for thousands of hours. Thus, it is critical to characterize microscopic catalyst evolution in order to understand and control or prevent morphological changes induced by PEC reactions.
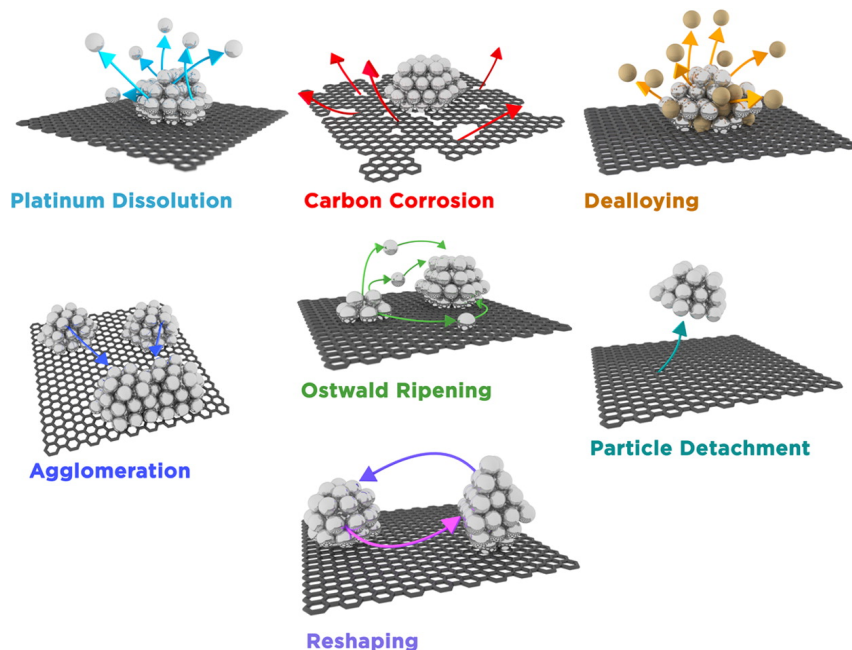
Figure 2.3: Commonly observed degradation mechanisms for platinum or platinum-alloy catalyst particles on a carbon support as commonly found in a polymer electrolyte membrane fuel cell (PEM-FC). Reprinted with permission from Hodnik et al.[35] Copyright 2016 American Chemical Society.

Researchers often use the stability of the current over time in long-term constant voltage experiments as a measure of electrode stability, but this method gives no insight into the mechanism for activity degradation. Significant reaction-induced morphology changes of the catalyst during reaction conditions can be observed through identical location transmission electron microscopy (IL-TEM), in-situ electrochemical transmission electron microscope (TEM), scanning tunneling microscopy (STM), and ambient pressure x-ray photoelectron spectroscopy (AP-XPS).[33,35] It is well known that successive oxidation and reduction cycles can degrade catalysts, but constant-voltage experiments also induce catalyst dissolution, corrosion, and restructuring. Degradation mechanisms identified for catalyst particles in a PEM-FC include catalyst dissolution, support corrosion, catalyst dealloying, catalyst particle agglomeration or coalescence, Ostwald ripening, catalyst particle detachment, and atomic rearrangement or reshaping (Figure 2.3).[35] Our recent study of a silver thin film cathode showed decreased elctrochemical surface area (ECSA), increased broad-spectrum absorption, and a broader grain size distribution after performing CO_2 electrolysis without illumination.[34] We found that the changes in optical properties and electrochemical surface area changed quickly in the first few minutes of applied potential but reached a steady state between 30 and 60 min. of electrolysis. In this case, we were able to "electrochemically condition" the silver photocathode for 45 min. to achieve stable performance over hours.[34]

Measuring the changes in morphology during PEC is critical when attempting to understand the structure-function relationships of a photoelectrode. Researchers should, at a minimum, compare the morphology changes before and after PEC using scanning electron microscopy (SEM), TEM, atomic force microscopy (AFM), or another readily available technique. However, ex-situ structural characterization will not detect reversible morphology or composition changes as the material may revert to its original structure after leaving the reactive environment. It is especially important for PEC researchers to check for reaction-induced morphology changes because the optical properties of the photoelectrode may change as well. Changes to the absorption of the electrode will alter IQE calculations as well as the photoactivity.

Conclusion

Incorporation of electrochemical cell temperature control, measurement of light flux at the surface of the photoelectrode, and monitoring of PEC-induced changes in morphology and optical properties are best practices for accurate and reproducible data. Following the guidelines outlined here will lessen confusion in the literature and allow the field of PEC to advance more quickly. We use these principles in the following chapter to design a PEC CO_2R cell.

Chapter 3

Design of a Temperature-Controlled Photoelectrochemical Cell[2]

Investigating photoelectrochemistry (PEC) reactions requires a vessel that contains electrolyte and permits illumination of the photoelectrode that is immersed in the electrolyte. While a simple single chamber electrolytic cell with a transparent window may be appropriate for the study of well-characterized reactions with a single product, a new PEC cell design is needed for more complicated reactions where quantification of multiple gaseous or liquid products is required, as in the case of carbon dioxide reduction (CO_2R). A PEC cell that allows one to measure changes to the product distribution with illumination is critical to understanding the mechanism of plasmon-enhanced PEC. In this chapter, we describe the design and operation of a temperature-controlled PEC cell for analysis of gaseous and liquid products formed at an illuminated working electrode. This cell is specifically designed to quantitatively analyze PEC processes that yield multiple gas and liquid products at low current densities and exhibit limiting reactant concentrations that prevent these processes from being studied in traditional single chamber electrolytic cells. The geometry of the cell presented here enables front-illumination of the photoelectrode and maximizes the electrode surface area to electrolyte volume ratio (S/V) to increase liquid product concentration and hence enhances ex situ spectroscopic sensitivity toward them. Gas is bubbled through the electrolyte in the working electrode chamber during operation to maintain a saturated reactant concentration and to continuously mix the electrolyte. Gaseous products are detected by an in-line gas chromatograph (GC), and liquid products are analyzed ex situ by proton nuclear magnetic resonance (^1H NMR).

To validate the cell and demonstrate its effectiveness, we present two sets of CO_2R experiments and their corresponding product analyses. First, we compare the product distribution during the reduction of CO_2 on a Ag foil electrode in the PEC cell to the same reaction performed in a common CO_2R electrochemical cell, showing no significant difference in the results. Second, to demonstrate the temperature control of the cell, we reduced CO_2 on Ag foil at four different temperatures ranging from 8.0 to 45.0 °C. In Chapter 4, we use this cell to compare product distributions between illuminated and unilluminated conditions on a plasmonic Ag cathode. The PEC cell and methods presented here provide precise and

---

[2]This chapter describes joint work with Elizabeth Corson.

accurate measurements of multiple gaseous and liquid products while illuminating the active surface of one of the electrodes. While we test the PEC cell presented here for CO_2R, these design considerations apply to any PEC system with multiple products, low current densities, and limiting reactant concentration. Examples include nitrogen reduction to ammonia and methane oxidation to methanol, ethane, or ethylene.

3.1 Cell Design Criteria

CO_2R is challenging to study due to the low solubility of CO_2 in water and generally low current density which yields a mixture of gaseous and liquid products at low concentrations.[2] Researchers studying electrochemical CO_2R have addressed these issues with leak-tight CO_2-flow cells that maximize the electrode S/V, generally by minimizing the cell volume.[3,36] The gas flow maintains CO_2 saturation of the electrolyte, provides mixing to limit mass transfer limitations, and carries evolved gases to an in-line product analysis system. The typical CO_2R cells also incorporate an ion-exchange membrane to separate the anode and cathode to prevent product crossover between chambers, parallel electrodes to ensure even current distribution across the face of the electrodes, and cell construction from electrochemically stable materials that resist degradation and prevent contamination of the electrolyte. While these cell design criteria are effective and sufficient for dark electrochemistry, no comparable cell exists that allows for front-illumination of the working electrode while still providing all the useful characteristics of the small volume, parallel-electrode cell configurations.[3,36]

In addition to the criteria for dark electrochemical CO_2 reduction, PEC CO_2 reduction also requires control of electrolyte temperature and a geometry conducive for front-illumination of the photoelectrode. As a result of the need to concentrate soluble products with low electrolyte volume, PEC cells have low cell mass and are especially susceptible to heating under illumination. Small changes in temperature affect the electrochemical activity (Figure 2.1) and product distribution making temperature control requisite when comparing performance under illumination to dark performance. Front-illumination of the electrodes active surface is desired over back-illumination, in which the electrode is illuminated through the inactive back side of the electrode, to remove the need for electrode optical transparency and to maximize the light intensity on the active surface of the electrode.

In the first iteration of PEC cell design, we designed a gas-tight glass cell with quartz end caps and a membrane separating the catholyte and anolyte (Figure 3.1). This cell can hold elevated pressure or vacuum unlike the compression cells. It also allows front- or back-illumination of the photoelectrode because the electrodes in this cell do not serve as a cell wall to contain electrolyte like the electrodes in compression cells. If an electrode could not fit through the glass necks of the cell, the electrode was attached to the conductive connector through the opening for the membrane while the cell was disassembled. The glass PEC cell has a 30 mL catholyte and anolyte volume each and a cathode-side gas head space of 10 mL. The large cell volume not only resulted in dilution of soluble CO_2R products but also required gas flow rates of > 40 standard cubic centimeters per minute (SCCM) to adequately mix the gas headspace and achieve full quantification of gaseous products in the GC. The rapid CO_2 flow rate results in dilution of the gaseous products evolved in CO_2R, increasing the partial current density of gases needed for detection.
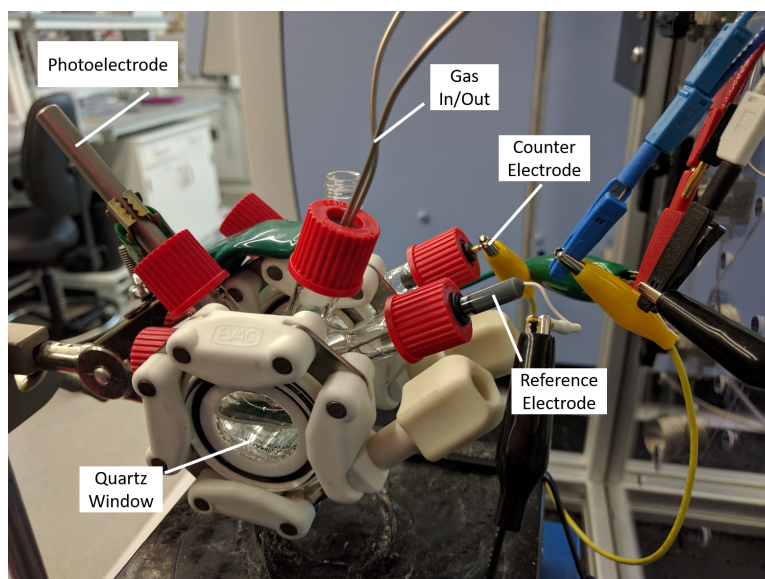
Figure 3.1: Gas-tight glass PEC cell with front- or back-illumination possible.
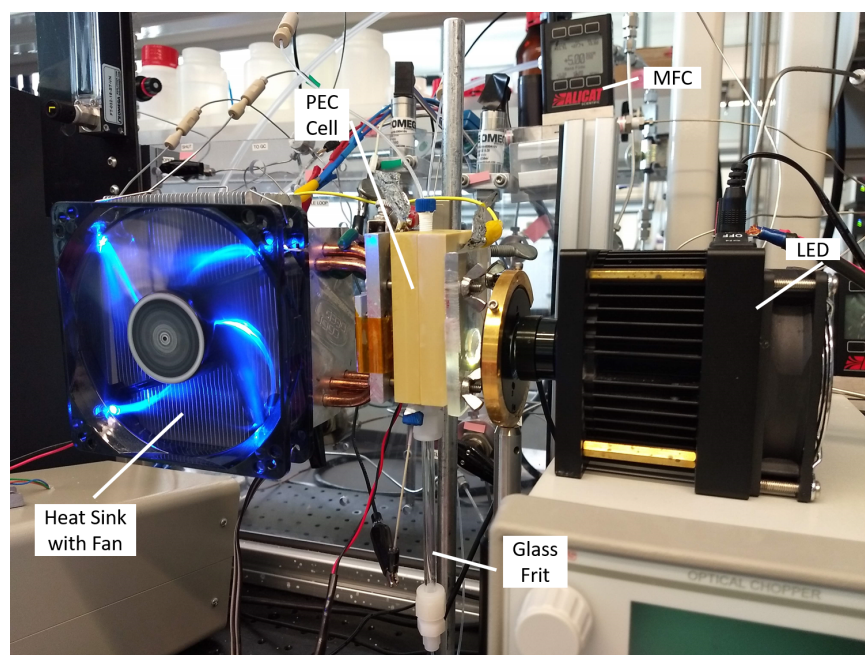
Figure 3.2: PEC cell in operation.

To achieve the smaller electrolyte volume and gas headspace necessary to improve CO_2R product decection, we modified the aligned parallel plate design of the dark compression cells reported in the literature[3,36] to allow front-illumination and electrolyte temperature control. Front-illumination was achieved by offsetting the parallel working and counter electrodes and illuminating the working photoelectrode through a quartz window and the working-side electrolyte. Temperature regulation is achieved by mounting a Peltier device and a central processing unit (CPU) heat sink and fan to the back, inactive surface of the photoelectrode
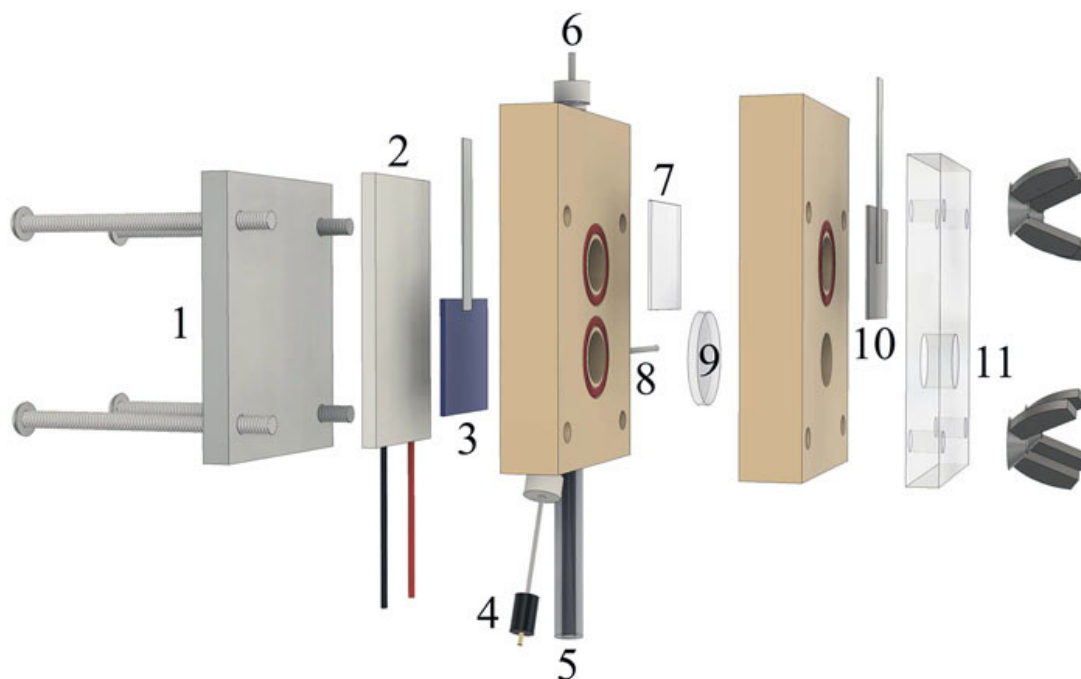
Figure 3.3: Schematic representation of the PEC cell. The copper and aluminum heat sink (not shown) is secured against the aluminum back plate (1) that transfers heat from the Peltier element (2). The working photoelectrode (3) is in close proximity to the reference electrode (4) and thermistor (8) and is separated from the counter electrode (10) by a membrane (7). Gas enters through the glass frit at the bottom (5) and flows through tubing at the top (6) to the GC for product analysis. A hole in the front plate (11) allows light to shine through the quartz window (9) onto the photoelectrode (3). The total volume of the electrolyte used in the working electrode chamber is 2.3 mL, and the electrode surface areas are 1 cm^{-2} (1.1 cm diameter circles). Reproduced from Corson et al.[31] with the permission of AIP Publishing.

and regulating the cooling with proportional-integral-derivative (PID) control, a control-loop feedback mechanism (Figures 3.2 and 3.3).

Like the electrochemistry (EC) cells on which it is based, the PEC cell incorporates continuous CO_2 flow through a glass frit at the bottom of the cell to maintain CO_2-saturation of the electrolyte and to carry the evolved gaseous products to a GC for analysis. We attempted to use a gas chromatograph - mass spectrometer (GC-MS) for gaseous product detection but were unable to quantify H_2. Though the capillary column in the GC was useful for separating and distinguishing CO_2 from CO in the mass spectrometer (MS) detector, it required that the vacuum pressure in the MS was higher than in a standalone MS. Thus, the baseline for low mass-to-charge-ratios was too high to distinguish H_2. The PEC cell is milled from polyether ether ketone (PEEK), a chemically inert hard polymer, and has a 0.43 $cm^2\,mL^{-1}$ S/V that allows for high sensitivity in ex situ liquid product analysis. For comparison, the cell used by Kuhl et al.[3] had a S/V of 0.56 $cm^2\,mL^{-1}$, and Lobaccaro et al.[36] reported a S/V of 0.67 $cm^2\,mL^{-1}$. Both the working and counter electrodes of our PEC cell have a surface area of 1 cm^{-2}. The cell is sealed around five O-rings and compressed by

tightening four screws with wing nuts. A complete list of cell parts is provided in Table 3.1.
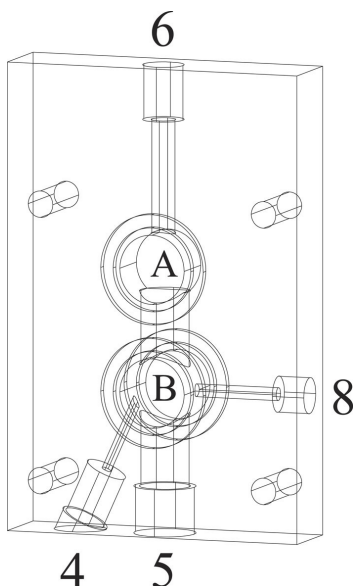
Figure 3.4: Wireframe view of the photoelectrode chamber of the PEC cell. The gas enters a port at the bottom of the cell (5) and exits through a port at the top of the cell (6). The reference electrode port (4) and the thermistor port (8) enter the bottom chamber (B) near the photoelectrode. The photoelectrode covers the back of the bottom chamber, and the working-chamber electrolyte is connected to the counter-chamber electrolyte through a membrane covering the top chamber (A). A cylindrical bore connects the top and bottom chambers. 2.3 mL of the electrolyte is added to the sealed chamber and entirely fills both the bottom and top chambers. Reproduced from Corson et al.[31] with the permission of AIP Publishing.

We considered a few possibilities for regulating the cell temperature after designing the front-illumination PEC compression cell. Simple immersion of the cell in a water bath would not provide the heat dissipation capacity or control over electrolyte temperature that we required. Circulating chilled water on the photoelectrode back plate could provide rapid cooling and a high heat dissipation capacity but would be bulky and susceptible to leaks. Additionally, we were unsure how responsive a water-cooled system would be to PID control or how rapidly it could adjust to changes in heat flux such as the illumination source turning on or off. We attempted to use self-heating tape wrapped around the cell. Heating tape can only provide elevated temperature control, but it is cheap and easy to use. However, heating tape is not viable in an electrochemical system because the coiled tape around the cell creates an induction effect and makes electrochemical measurements unreliable or impossible. The temperature regulation solution we selected is a Peltier device and heat sink mounted against the back of the photoelectrode and connected to a PID controller and temperature probe. Peltier devices use the thermoelectric effect to rapidly heat or cool and are relatively thin and manufactured in a variety of shapes and sizes for easy incorporation into devices. The lack of moving parts and measurable external electric field makes Peltier devices easy to incorporate into an electrochemical compression cell. The Peltier device, PID controller, and temperature

Table 3.1: PEC cell parts list to make one complete device. All quantities needed are 1 unless indicated by * (quantity: 6) or † (quantity: 4).

Purpose	Part Description	Supplier	Part No.
Cell Body	2" × 1' × 1/2" Bar, PEEK	McMaster	9089K126
Cell Front Plate	12" × 12" × 1/4" Sheet, Polycarbonate	McMaster	8707K173
Cell Back Plate	6" × 6" × 1/4" Sheet, Aluminum	McMaster	86825K721
Tubing to Frit	1/16" Tube to 1/4" Tube Reducing Union	Swagelok	NY-400-6-1
Frit to Cell	1/4" Tube to 1/8" NPT PTFE Connector	Swagelok	T-400-1-2
Glass Frit	1/4" OD × 135 mm Porosity E Filter Stick	Ace Glass	Custom
Reference Electrode	1 mm OD leak-free Ag/AgCl, 3.4 M KCL	Innovative Instruments	LF-1
Reference Fitting	1/4-28 Blue ETFE Flangeless Nut for 1/16" OD	IDEX	P-210
	1/4-28 Flat-Bottom ETFE Flangeless Ferrule for 1/16" OD	IDEX	P-200x
Reference Sleeve	1/16" OD × 0.042 ID × 1.6" NanoTight Sleeve Purple	IDEX	F-252
Gas Out Fitting	1/4-28 Blue ETFE Flangeless Nut for 1/16" OD	IDEX	P-210
	1/4-28 Flat-Bottom ETFE Flangeless Ferrule for 1/16" OD	IDEX	P-200x
O-rings*	15/16" OD × 13/16" ID × 1/16" Buna-N O-ring	Apple Rubber	AS-568-019 70 hardness
In/Out Tubing	1/16" OD × 0.02" ID FEP Tubing, 5 m	Valco	TFEP120-5M
Window	20 mm × 2 mm Quartz Disk	Aireka Cells	QD10008
Compression†	2.2" Stainless Steel Screws		
Compression†	Stainless Steel Wing nuts		

probe will likely need to be purchased separately and integrated by the user.

The three primary temperature probe options are a thermocouple, thermistor, or resistance temperature detector (RTD). A thermocouple is calibrated to measure temperature based on the temperature-dependent voltage generated between two wires in the probe. Thermistors and RTDs measure temperature based on the temperature-dependence of a resistor inside the probe. Thermistors contain a ceramic or polymer resistor while an RTD contains a metal resistor. Thermocouples are the cheapest temperature probe and have the largest temperature range, but are generally better at high temperatures and can drift in their temperature measurement over time due to chemical changes such as oxidation. This application requires stable and consistent temperature control around room temperature, so a thermocouple is not appropriate here. While RTDs and thermistors have a slower response time than a thermocouple, they are more accurate and have much greater long-term stability. Thermistors have a smaller operational range than RTDs, but they are slightly better at precision measurements. The liquid temperature range of water is more restrictive than a thermistor's temperature range, and precision is critical due to the significant changes in electrochemical activity with temperature. Thus, a thermistor was selected for this application.
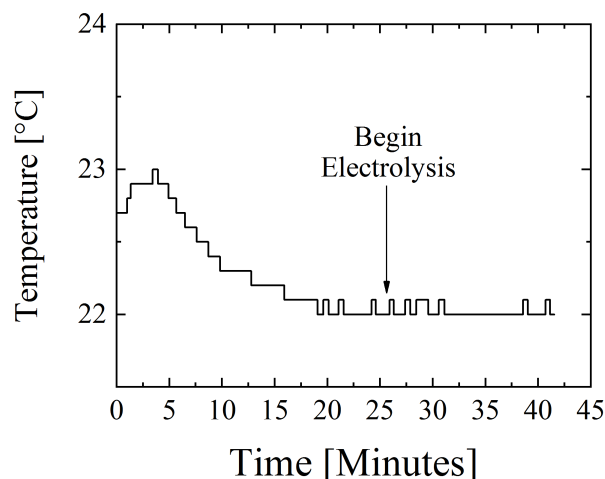
Figure 3.5: Temperature control during electrolysis while the PEC cell photoelectrode was illuminated using a light-emitting diode (LED) array (385, 405, and 470 nm). Illumination and cell temperature control started after 1 min of temperature recording with a set point of 22.0 °C. Continuous illumination and temperature control were maintained when electrolysis started at 26 min. Reproduced from Corson et al.[31] with the permission of AIP Publishing.

The reference electrode and thermistor are located in close proximity to the working electrode without blocking the light, as shown in the wireframe view of the working electrode chamber (Figure 3.4). The temperature can be monitored continuously and controlled within 0.1 °C during an electrochemical experiment using an external PID controller coupled to a Peltier element located directly behind the working electrode (part 2 in Figure 3.3). A complete parts list for the temperature control apparatus is given in Table 3.2. When a high-powered light source begins to illuminate the cell with a temperature setpoint of

22.0 °C, the electrolyte temperature experiences a small initial spike then can be stabilized at (22.0 ± 0.1) °C in less than 20 min after the light is turned on (Figure 3.5). In this study, we demonstrate the cell operating from 8.0 to 45.0 °C. However, the true operating range is much larger. When using aqueous electrolytes, the cell temperature is limited primarily by the phase transitions of water.

Table 3.2: Parts list for the PEC cell temperature control apparatus. All quantities needed are 1.

Purpose	Part Description	Supplier	Part No.
Temp Control	Peltier Element PID Panel Controller	Accuthermo Technology	ATEC302
Amplifier	Peltier Element H-Bridge Amplifier	Accuthermo Technology	FTX700D
	M6 Flat Bottom PEEK Nut for 2 mm OD	IDEX	P-357
Probe Fitting	1/4-28 Flat-Bottom ETFE Flangeless Ferrule for 2 mm OD	IDEX	P-314N
Temp Power	150 W, 12 V, 12.5 A Switching Power Supply	Mean Well	RS-150-12
Heat/Cool	30 mm × 60 mm, 131-couple, 15 A Peltier Cooler	Ferro Tec	72008/131/150B
Thermal Conductivity	Boron Nitride Thermal Grease	Chemtronics	CW7250-ND
Temp Sensor	5" × 1/16" Stainless Steel NTC Thermistor	Micro Lab	103
Sensor Cover	4.5" × 1/16" ID FEP Heat Shrink Caps	Tef-Cap	Custom

3.2 Comparison of the Custom PEC Cell to a Standard EC cell

Offset parallel electrodes represent the most straightforward geometry for front illumination of the electrode. However, they also introduce the possibility of non-uniform electric fields across the surface of the electrode. In fact, during initial trials, current instabilities were observed during constant voltage measurements below -0.7 Volts versus the reversible hydrogen

electrode (V_{RHE}) in 0.1 M KHCO$_3$. Electric field gradients can be suppressed by increasing electrolyte conductivity and thus concentration due to the screening of the electrode charge by the electrolyte ions. We observed a substantial reduction of current instabilities by increasing the concentration of the electrolyte to 1 M KHCO$_3$.

To determine the impact of offset parallel electrodes at this higher electrolyte concentration, the product distribution and current densities on Ag foil at four different potentials at ambient temperature were measured in the PEC cell as well as the EC cell with aligned parallel electrodes fabricated based on a previously reported design by Lobaccaro et al.[36] (Figure 3.6).
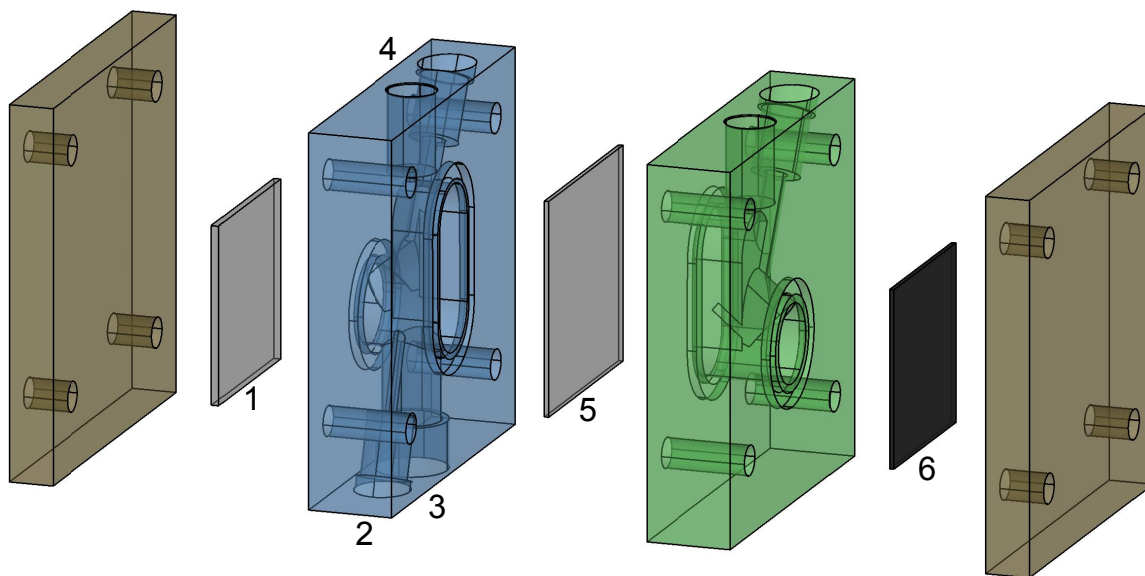
Figure 3.6: Schematic representation of the EC cell designed by Lobaccaro et al.[36] The working electrode (1) is in close proximity to the reference electrode (2) and is separated from the counter electrode (6) by a membrane (5). Gas enters through the glass frit at the bottom (3) and flows through tubing at the top (4) to the GC for product analysis. Reproduced from Corson et al.[31] with the permission of AIP Publishing.

Faradaic efficiencies for each product are plotted in Figure 3.7. The observed products were CO, H$_2$, and formate with an average total Faradaic efficiency of 99.9 % across both cells. The results in the PEC cell were remarkably similar to those measured in the EC cell; using a two-sample t-test assuming unequal variances with a significance level $\alpha = 0.05$, there was no statistical difference between the PEC cell and EC cell performance. In addition, there was no statistical difference between the average current densities at each potential between the PEC cell and the EC cell, which ranged from -0.9 to $-15\,\mathrm{mA\,cm^{-2}}$ (Figure 3.8). These results indicate that any electric field distribution differences due to the offset parallel electrode design of our cell does not impact the product current efficiencies or the overall current density.

Not only are the results in the PEC cell and EC cell nearly identical but they also agree with similar studies reported in the literature.[10] Although minor differences in exact product distributions between prior reports and ours are observed, the trend of CO production going
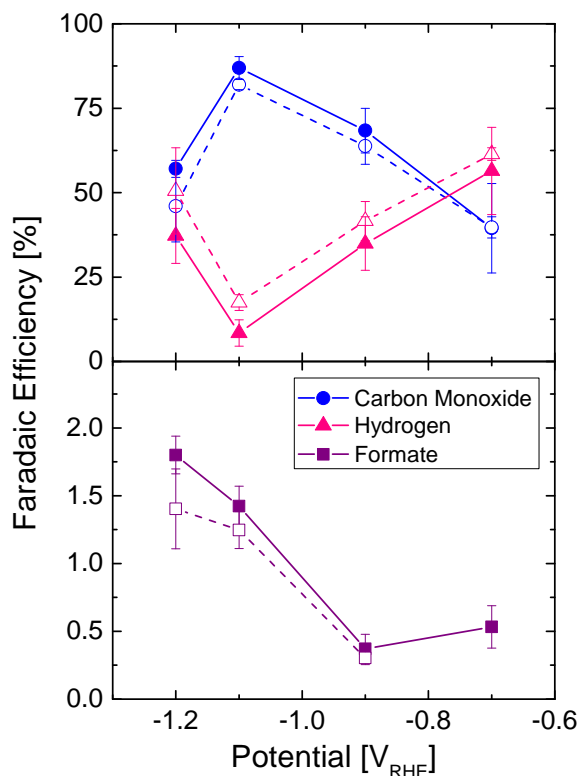
Figure 3.7: Faradaic efficiency for each CO$_2$R product after 15 min of electrolysis without illumination at various potentials on Ag foil in 1 M KHCO$_3$ with continuous CO$_2$ flow at 22.0 °C. The PEC cell results are plotted with filled symbols and connected with solid lines (——), and the EC cell results are plotted with open symbols and connected with dashed lines (- - -) to guide the eye. No formate was detected in the EC cell at −0.7 V$_{RHE}$. Adapted from Corson et al.[31] with the permission of AIP Publishing.

through a maximum at −1.1 V$_{RHE}$, with H$_2$ production going through a minimum, is in excellent agreement with prior work.[10] Similarly, the continually increasing trend of formate production with more cathodic potentials also matches those results. Variations in operating conditions may explain the differences between our studies and those previously published; Hatsukade et al.[10] used 0.1 M KHCO$_3$, flowed CO$_2$ through tubing at 20 SCCM, and operated for 1 h prior to product analysis.[10]

3.3 Temperature Variation During CO$_2$ Reduction

Like all gases, CO$_2$ solubility in aqueous electrolytes at moderate temperatures (0 to 50 °C) decreases with increasing temperature, which in turn can have a profound effect on the product distribution during electrolysis of CO$_2$-saturated solutions. Nevertheless, only a few studies have been published on the influence of temperature on CO$_2$ reduction.[37–42] To demonstrate the temperature control capabilities of our PEC cell, we studied constant potential (−1.1 V$_{RHE}$) electrolysis of CO$_2$-saturated 1 M KHCO$_3$ at a smooth Ag foil electrode
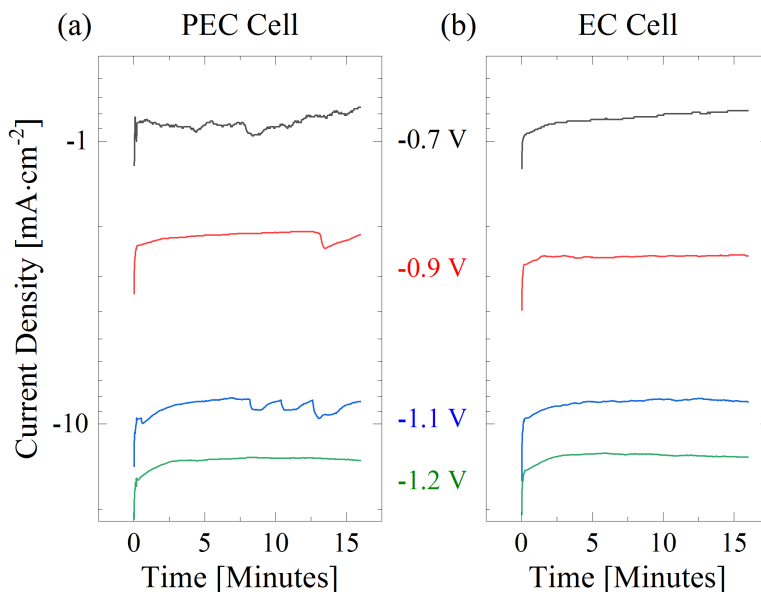
Figure 3.8: Current densities during electrolysis at various potentials—-0.7 V_{RHE} (black), -0.9 V_{RHE} (red), -1.1 V_{RHE} (blue), and -1.2 V_{RHE} (green)—over Ag Foil in 1 M $KHCO_3$ with continuous CO_2 flow at $22.0\,°C$ in the (a) PEC cell and in the (b) EC cell. Reproduced from Corson et al.[31] with the permission of AIP Publishing.

at 8.0, 22.0, 35.0 and $45.0\,°C$.

Faradaic efficiencies of CO, H_2, and formate at 8.0, 22.0, 35.0 and $45.0\,°C$ are presented in Figure 3.9 and indicate that the selectivity toward CO production is the highest at $8.0\,°C$ and decreases as the cell temperature is increased with a concomitant increase in H_2 selectivity. The formate production rate seems to be independent of temperature. Total current density and the partial current densities of CO, H_2, and formate increase with increasing temperature. In particular, H_2 partial current density, which increased by more than an order of magnitude from 8.0 to $45.0\,°C$, was influenced to a much greater extent than CO formation with increasing temperature. These trends are likely a result of diminished CO_2 solubility in the electrolyte, which decreases exponentially with temperature.[36] The lower CO_2 concentration in the electrolyte at higher temperature allows more active sites to reduce water to H_2. Azuma et al.[39] similarly saw CO decrease and H_2 increase from $2\,°C$ to room temperature on a Pd electrode in 0.05 M $KHCO_3$, although they observed formate decrease with increasing temperature.[39] Hori et al.[37] reported increasing H_2 production on Cu in 0.5 M $KHCO_3$ with increasing temperature (0 to $40\,°C$). While the total current efficiency of CO_2 reduction products decreased with increasing temperature, CO and C_2H_4 increased, formate remained constant, and CH_4 decreased with increasing temperature.[37] Clearly temperature can affect factors beyond solubility, such as reaction rates, coverage of adsorbed species, and reaction pathways, making it a vital parameter for understanding the fundamental mechanisms of CO_2 reduction.[36,37,39]
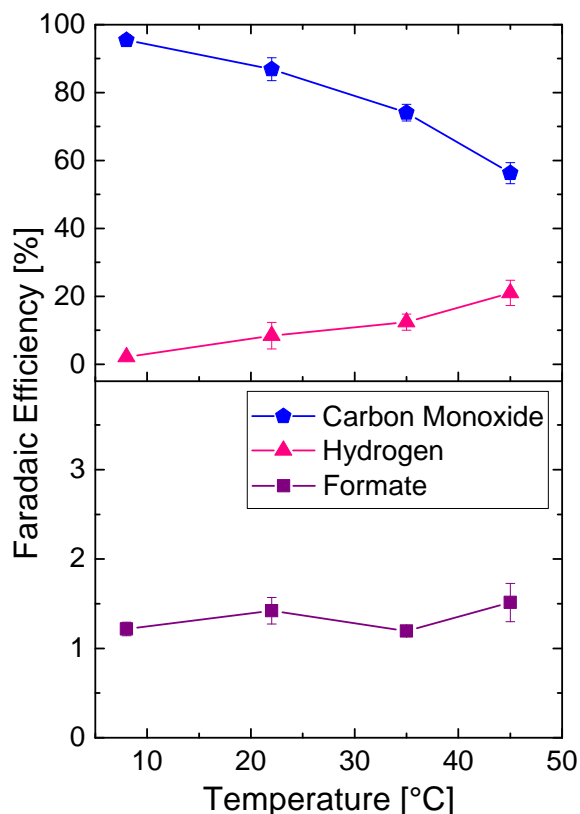
Figure 3.9: Faradaic efficiency for each CO_2R product after 15 min of electrolysis without illumination at -1.1 V_{RHE} over Ag foil in 1 M $KHCO_3$ with continuous CO_2 flow in the PEC cell at 8.0, 22.0, 35.0 and 45.0 °C. Reproduced from Corson et al.[31] with the permission of AIP Publishing.

3.4 Conclusions

We designed a PEC cell for studying challenging systems which evolve multiple gaseous or liquid products and possess low current densities and limiting reactant concentrations. While the cell can be adapted to many reactions, we demonstrate its efficacy for CO_2R in this chapter. We show our cell is effective for studying PEC CO_2 reduction and the influence of illumination on photoactive electrodes. We have shown that our PEC cell can match the results of a standard electrochemical cell while incorporating the additional features of temperature control and allowing front-illumination of the working electrode. The plasmonic nanostructured Ag cathode was shown to selectively promote CO_2 reduction to CO over H_2 evolution upon illumination. In Chapter 4, we will use this cell to quantify CO_2R product distribution at a Ag thin film plasmonic cathode.

3.5 Methods

3.5.1 (Photo)electrochemical Cells

A 0.5 M solution of K_2CO_3 (Alfa Aesar, 99.997 % metals basis) was prepared with 18.2 MΩ ultrapure water from a Millipore system, which became 1 M $KHCO_3$ when saturated with CO_2 (Praxair, 99.999 %). The pH of the saturated electrolyte was 7.57 (Hanna Instruments, pH meter 9124). In the PEC cell, the working chamber was filled with 2.3 mL of the electrolyte and the counter chamber with 0.8 mL. Both chambers of the standard, dark EC cell, designed by Lobaccaro et al.[36] and used here as a comparison to the PEC cell, were filled with 1.9 mL of the electrolyte (Figure 3.6).

The Ag foil cathode (thickness 0.1 mm, Alfa Aesar, 99.998 % metals basis) was mechanically polished (Norton T401, 2000 grit) before each use. The counter electrode was a platinum foil and the reference electrode was a leak-free Ag/AgCl electrode (Innovative Instruments, LF-1, 3.4 M KCl). The working and counter chambers were separated by an anion-exchange membrane (AGC Engineering, Selemion AMV).

The cell was sonicated in 20 v/v % nitric acid and ultrapure water after fabrication and sonicated in ultrapure water before each use. The chambers of the cell were rinsed with 0.05 M K_2CO_3 before adding new electrolyte between consecutive electrolysis measurements on the same cathode.

3.5.2 Temperature Control

A planar Peltier element, also known as a thermoelectric device or thermoelectric cooler (TEC), (Ferro Tec, 72008/131/150B) was compressed between the aluminum back plate and the cathode. The back plate was attached to a heat sink with a mounted fan (Deep Cool, GAMMAXX 400). The interfaces between the heat sink, back plate, and Peltier element were coated with thermal paste (Chemtronics, CW7250). A thermistor (Microlab, Model 103) covered with a heat-shrink fluorinated ethylene propylene (FEP) probe cover (Tef-Cap Industries) monitored the temperature of the catholyte through the cell side-port. A PID temperature controller (Accuthermo Technology, ATEC302) was used to maintain the catholyte at a constant temperature set point throughout electrolysis. If temperature control is not needed, the Peltier element and heat sink can be removed. In this case, the back plate can be fabricated from a variety of materials including aluminum and polycarbonate.

3.5.3 Product Analysis

The assembled cell was connected to a gas manifold with leak-tight fittings (IDEX, P-210) as shown in (Figure 3.10). A mass flow controller (MFC) (Alicat, MC-10SCCM-D) set the gas flow rate into the cell. A mass flow meter (MFM) (Alicat, M-50SCCM-D) placed in line before the gas entered the GC gas-switching valve verified the flow of the controller and was used as a check to ensure the system was leak-free. A CO_2 flow rate of 5.0 SCCM was used for all experiments reported in this study. The CO_2 is bubbled into the electrolyte through a glass frit (Ace Glass, Porosity E).
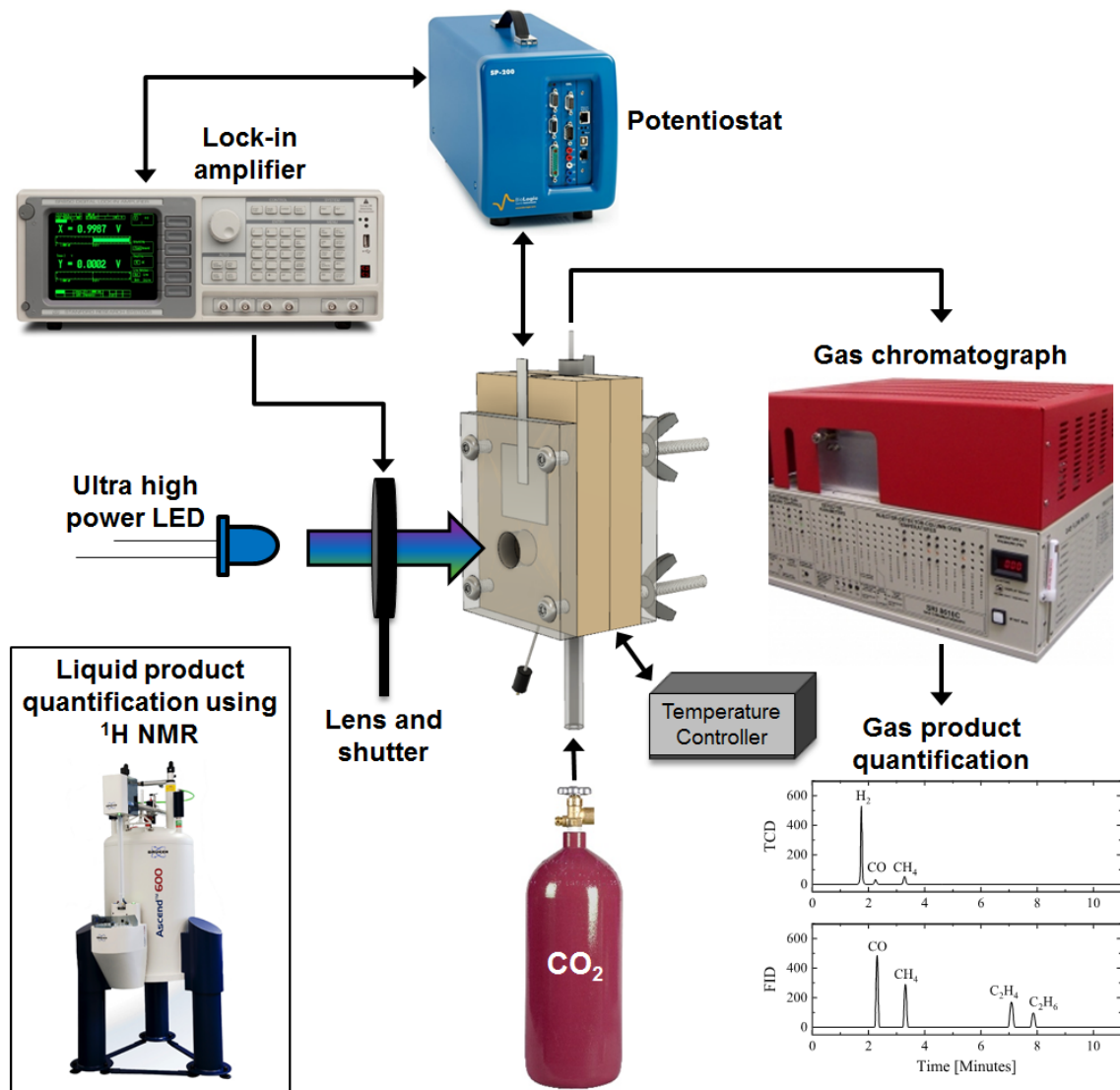
Figure 3.10: Photoelectrochemical CO_2R apparatus diagram. CO_2 is delivered to the PEC cell through the glass frit at the bottom. The flow carried evolved gases to the GC which outputs a chromatogram to a computer. A potentiostat (BioLogic Science Instruments, SP-300) controls the cell potential and masures the resulting current. A PID temperature controller maintains a constant temperature in the catholyte. A LED illuminates the cell through a condenser lens and shutter. The shutter is controlled by a lock-in amplifier, which also extracts photocurrent from the potentiostat signal, during chopped-light measurements.

The bubbled CO_2 served to carry gaseous CO_2R products to a GC (SRI Instruments, Multiple Gas Analyzer #5) with a 12 ft HayeSep D column, argon carrier gas, and a gas-switching valve with a 1 mL sample loop was used for gaseous product analysis. Products separated by the column flow through a thermal conductivity detector (TCD) that detects H_2 followed by a methanizer that converts CO and CO_2 to CH4 and a flame ionization detector (FID) that detects CH_4, C_2H_4, and C_2H_6. The GC was calibrated with a set of three calibration gases containing a known mixture of H_2, CO, CH_4, C_2H_4, and C_2H_6 in a balance of CO_2 (Airgas) at concentrations between 100 and 8000 ppm. A linear calibration curve for each product was calculated from points representing the average of runs repeated multiple times across several days, with the intercept set at zero and R^2 values of 99.89 to 99.99 %.

^{1}H NMR spectroscopy (500 MHz Bruker Avance III) was performed for liquid product analysis. 400 µL of an electrolyte sample collected at the end of an experiment was combined with 50 µL of deuterium oxide (D_2O) (Sigma Aldrich, 151882) as the internal solvent lock and 50 µL of an internal standard comprised of 1 mM phenol in water. A proton water suppression method with a 60 s acquisition time was averaged 16 times. Formate was quantified by comparing the integrated area of the product peak to that of phenol.[3]

Gas Chromatography Theory

GC is an analytical technique for separating and quantifying chemical compounds that can be vaporized without decomposition. A GC separates compounds by retention time in a capillary or packed column then uses one or more detectors to identify eluted compounds based on the elution time of standard compounds.

There are seven major parameters that affect GC performance—stationary phase, film thickness, internal diameter, column length, temperature, carrier gas type, and carrier gas velocity. As an aggregate of all these factors, the resolution equation

$$R = \left(\frac{\sqrt{N}}{4}\right)\left(\frac{k}{k+1}\right)\left(\frac{\alpha-1}{\alpha}\right) \tag{3.1}$$

where N is the number of theoretical plates, k is the retention factor, and α is the selectivity is used to evaluate the performance of a GC separation. $R = 1.5$ is the goal for high resolution while keeping run times low.

More efficient columns have higher N and narrower peak widths at a given elution time. The efficiency of a column is evaluated by determining the number of theoretical plates N.

$$N = \frac{L}{H} = 5.545\left(\frac{t_R}{w_h}\right)^2 \tag{3.2}$$

where L is column length, H is the height of a theoretical plate, t_R is the retention time, w_h is the peak width at half maximum, and 5.545 is 8 ln 2. A theoretical plate is a region where two phases establish equilibrium, and the height H (sometimes referred to as the height equivalent of a theoretical plate (HETP) is given by the van Deemter Equation

$$N = A + \frac{B}{\bar{u}} + C\bar{u} \tag{3.3}$$

where A is the term for peak broadening by turbulent diffusion, B is the term for broadening by longitudinal diffusion, C is the broadening due to resistance to mass transfer, and $\bar{u}$ is the carrier gas velocity. The H versus $\bar{u}$ van Deemter plot is a hyperbola that gives the optimum carrier velocity at $\bar{u}_{\mathrm{opt}} = \sqrt{B/C}$. Generally, narrower columns have higher efficiency because they have more theoretical plates per meter but lower sample capacity.

The retention of a species in the column is measured by k, the ratio of the time that a species spends in the stationary phase to the time spent in the mobile phase.

$$k = \frac{t'_R}{t_M} \tag{3.4}$$

Thicker films give more retention, and to a lesser extent columns with smaller inner diameters produce larger k values because there is less available mobile phase in the column.

The selectivity α of a column describes how well a column separates two components of a sample mixture and is given by

$$\alpha = \frac{t'_{R(2)}}{t'_{R(1)}} \tag{3.5}$$

where species (1) elutes before species (2) so that $\alpha > 1$. The selectivity of a GC is most affected by the stationary phase of the column. The stationary phase should have similar polarity to the sample components so that there will be more retention and better separation. The intermolecular forces that may be involved are hydrogen bonding, London dispersion, dipole-dipole, dipole-induced dipole, and size/shape selectivity.[43]

The GC column used to separate the CO_2R product gases in this study is a 1/8 in inner diameter stainless steel column packed with Hayes Separations' porous divinylbenzene polymer HayeSep D. The nonpolar polymer is designed to separate light gases through Van der Waals forces.
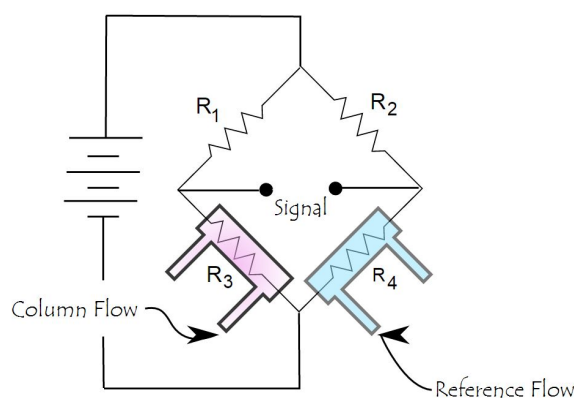
Figure 3.11: Schematic representation of the wheatstone bridge in a TCD Reprinted with permission from Mattj63 and Wikimedia Commons.

A TCD is used in this study to detect H_2 eluting from the column by detecting changes in thermal conductivity of column eluents versus argon reference gas. A TCD generally uses a Wheatstone bridge circuit (Figure 3.11) in a controlled temperature environment to measure

conductivity changes in the eluent. When the thermal conductivity of the column eluent gases flowing over resistor R_3 is different from the thermal conductivity of the reference gas flowing over resistor R_4, a voltage signal is generated in the Wheatstone bridge. Since the thermal conductivity of H_2 is larger than that of the argon reference gas, the voltage drops and the signal is negative. The difference in thermal conductivity between the gaseous hydrocarbon products in this study and the argon carrier gas is not great enough to quantify or even reliably detect them using a TCD. The hydrocarbon components could be detected using a TCD if helium was used as the carrier gas, but the hydrocarbon components can be detected with better resolution using a FID.

A FID detects the ions produced by the combustion of organic compounds in a H_2 flame. The FID in this study is preceded by a methanizer that hydrogenates CO to methane and allows low concentrations of CO to be detectede by the FID.

3.5.4 Electrochemical Measurements

Electrochemical measurements were controlled with a Bio-Logic SP-300 potentiostat. Impedance spectroscopy was used before each experiment to determine the uncompensated electrolyte resistance (R_u). The potentiostat compensated for 85% of R_u during electrolysis, where the set potential was applied for 16 min with a GC injection occurring after 15 min. Reported potentials have been converted to V_{RHE} scale and adjusted for the final 15% of R_u. Each electrochemical experiment was repeated at least three times; reported results are the average of all runs with error bars showing one standard deviation.

3.5.5 Photoelectrochemical Measurements

The Ag photoelectrode was illuminated by a collimated array of three LEDs (Mightex) with a combined power of 3 W cm^{-2} at wavelengths of 385, 405, and 470 nm, which were selected due to their proximity to the reported surface plasmon resonance of Ag.[20] Electrolysis with product analysis was performed as described above under continuous illumination.

Chapter 4

Directing Selectivity of Electrochemical CO₂ Reduction Using Plasmonics[3]

Abstract

Catalysts for electrochemical carbon dioxide reduction in aqueous electrolytes suffer from high energy input requirements, competition with hydrogen evolution reaction (HER) from water reduction, and low product selectivity. Theory suggests that plasmonic catalysts can be tuned to selectively lower the energy barrier for a specific reaction in a set of competitive reactions, but there has been little experimental evidence demonstrating plasmon-driven selectivity in complicated multi-electron electrochemical processes. Here, the photoactivity at a plasmonically active Ag thin film cathode at small cathodic potentials selectively generates CO while simultaneously suppressing H_2 production. At larger cathodic potentials the photoactivity promotes production of methanol and formate. Methanol production is only observed under illumination, not in dark conditions. The preference of the plasmonic activity for carbon dioxide reduction over HER and the ability to tune plasmonic activity with voltage demonstrates that plasmonics provide a promising approach to promote complex electrochemical reactions over other competing reactions.

Summary

We use a Ag cathode without a supporting absorber to probe the effect of plasmonic excitation on CO_2 reduction at several potentials. Ag is an ideal heterogeneous catalyst for plasmonic electrochemical reduction of CO_2 because of its well-understood dark CO_2 electrocatalytic performance,[2,10] and the resonant excitation of Ag surface plasmons occurs upon illumination with near-ultraviolet (UV)-visible light irradiation at 340 to 400 nm (3.1 to 3.6 eV).[20] Moreover, due to the electronic band structure of Ag, surface plasmon resonance (SPR) is predicted to generate high energy hot electrons,[44] making this metal appropriate

---

[3]This chapter describes joint work with Elizabeth Corson.

for a reduction reaction study. Many transition metals are poor CO_2 reduction catalysts because they produce primarily H_2, but Ag cathodes promote CO production at ambient temperature and pressure with reasonable CO formation selectivity over HER, albeit at large overpotentials (approximately 1 V) in near-neutral-pH aqueous electrolyte.[2,10] Ag cathodes also produce small amounts of formate at potentials more cathodic than -0.6 Volts versus the reversible hydrogen electrode (V_{RHE}) and exceedingly small amounts of methanol, ethanol, and methane at highly cathodic potentials (more cathodic than -1.3 V_{RHE}).[10]

Here, we show that the plasmonic activity over a polycrystalline Ag thin film cathode is significant and selective for CO_2 reduction while suppressing HER at low applied cathodic potentials. H_2 production is also suppressed under illumination of a Ag cathode in CO_2-free (Ar-saturated) electrolyte, resulting in a decrease in activity. An illuminated Ag cathode generates CO at $> 90\%$ Faradaic efficiency at much lower overpotentials than an unilluminated Ag cathode. Methanol production is not observed without illumination at cathodic potentials down to -1.1 V_{RHE}, but methanol production under illumination is produced at 0.1 to 2.0% Faradaic efficiency between -0.8 and -1.1 V_{RHE}, which is an unprecedented methanol Faradaic efficiency for Ag cathodes. Interestingly, the enhancement in CO production is only observed at -0.8 V_{RHE} and potentials more anodic while the methanol production only occurs at -0.8 V_{RHE} and potentials more cathodic. This is the first known example of using applied voltage to control the product selectivity of plasmonic-driven reactions, indicating that voltage bias is an important variable in tuning and understanding plasmonic selectivity in complex electrochemical reactions. Additionally, the combined enhancement of CO_2 reduction and suppression of HER via plasmonic catalysis may be an important breakthrough in directing selective aqueous electrochemical CO_2 reduction.

4.1   Synthesis and Characterization of Ag Thin Films
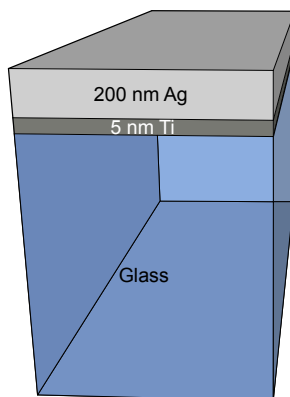
Figure 4.1: Diagram of the Ag thin-film cathode showing e-beam deposited 200 nm Ag on 5 nm Ti on a glass slide. Reprinted with permission from Creel et al.[34] Copyright 2019 American Chemical Society.

We fabricated the Ag photocathodes by electron beam (e-beam) evaporating Ag onto a glass slide substrate using titanium as an adhesion layer (Figure 4.1) followed by electrochemi-

cal conditioning of the surface at -1.1 V_{RHE} in aqueous CO_2-saturated potassium bicarbonate ($KHCO_3$) electrolyte. Electrochemical conditioning of the electrode was necessary due to the evolution of the electrode's optical properties and morphology with CO_2 electrolysis. The as-deposited Ag film exhibited a weak absorption peak at 346 nm (Figure 4.2), that corresponds to the Ag surface plasmon resonance.[20] After only one min of CO_2 electrolysis, the absorption of the rinsed and dried cathode increased across the spectrum with the plasmonic peak broadening and red-shifting. The plasmonic absorption peak continued to widen and move toward larger wavelengths with further CO_2 electrolysis until it reached a steady state between 30 and 60 min of electrolysis with an absorption maximum at 351 nm (Figure 4.2). No change in the plasmonic absorption occurred when the electrode was immersed in electrolyte without applied bias. We hypothesized that the large applied voltage caused the Ag nanostructures on the rough evaporator-deposited surface to ripen into larger, more stable nanostructures.[45,46]
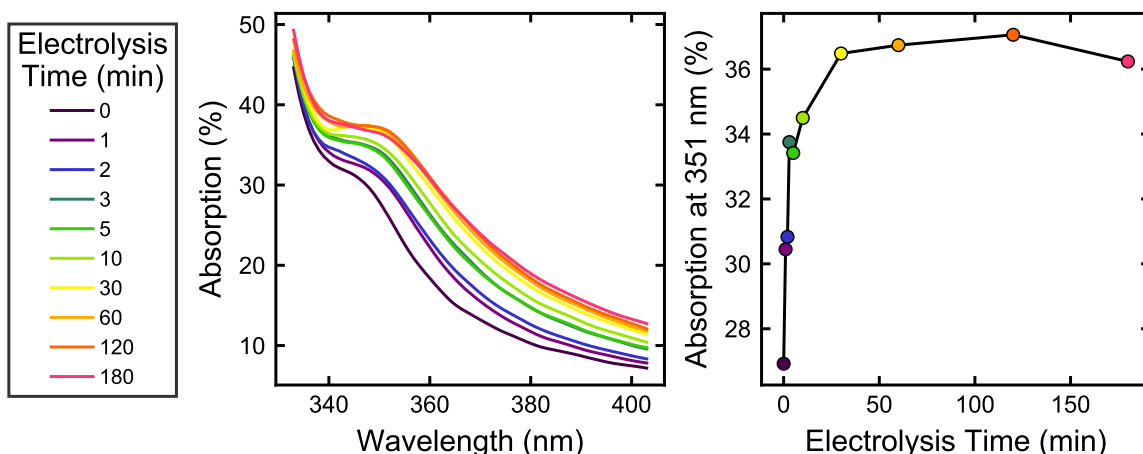
Figure 4.2: Evolution of the UV-visible absorption spectra and the absorption at 351 nm of a thin film Ag cathode after biasing at -1.1 V_{RHE} in CO_2-saturated 1 M $KHCO_3$ for various times. Absorption is calculated as $100\% - \%R$ where $\%R$ is the total reflection measured by an integrating sphere. Reprinted with permission from Creel et al.[34] Copyright 2019 American Chemical Society.

To test this hypothesis, we measured the electrochemical double layer capacitance as a proxy for elctrochemical surface area (ECSA) at various intervals over the electrolysis time. First, the Faradaic current due to double layer charging in cyclic voltammetry (CV) was measured at a series of increasingly rapid scan rates (Figure 4.3a). The capacitance is the y-intercept of the best-fit line of the charging current versus scan rate (Figure 4.3b). The capacitance was measured for the same electrode after various electrolysis times. Each measured capacitance was normalized to the capacitance of the as-deposited electrode for the relative ECSA (Figure 4.3c). The ECSA decreases then stabilizes over electrolysis time, consistent with the coarsening hypothesis from absorption measurements.

SEM images before and after 45 min of CO_2 electrolysis show nodule-like features of $10 - 100$ nm on the electrode surface, but there is little noticeable difference between them (Figures 4.4a and 4.4b). AFM topographic images both before and after 45 min of electrolysis
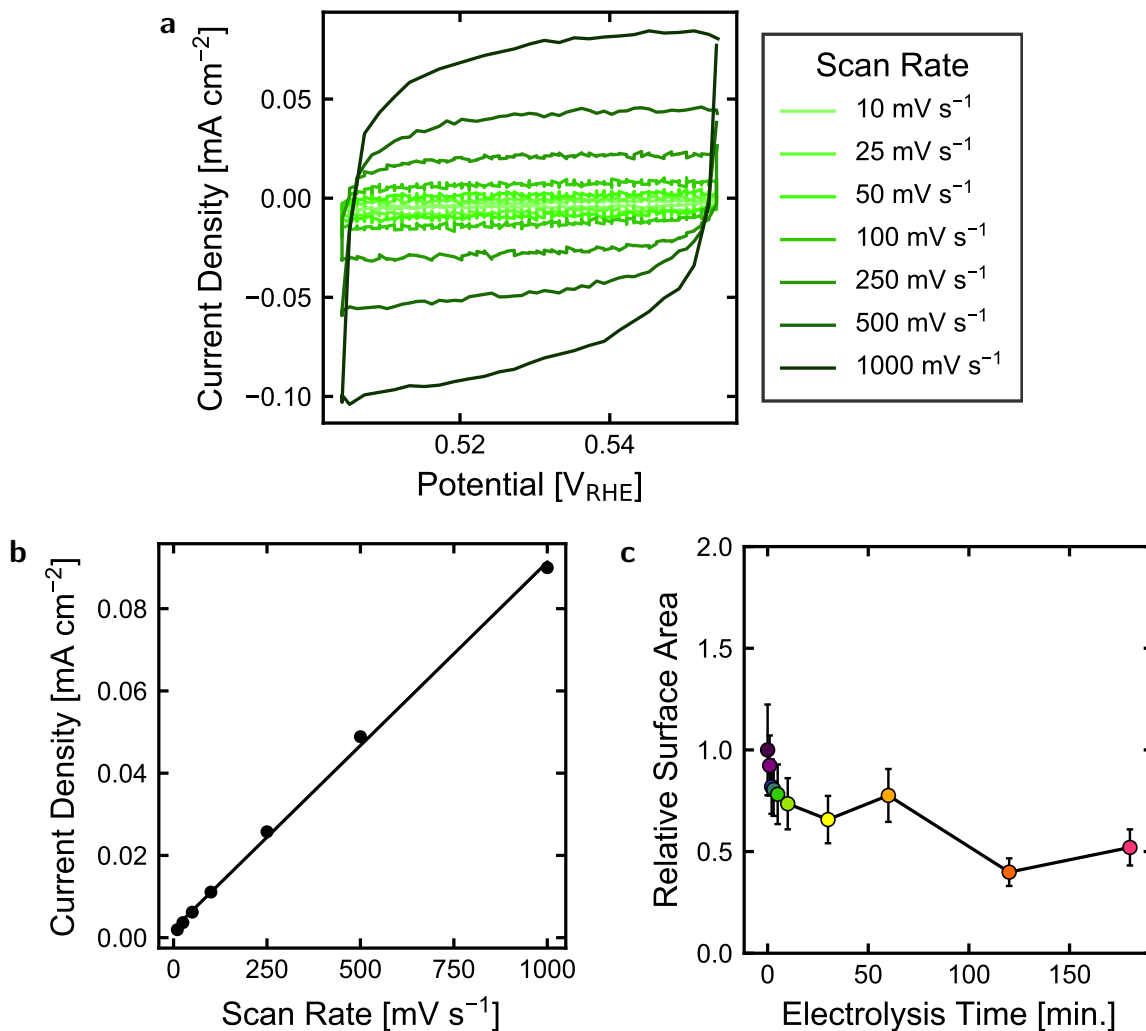
Figure 4.3: Relative ECSA measurement by capacitive cycling measurements on a Ag cathode. (a) Capacitive cycles over a 50-mV non-Faradaic region at a series of rapid scan rates after 0 min of electrolysis. Only the third cycle for each scan rate is shown here. (b) Capacitive current for a series of scan rates after 0 min of electrolysis where the y-intercept of the best-fit line gives the capacitance. (c) Capacitance relative to the unconditioned (electrolysis time = 0) electrode capcitance gives the relative ECSA as a function of electrolysis time. Error bars represent the standard deviation of experiments performed in triplicate on a single electrode. Reprinted with permission from Creel et al.[34] Copyright 2019 American Chemical Society.

a

b
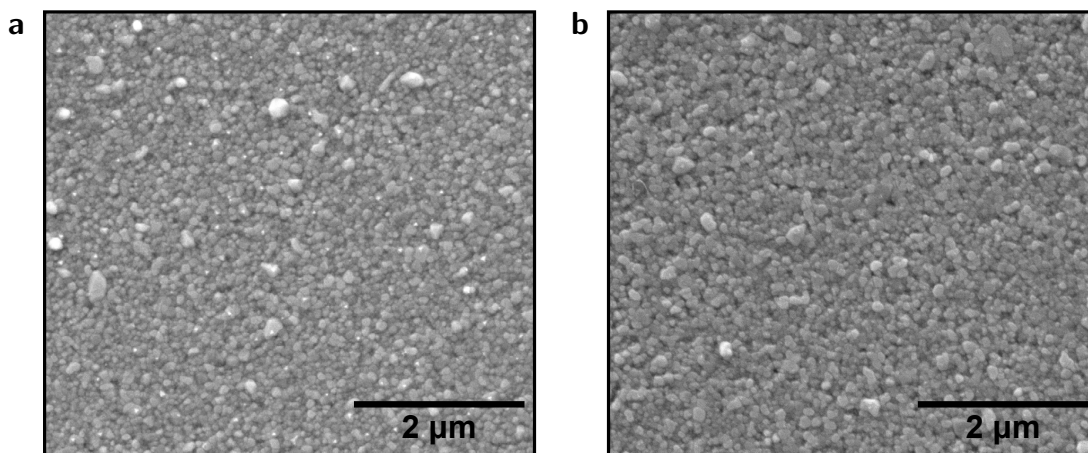
Figure 4.4: scanning electron microscopy (SEM) image of the thin film Ag cathode (a) as-deposited and (b) after biasing at -1.1 V$_{RHE}$ for 45 min. Reprinted with permission from Creel et al.[34] Copyright 2019 American Chemical Society.

mirror the feature size and similarity of SEM images (Figures 4.5a and 4.5b, even though the electrode surfaces appear mirror-like to the naked eye. AFM root mean square (RMS) surface roughness measurements before and after electrochemical conditioning—6.0 nm and 4.4 nm, respectively—indicate a slight decrease in surface roughness, matching the ECSA measurements. A grain size analysis using the watershed method detected the grains shown in purple in Figures 4.5c and 4.5d and indicated that the grain size distribution broadens slightly, increasing the population of both large and small features, after electrochemical conditioning (Figure 4.5e).

4.2 CO$_2$ Electrochemical Reduction Product Measurements

The gaseous products of CO$_2$ reduction over the Ag cathode were measured by an in-line gas chromatograph (GC) while applying a constant voltage.[10] The liquid products were measured by proton nuclear magnetic resonance (^{1}H NMR) of the electrolyte after the electrochemical measurement was complete. The cathode was continuously illuminated from the front with 170 mW cm^{-2} incident light intensity from a 365 nm light-emitting diode (LED), which was selected given its proximity in energy to the plasmon resonance peak (351 nm, Figure 4.2) of our conditioned Ag cathodes, or left unilluminated for the "dark" control. No high-power LEDs (2 to 3 mW cm^{-2}) are available at wavelengths below 365 nm, limiting the range of photon energies studied here to the visible spectrum, which is interesting for solar-driven processes. Our electrolysis cell was specifically designed to ensure precise temperature control, and all measurements, both illuminated and in the dark, were performed at (22.0 ± 0.1) °C.[31]

The difference in product distributions between the illuminated and dark conditions is dramatic and dictated by the applied potential. At potentials more anodic than -0.9 V$_{RHE}$, the Faradaic efficiency and production rate of CO is significantly enhanced when the Ag
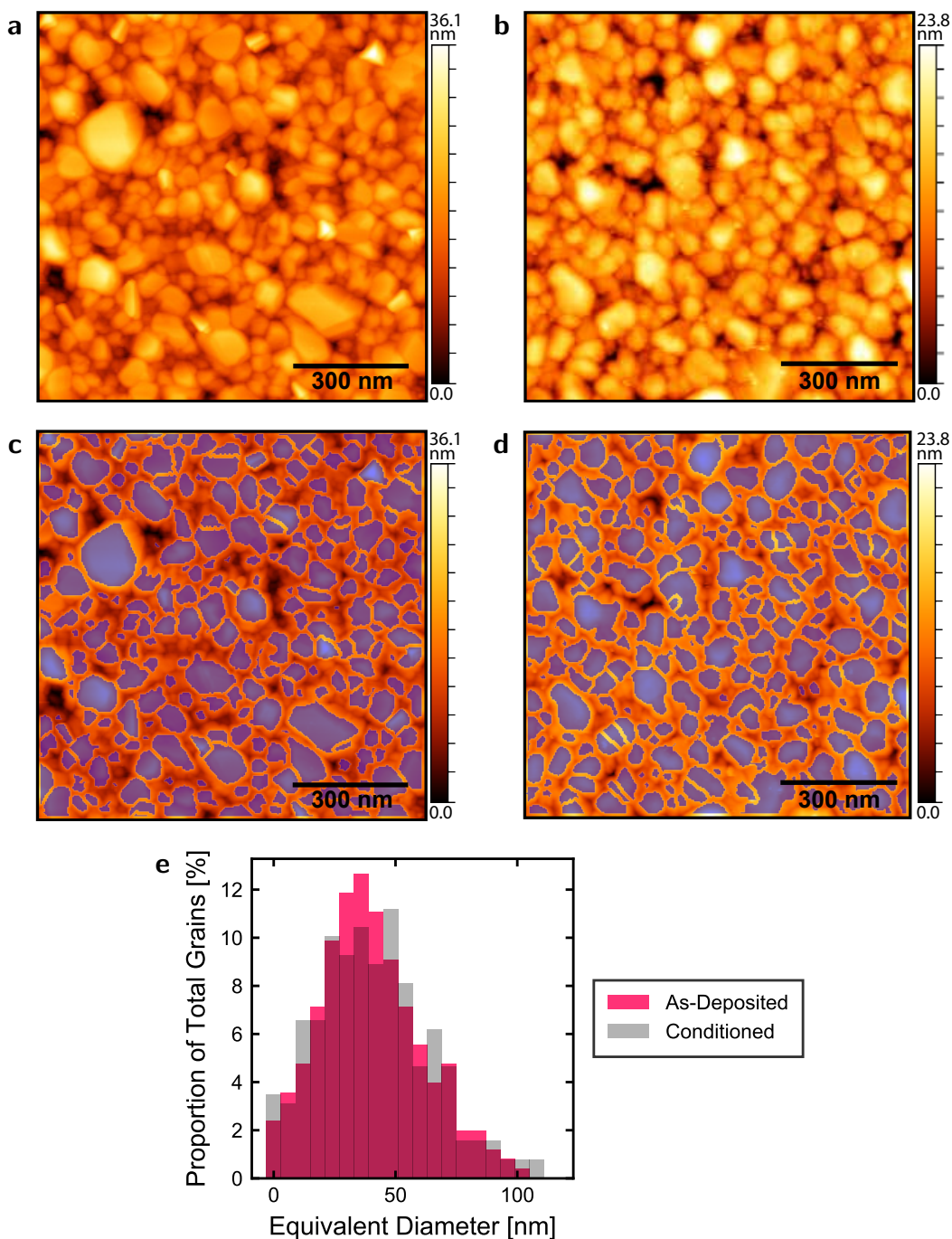
Figure 4.5: atomic force microscopy (AFM) topographic images of the thin film Ag cathode (a) as-deposited and (b) after biasing at -1.1 V$_{\mathrm{RHE}}$ for 45 min. Grains detected by the watershed algorithm (purple) in the AFM image of the cathode (c) as-deposited and (d) after biasing at -1.1 V$_{\mathrm{RHE}}$ for 45 min. (e) Comparison of the grain size distribution on the cathode in terms of equivalent diameter—the diameter of a disk with the same projected area as the grain—"As-Deposited" and after biasing at -1.1 V$_{\mathrm{RHE}}$ for 45 min ("Conditioned"). Reprinted with permission from Creel et al.[34] Copyright 2019 American Chemical Society.

plasmonic catalyst is illuminated (Figures 4.6a and 4.7a). The most dramatic enhancement of CO occurs at the lowest potential used in this study, -0.6 V$_{RHE}$, where the Faradaic efficiency of CO increases from 17 % in the dark to 95 % when the cathode is illuminated. The increase in CO Faradaic efficiency reflects a 3, 5, and 16-fold increase in the CO production rate in the light versus the dark at -0.8, -0.7, and -0.6 V$_{RHE}$, respectively (Figure 4.7a). The decrease in H$_2$ Faradaic efficiency when the Ag cathode is illuminated at these small cathodic potentials (Figure 4.6a) stems not only from the increase in CO production but also a notably lower rate of H$_2$ generation in the light at these potentials (Figure 4.7a).

The cathodic sweep of a CV in CO$_2$-saturated 1 M KHCO$_3$ predictably shows increased cathodic current and a decreased onset potential when the Ag cathode is illuminated (Figure 4.8a). CO is the only product detected over the illuminated Ag cathode at -0.37 V$_{RHE}$ while no products were detected at the same potential without illumination. CVs in Ar-saturated 0.5 M potassium carbonate (K$_2$CO$_3$) show the opposite trendcathodic current decreases under illumination relative to the unilluminated electrode (Figure 4.8b). Though the same starting electrolyte was used in both the Ar- and CO$_2$-saturated CVs, the presence of CO$_2$ lowers the pH, as noted in the legends of Figure 4.8. Similar results are observed in CO$_2$- and Ar-saturated 0.5 M sodium perchlorate (NaClO$_4$) (Figure 4.9), indicating that a plasmon interaction with adsorbed bicarbonate (which could plausibly be adsorbed to, and therefore blocking, active sites) is likely not impacting these results. Therefore, H$_2$ production is suppressed on a plasmonic Ag cathode regardless of the presence of CO$_2$ or specific electrolyte anions.

A plausible explanation for this CO formation selectivity over HER is that the plasmonically generated hot electrons are selectively, rather than indiscriminately, transferred to molecules adsorbed on the metal surface. In the case of plasmonic electrochemical CO$_2$ reduction, there are several leading theories for the mechanism of plasmonic-hot-electron-driven photocatalysis that may be valid in this photoelectrochemical system.[47–52] In an indirect charge transfer mechanism, SPR excites a hot electron in the Ag catalyst; subsequently, that hot electron is transferred to unoccupied molecular orbitals of an adsorbate. In a direct charge transfer mechanism, SPR induces direct charge transfer in the metal-adsorbate complex from an electronic state with primarily Ag character to a hybridized orbital with primarily CO$_2$-reduction-intermediate character.[51,52] In a transient negative ion (TNI) mechanism, plasmonic hot electrons are generated on the Ag, populate unoccupied adsorbate states for a short time, and then return to the metal, leaving the adsorbate molecule in a vibrationally excited state with increased reactivity (Figure 4.10).[47–50] These three mechanisms are all consistent with the transfer of electron density to adsorbed CO$_2$ or an intermediate in the pathway to selectively form CO, formate, or methanol, as is observed in this study.

The plasmonic suppression of HER superficially appears to be a completely different process than the promotion of CO$_2$ reduction. However, it is possible that H$_2$ is suppressed because protons (or hydroxide ions) or water molecules are selectively purged from the surface of the Ag cathode through desorption induced by electronic transitions (DIET), the basis for the TNI mechanism discussed above.[50,53] In the DIET mechanism, the H$_2$ precursor is excited electronically through the transient population of unoccupied adsorbate orbitals. The DIET mechanism diverges from the TNI mechanism in the result of the vibrational excitation. In DIET, the adsorbate overcomes the surface binding energy and desorbs rather
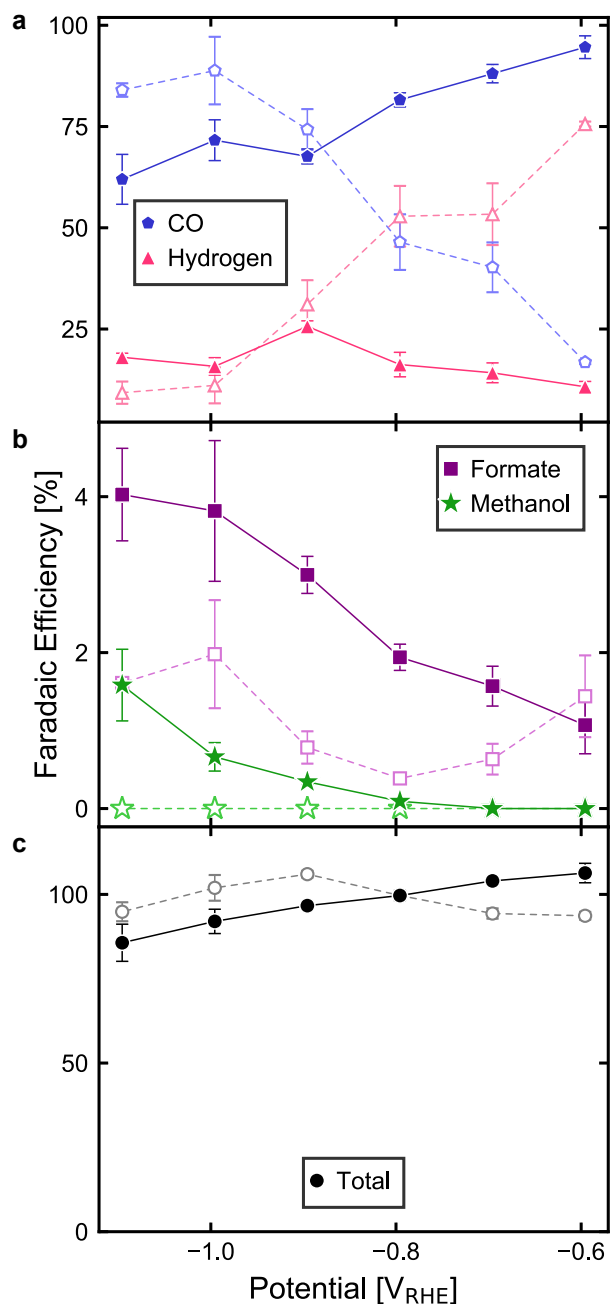
Figure 4.6: Faradaic efficiency for each carbon dioxide reduction (CO$_2$R) product over an illuminated and dark Ag cathode. Filled symbols with solid lines represent data collected under 365 nm LED illumination at 170 mW cm^{-2}. Open symbols with dashed lines represent data collected without illumination. (a) Faradaic efficiencies of CO and H$_2$ at a range of applied potentials. (b) Faradaic efficiencies of formate and methanol at a range of applied potentials. No methanol was detected in the dark. (c) Total Faradaic efficiencies at a range of applied potentials. Error bars represent the standard deviation of experiments performed in triplicate on three different electrodes. Reprinted with permission from Creel et al.[34] Copyright 2019 American Chemical Society.

47
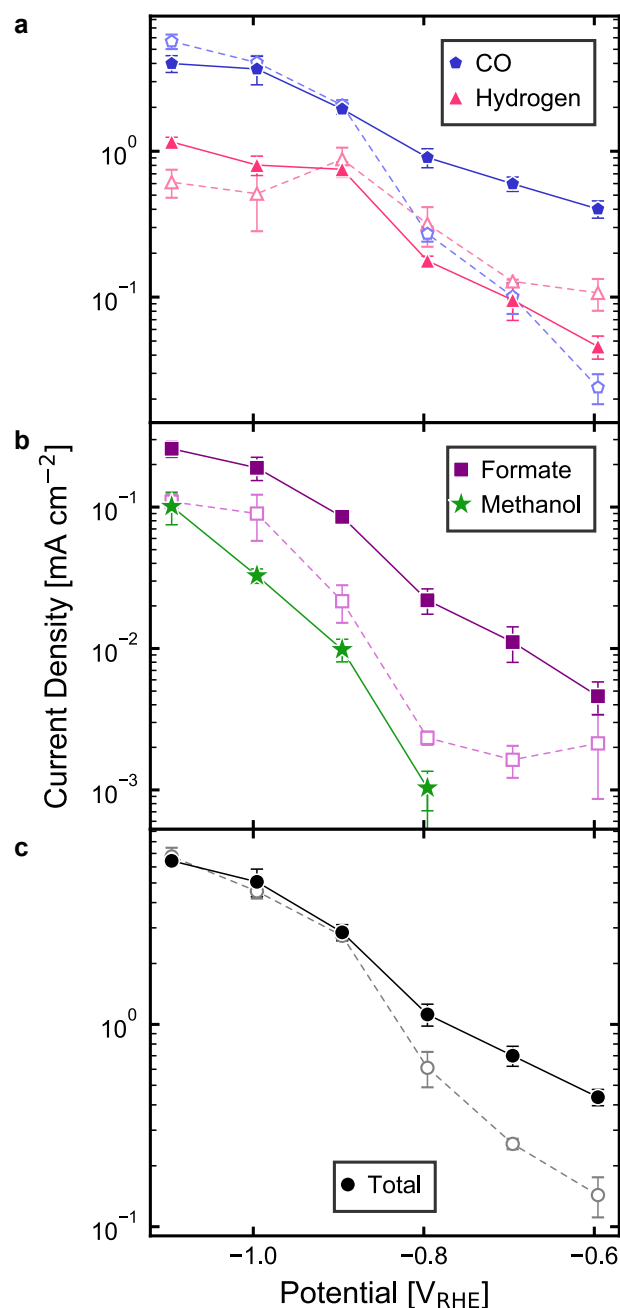
Figure 4.7: Tafel plot of the partial current density for each CO$_2$R product over an illuminated and dark Ag cathode. Filled symbols with solid lines represent data collected under 365 nm LED illumination at 170 mW cm^{-2}. Open symbols with dashed lines represent data collected without illumination. (a) Partial current densities of CO and H$_2$ at a range of applied potentials. (b) Partial current densities of formate and methanol at a range of applied potentials. No methanol was detected in the dark. (c) Total current densities at a range of applied potentials. Error bars represent the standard deviation of experiments performed in triplicate on three different electrodes. Reprinted with permission from Creel et al.[34] Copyright 2019 American Chemical Society.
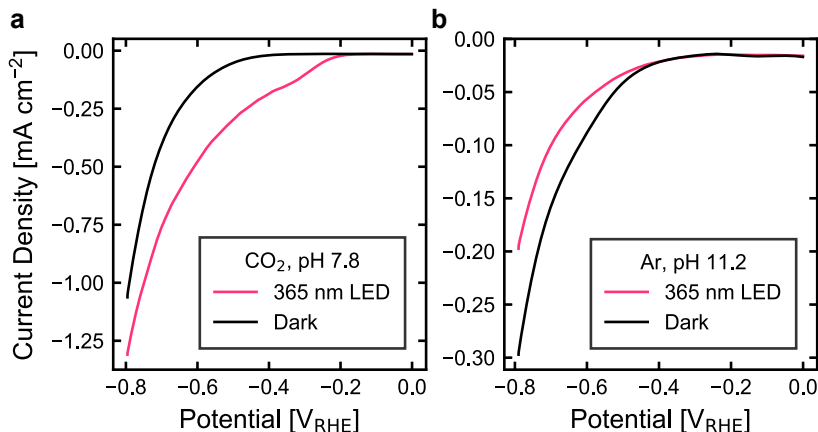
Figure 4.8: Cathodic voltage sweep at 100 mV s^{-1} at an illuminated and dark Ag cathode in (a) CO$_2$- and (b) Ar-saturated 0.5 M K$_2$CO$_3$ under 365 nm LED light at 170 mW cm^{-2}. The voltage ranges were selected to ensure that no Ag oxidation occurred at the anodic limit and to include all potentials where a photoeffect is observed for CO and H$_2$ in CO$_2$-saturated electrolyte at the cathodic limit. Reprinted with permission from Creel et al.[34] Copyright 2019 American Chemical Society.
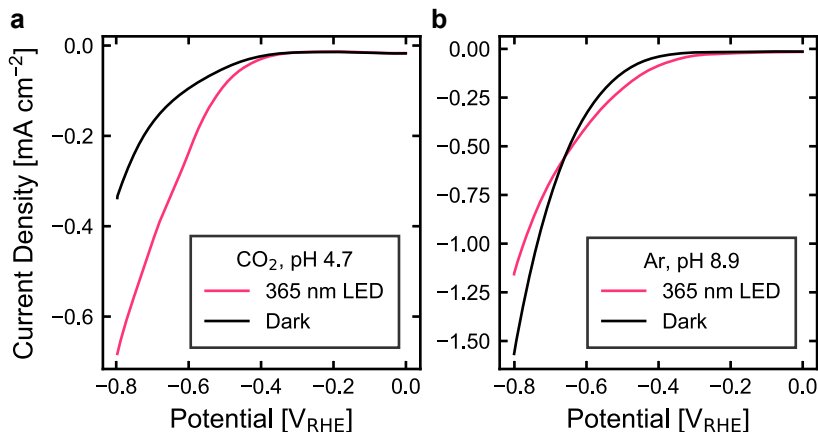
Figure 4.9: Cathodic voltage sweep at 100 mV s^{-1} over illuminated and dark Ag cathodes in (a) CO$_2$- and (b) Ar-saturated 0.5 M NaClO$_4$ under 365 nm LED light at 170 mW cm^{-2}. The voltage ranges were selected to ensure no Ag oxidation occurred at the anodic limit and to include all potentials where a photoeffect is observed for CO and H$_2$ in CO$_2$-saturated K$_2$CO$_3$ at the cathodic limit. Reprinted with permission from Creel et al.[34] Copyright 2019 American Chemical Society.
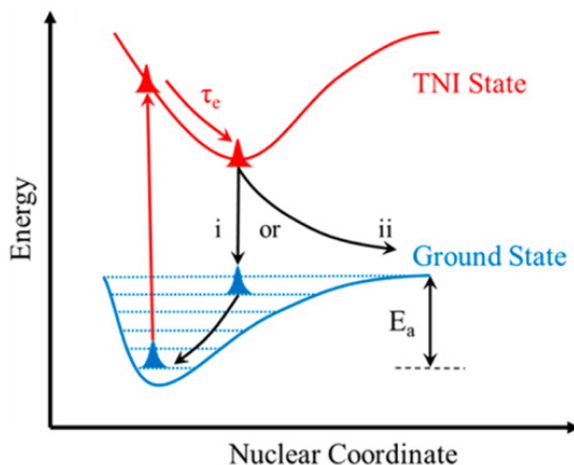
Figure 4.10: Schematic of the TNI mechanism where a brief electronic excitation into an state on an adsorbed molecule can result in the adsorbate (i) gaining vibrational energy, or (ii) overcoming an activation barrier for a chemical transformation. Reprinted with permission from Kale et al.[47] Copyright 2013 American Chemical Society.

than overcoming a reaction barrier. Another possible explanation for H_2 suppression is that the plasmonic hot electron populates a hybridized antibonding orbital in the metal-adsorbate complex. These mechanisms share the common theme of inhibition of a critical intermediate in H_2 generation.

In the case of CO_2, the interaction with a plasmonic catalyst spurs reaction while the interaction of H_2 precursors leads to a reversion to the initial state. Further studies are needed to distinguish among the proposed mechanisms, but the observation of differing interactions among adsorbates in the same catalytic system is unprecedented. Thus, plasmonic catalysis may allow the tuning of selectivity in complex reactions by promoting the surface reaction of some species and the depopulation of others.

At more cathodic potentials (-0.9 V_{RHE} and below), the differences in partial current density between light and dark conditions for H_2 and CO formation are small (Figure 4.7a). However, starting at -0.8 V_{RHE} and continuing to more cathodic potentials, the Ag catalyst produces methanol when illuminated but no detectable methanol in the dark up to -1.1 V_{RHE} (Figures 4.6b and 4.7b). The initial detection of methanol in illuminated conditions at -0.8 V_{RHE} represents a 550 mV decrease in the required overpotential to produce methanol compared to a previous report of methanol production on unilluminated polycrystalline Ag.[10] The rate of methanol production continues to increase at more cathodic potentials (Figure 4.7b), and the maximum methanol Faradaic efficiency achieved in this study is 1.4 % when the cathode is illuminated and biased at -1.1 V_{RHE} (Figure 4.6b), which is more than 130 times greater than the methanol production efficiencies reported at 250 mV higher overpotential on polycrystalline Ag in dark conditions.[10] Given that methanol is the sole product that is only produced under illumination, we compare its partial current density at various wavelengths of constant photon flux (Figure 4.11). Partial current densities for other products at the same wavelengths show no obvious trends likely due to the difficulty in deconvoluting dark and light currents. The methanol production rate at -1.1 V_{RHE} is

proportional to the absorption of the conditioned Ag cathode at the wavelength of illumination. The correlation between absorption and methanol production is a strong indication that methanol is generated via photonic effects. We present further evidence of photonic effects in later sections.
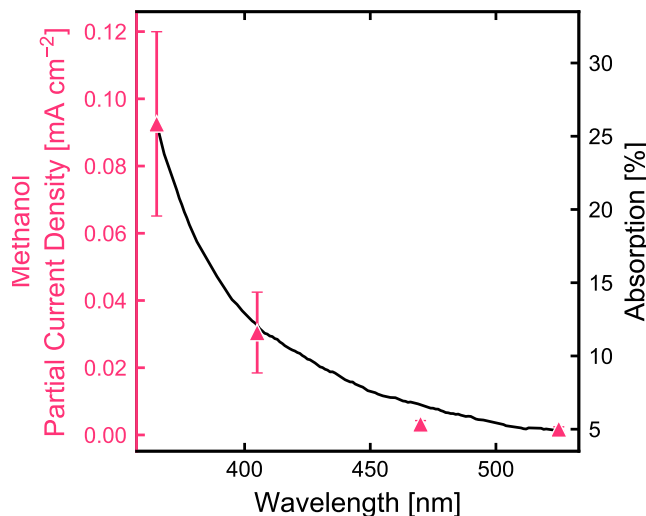
Figure 4.11: Methanol production rate under equal LED photon fluxes (3.2×10^{17} photons $cm^{-2}s^{-1}$) of different wavelengths (left ordinate) and absorption of the electrode (right ordinate) after performing CO_2 reduction at -1.1 V_{RHE} for 45 min. Absorption is calculated as $100\% - \%R$, where $\%R$ is the total reflection measured by an integrating sphere. Reprinted with permission from Creel et al.[34] Copyright 2019 American Chemical Society.

The formate production rate and Faradaic efficiency increase in the light relative to the dark from -1.1 to -0.7 V_{RHE} (Figures 4.6b and 4.7b). For example, in the potential window of -1.1 to -0.9 V_{RHE}, formate is produced under illumination at 2 to 4 times the rate of formate production at the same potential in the dark. The Faradaic efficiencies for all products reported for dark conditions here are in very good agreement with similar measurements reported by Hatsukade et al. on a polycrystalline Ag foil cathode.[10]

4.3   Photocurrent Measurements

Photocurrent magnitude measured at constant voltage with 3 Hz light modulation (Figure 4.12a) grows with the magnitude of applied cathodic potential (Figure 4.12b), in agreement with previous studies.30 The maximum photocurrent of 0.62 mA cm^{-2} at -1.1 V_{RHE} represents an internal quantum efficiency of 4% for conversion of 170 mW cm^{-2} of 365 nm light. The difference in photocurrent at -1.1 V_{RHE} reported in Figure 4.12b and the photocurrent observed in Figure 4.12a results from the difference in CO_2 flow between the two measurements, resulting in different mass transport effects; CO_2 is sparged through the cell before the measurement in Figure 4.12a but stopped during data collection to reduce signal noise whereas CO_2 is bubbled vigorously throughout in Figure 4.12b.
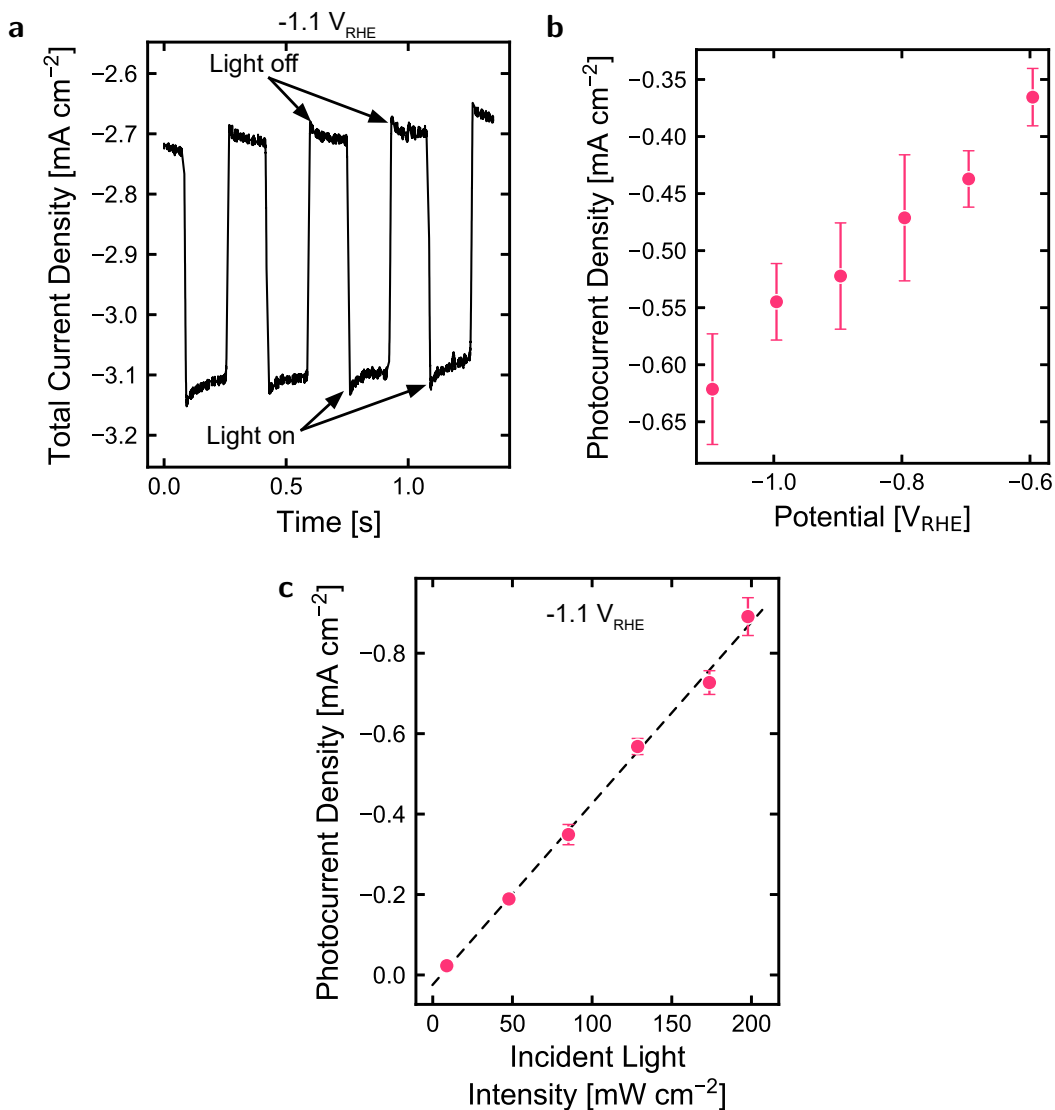
Figure 4.12: Photocurrent on Ag cathodes illuminated by a 365 nm LED. (a) Chopped-light chronoamperometry at -1.1 V_{RHE} under 170 $mW\,cm^{-2}$ incident light intensity over a Ag cathode without CO_2 bubbling to decrease the noise in the signal. (b) Photocurrent density at various potentials under 170 $mW\,cm^{-2}$ incident light intensity. (c) Photocurrent density at various light intensities incident on the Ag cathode at -1.1 V_{RHE}. The dotted line represents the least-squares regression line. Error bars in each figure represent the standard deviation of experiments performed in triplicate. Reprinted with permission from Creel et al.[34] Copyright 2019 American Chemical Society.

In the potential window of -0.8 to -0.6 V_{RHE} where CO production is plasmonically enhanced, the increase in CO partial current density at each potential (Figure 4.7a) is greater than the photocurrent density at the corresponding potential (Figure 4.12b). The decrease in HER (Figure 4.7a) at these potentials counteracts the promotion of CO, leading to a smaller than expected photocurrent. The rise in soluble product (formate and methanol) formation under illumination accounts for 14 to 41 % of the photocurrent at potentials from -1.1 to -0.9 V_{RHE}. The remainder of the photocurrent likely modifies the production of CO and H_2 slightly, although this production formation difference is not significant compared to statistical variation between trials. Notably, the difference between the total current density with and without illumination is also only statistically significant from -0.8 to -0.6 V_{RHE} (Figure 4.7c) where the photocurrent represents a relatively large proportion of the total current.

If plasmonically generated hot carriers are not extracted from the cathode, their excess energy is transferred to heating of other electrons, the lattice, and eventually the surroundings. SPR can be used to promote reactions by local heating, but the change in selectivity observed in this study cannot be explained by an increase in the local temperature at the cathode surface or heating from the LED. Our previous study showed that H_2 production is enhanced and CO production is suppressed at elevated temperatures,[31] but H_2 production rates remain the same or even decrease while CO production rates remain the same or increase with illumination in this study (Figure 4.7a). This strongly suggests that localized plasmonic heating (if it is occurring) is not the source of the observed selectivity changes. The photocurrent on the Ag cathode depends linearly on the incident 365 nm LED illumination intensities (Figure 4.12c), consistent with both an athermal mechanism for the photoactivity and the proportionality between methanol production and wavelength (Figure 4.11).[12,53] No apparent trends are observed in light-intensity-dependent product analysis (Figure 4.13). The difference between the photocurrent reported for 170 $mW\,cm^{-2}$ illumination with a 365 nm LED in Figure 4.12b and Figure 4.12c is a result of slight experimental variations. The trends shown here are repeatable across all trials.

4.4   Conclusions

In this study, we find that a simple electrochemically-conditioned polycrystalline Ag thin film exhibits strong plasmonic activity that is selective for three different CO_2 reduction products, depending on the applied potential. The same cathode simultaneously suppresses HER. These combined effects indicate that plasmonics can be used to achieve selectivity in aqueous electrochemical CO_2 reduction. The Ag nanostructures that give rise to these effects are not intentionally structured but formed electrochemically under highly cathodic conditions, meaning that the heterogeneous nanostructures are stable for hours at those conditions for product evolution. This study motivates the need for further research into several unsolved questions as the mechanism for the plasmonic selectivity is unclear. Further spectroscopic and computational research is needed to determine the role of the local electric field and the mechanism for hot electron transfer into acceptor molecules. A different nanostructure size or shape distribution to alter the SPR absorption or hot carrier generation could change the CO_2 reduction selectivity or make the plasmonic nanostructure selective for a different
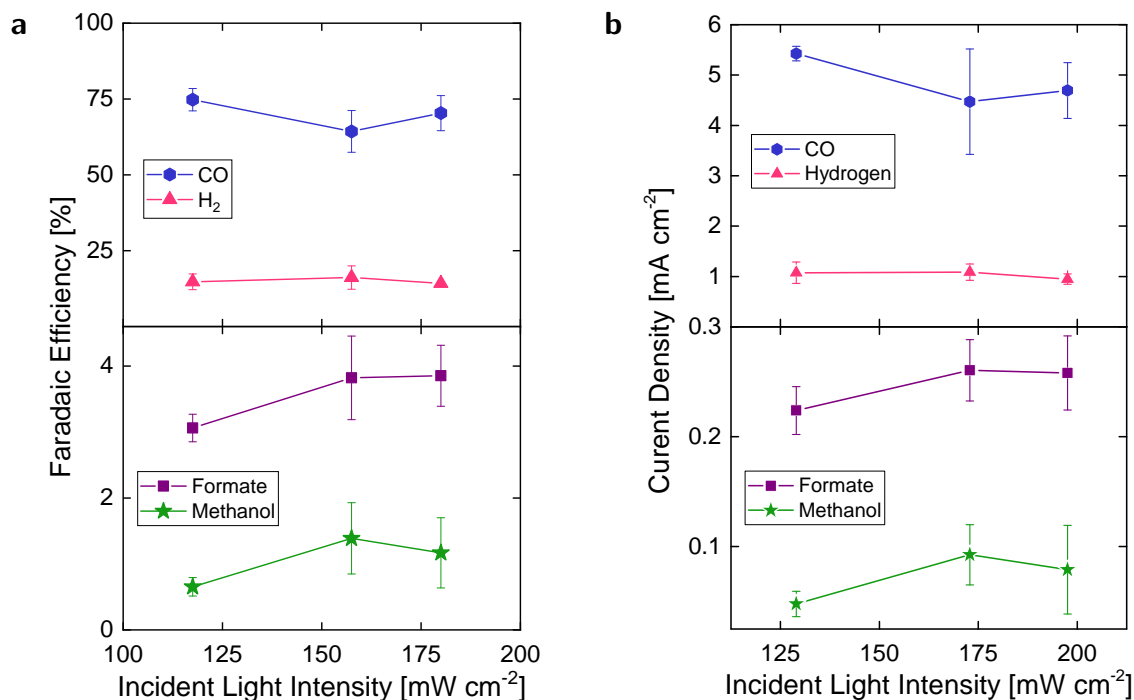
Figure 4.13: Product distribution over a Ag cathode at -1.1 V_{RHE} under 365 nm LED illumination of various incident light intensities. (a) Faradaic efficiencies. (b) Partial current densities. Error bars represent the standard deviation of experiments performed in triplicate. Reprinted with permission from Creel et al.[34] Copyright 2019 American Chemical Society.

reaction altogether. Plasmonic nanostructures likely exhibit potential-dependent activity and selectivity for other electrochemical redox reactions, but we do not know whether all reactions can be catalyzed plasmonically. We will gain further insight into these mechanisms with the development of plasmonic catalysts with improved photon-to-current efficiencies and enhanced selectivities for other complex electrochemical reactions.

4.5 Methods

4.5.1 Synthesis of Ag Cathodes

3 in. $\times$ 1 in. $\times$ 1.2 mm glass microscope slides were cleaned by sonication in acetone for 10 min followed by oxygen plasma cleaning for 4 min. The catalyst was fabricated by e-beam evaporation of 5 nm of titanium (99.999 %) as an adhesion layer on the clean glass slide and 200 nm of Ag (99.97 %) over the titanium. Ag cathodes were stored in a vacuum chamber after fabrication until use. Except where noted, all Ag cathodes were electrochemically conditioned at -1.1 V_{RHE} for 45 min in carbon-dioxide-(CO_2) saturated aqueous 1 M $KHCO_3$ before use.

4.5.2   X-ray Photoelectron Spectroscopy

x-ray photoelectron spectroscopy (XPS) spectra were collected using a Thermo Scientific
K-Alpha XPS System with a monochromated aluminum Kα source. A pass energy of 100 eV
was used for survey scans and 20 eV for high resolution scans with an energy resolution of
0.1 eV. Thin film surfaces were cleaned using an argon cluster gun (6000 eV, 150 atoms per
cluster) for 60 s before all XPS measurements. XPS spectra show the characteristic Ag $3d_{3/2}$
and $3d_{5/2}$ peaks but do not show any sign of the underlying titanium glass adhesion layer
after electrochemical conditioning.

4.5.3   Cathode Surface Imaging

SEM images were acquired using a Thermo Scientific Quanta FEG 250 SEM and a 10 kV
accelerating voltage.

AFM measurements were acquired with a Bruker Dimension Icon commercial AFM
system using the PeakForce Quantitative Nanoscale Mechanical tapping mode under ambient
conditions. For all topography measurements uncoated silicon probes (SCANASYST-AIR)
with spring constants of 0.4 N m^{-1} were used. Grain size analysis was performed using the
watershed algorithm in the Gwyddion software package. The grain location was determined
with 100 steps, a drop size of 0.10%, and a threshold of 150 nm^2. Segmentation was
determined with 20 steps and a drop size of 15.00%. No additional preparation for AFM was
performed on the as-deposited Ag cathodes, but electrodes were rinsed profusely in ultrapure
water (Millipore, 18 MΩ) and dried with a nitrogen stream after electrochemical conditioning
in preparation for AFM measurements.

4.5.4   UV-Visible Absorption Measurements

UV-visible total reflection, R, measurements of dry Ag cathodes were collected on a Shi-
madzu SolidSpec-3700 UV-visible-near-infrared (NIR) spectrophotometer equipped with an
integrating sphere after various electrolysis times in a beaker with CO_2-saturated aqueous 1
M KHCO$_3$ with a platinum wire counter electrode and a Basi MF-2052 silver/silver chloride
(Ag/AgCl) reference electrode. Spectra were referenced to a National Institute of Standards
and Technology (NIST)-calibrated mirror, and the calibration was used to find the absolute
reflection values. Absorption values reported here are $100\% - \%R$.

4.5.5   Photoelectrochemical measurements

The electrolyte used in this study was CO_2-saturated aqueous 1 M KHCO$_3$ (pH 7.75) made by
saturating 0.5 M K$_2$CO$_3$ (Alfa Aesar, 99.997% metals basis) prepared with ultrapure water
(Millipore, 18 MΩ). The electrolyte was sparged with CO_2 for 10 min prior to electrolysis
start. 85%-IR-corrected measurements were performed with a Biologic SP-300 potentiostat
in a gas-tight polyether ether ketone (PEEK) electrochemical compression cell[31] with Ace
Seal 2-015 Kalrez 6375 o-rings exposing 1 cm^2 geometric surface area of the cathode and
anode. Impedance spectroscopy from 100 to 1 kHz with 10 mV amplitude at open circuit

voltage was used to calculate the IR correction for each measurement. Typical resistances measured between the working electrode and reference electrodes in our cell fell between 5 and 10 Ω. A temperature control system comprising a Ferrotec 72008/131/150B peltier cooler mounted flush with the backside of the cathode, central processing unit (CPU) heat sink with fan, and proportional-integral-derivative (PID) controller held the catholyte at a constant (22.0 ± 0.1) °C. A Selemion AMF anion exchange membrane separated the catholyte and anolyte. CO_2 was continuously bubbled at 5 standard cubic centimeters per minute (SCCM) through a glass frit at the bottom of the cell unless otherwise noted. Platinum foil was used as the water oxidation anode, and no platinum dissolution or deposition was observed on the Ag cathode, as our product Faradaic efficiencies matched those in a previous study.[10] An Innovative Instruments, Inc., LF-1 leak-free Ag/AgCl reference electrode was used as the potential reference, but all potentials were converted to and reported versus the reversible hydrogen electrode. CVs that were performed in Ar- or CO_2-saturated 0.5 M K_2CO_3 or 0.5 M $NaClO_4$ at a sweep rate of 100 mV s^{-1}. The cathodic sweep of the 10th cycle, representative of any cycle, is plotted in Figures 4.8 and 4.9.

The cathode was illuminated from the front using a LCS-0365-48-22 Mightex Systems 365 nm ultra-high-power LED. While the output power of the LED was 2.5 W, only 170 mW reached the surface of the cathode due to the size of the cell window, absorption of the electrolyte, and scattering by the CO_2 bubbles. The light intensity incident on the cathode was determined by measuring the transmission of light through the photoelectrochemical cell with electrolyte, CO_2 bubbles, and a glass slide in place of the thin film Ag cathode then corrected for the 91.1 % transmission of 365 nm light through the glass slide. The electrolyte was saturated, but the the CO_2 bubbling was turned off for the example chopped-light chronoamperometry plot (Figure 4.12a) to minimize noise in the signal. The output light intensity for that measurement only was decreased to maintain an incident light intensity of 170 mW cm^{-2}. Wavelength-dependent measurements were performed at equal incident photon flux (3.2×10^{17} photons cm^{-2} s^{-1}) to the 365 nm LED using Mightex Systems LCS-0405-50-22, LCS-0470-50-22, and LCS-0525-60-22 LEDs at 405, 470, and 525 nm, respectively. The emission spectra of the LEDs provided by the manufacturer is included in Figure 4.14. The output and incident power were measured with a Coherent PowerMax PM10 power meter connected to a Coherent LabMax-TOP power meter console. Photocurrent was extracted from 3 Hz chopped-light chronoamperometry measurements using a Stanford Research Systems SR850 lock-in amplifier and a ThorLabs SHB1 shutter system.

4.5.6 CO_2 Reduction Product Measurements

Gaseous products of the electrochemical reactions were analyzed by an in-line SRI Instruments Multiple Gas Analyzer #5 GC equipped with a 12 ft HayeSep D (divinylbenzene) column, thermal conductivity detector (TCD), flame ionization detector (FID) with methanizer, and argon carrier gas. The detection limit of the GC is 1 ppm. For a single product analysis run, a constant potential was applied for 64 min with GC injections at 3, 15, 27, 39, 51, and 63 min Gas in the headspace and gas line to the GC does not eqilibrate by the three-min injection, so the average concentration from only the last five cycles was used in calculations of product generation. The concentration of the gas in each injection was computed from
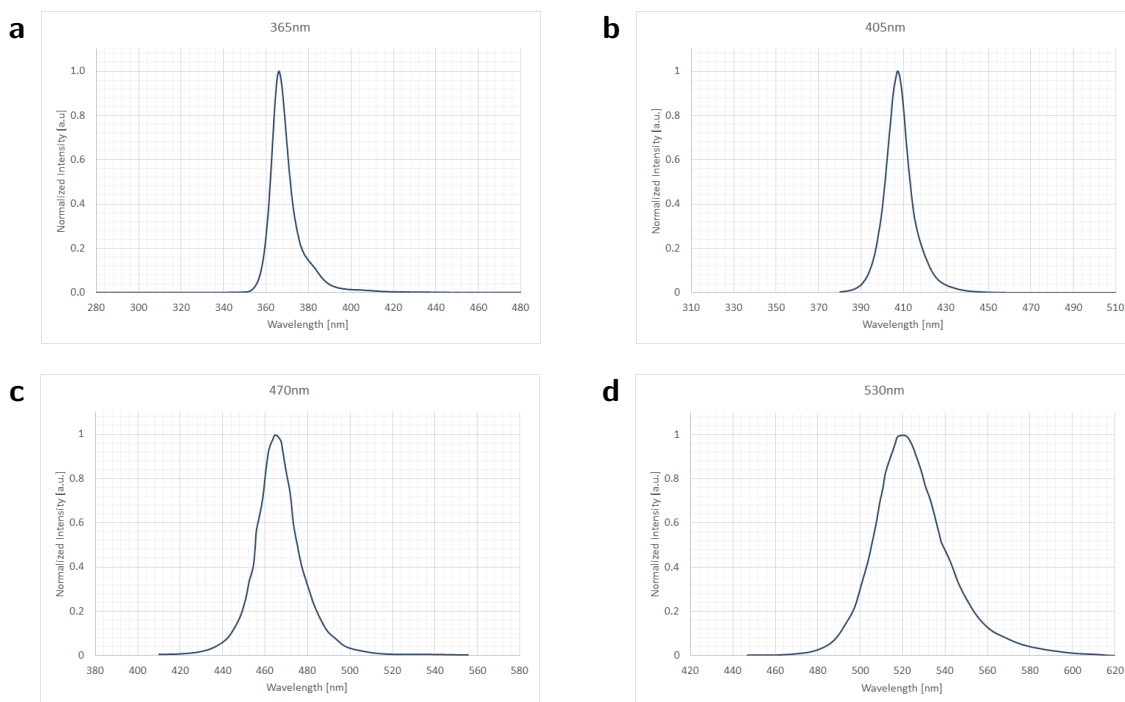
Figure 4.14: Emission spectra of the ultra-high-power Mightex Systems LEDs used in this study provided by the manufacturer. (a) 365 nm LED (LCS-0365-48)-22, (b) 405 nm LED (LCS-0405-50-22), (c) 470 nm LED (LCS-0470-50-22), and (d) 525 nm LED (LCS-0525-60-22)

calibration curves with at least three points for each gas type. The partial current density, I_x, for each gaseous product, x, in each GC injection is given by

$$I_x = \frac{\mathrm{F}c_x n f}{ma} \tag{4.1}$$

where c_x is the concentration of product x as a molecular fraction of the total injected gas, n is the number of electrons needed to produce product x (2 mol of electrons per mol of H$_2$ or CO), f is the flow rate of CO$_2$ into the electrochemical cell (5 cm^3 min^{-1} or 8.333×10^{-5} L s^{-1} in this study), m is the the molar volume of CO$_2$ at 21.0 °C (24.01 L mol^{-1} from the NIST WebBook), and a is the geometric surface area of the cathode (1 cm^2 in this study). We assume that the evolved gases have the similar molar volumes as CO$_2$. The Faradaic efficiency of a product is given by

$$\mathrm{FE} = \frac{I_x}{I} \tag{4.2}$$

where I is the average total current density measured by the potentiostat over the five min before the GC injection. The average values for current density and Faradaic efficiency over the last five injections are reported here. Liquid products in the catholyte and anolyte were quantified after the electrolysis was complete by ^{1}H NMR spectroscopy on a Bruker Avance III 500 MHz magnet using phenol and dimethyl sulfoxide (DMSO) as internal standards and a water suppression method with 60 s between pulses to allow for complete proton relaxation.[31]

The area of the DMSO singlet peak at 2.6 ppm relative to tetramethylsilane (TMS) was used to determine the methanol concentration in the sample using the methanol singlet at 3.23 ppm relative to TMS. The detection limit of the ^{1}H NMR is 1 ppb.

4.5.7 Electrochemical Surface Area Measurements

ECSA of electrochemically conditioned electrodes was determined relative to the as-e-beam-evaporated electrode by taking the ratio of their double layer capacitances as measured by the cyclic linear potential sweep method.[54] First, the Faradaic current due to double layer charging in CVs was measured at a series of increasingly rapid scan rates (Figure 4.3a). A Savitzky-Golay filter was used to smooth the CV data in Figure 4.3a, but the raw data was used in the determination of the charging current. The charging current was taken as half of the difference between the average current between 0.544 and 0.549 V_{RHE} in the anodic direction and the average current between 0.509 and 0.514 V_{RHE} in the cathodic direction on the third CV cycle. The capacitance is the y-intercept of the best-fit line of the charging current versus scan rate (Figure 4.3b). The capacitance was measured for the same electrode after various electrolysis times. Each measured capacitance was normalized to the capacitance of the as-deposited electrode for the relative ECSA (Figure 4.3c).

Chapter 5

Well-Defined Nanostructured Electrodes

5.1 Colloidal Nanoparticle Electrodes

As discussed in Section 1.2.3, the surface plasmon resonance (SPR) energy and properties of a plasmonic nanostructure are broadly tunable with the size and shape of the nanostructure. These properties alter the catalytic ability of the plasmonic nanostructure. The efficiency of hot electron generation impacts the availability of hot electrons, the energy of hot electrons affects their reducing potential, and the intensity of local electric fields manipulates the local environment at the plasmonic active sites; all vary with plasmonic properties. Thus, a narrow size and shape distribution of the plasmonic catalyst may increase plasmonic catalytic activity, decrease required overpotentials, or even increase selectivity for a particular reaction. In fact, a study of photochemistry (PC) water reduction over Au-TiO$_2$ heterostructures demonstrated that the gold nanoparticle size and the illumination wavelength have a dramatic effect on activity. Under broadband illumination that excites both the gold SPR and the TiO$_2$ band gap, a photocatalyst with 4.4 nm Au nanoparticles produced H$_2$ at 20 times rate per gram of catalyst than heterostructures with 67 nm Au nanoparticles. Conversely, under illumination that only activates the gold SPR, the photocatalyst with 4.4 nm Au nanoparticles was inactive for H$_2$ evolution while the photocatalyst with 67 nm Au nanoparticles still produced a significant amount of H$_2$. The 4.4 nm Au nanoparticles are too small to have a strong SPR but have a more synergistic effect with the TiO$_2$ than the larger nanoparticles.[55]

It is possible to achieve fine control over the shape, size, and composition of nanoparticles through solution-based colloidal synthesis methods because of the separation of particle nucleation and growth phases in time. Colloidal synthesis generates inorganic nanoparticles that are suspended in a solution with solubility conferred by organic ligands that passivate the surface sites of the nanoparticle.

5.1.1 Colloidal Nanoparticle Synthesis

Colloidal synthesis is usually performed with a metal salt precursor, reducing agent, and ligand stabilizers under inert atmosphere at high temperatures using a Schlenk line (Figure 5.1).
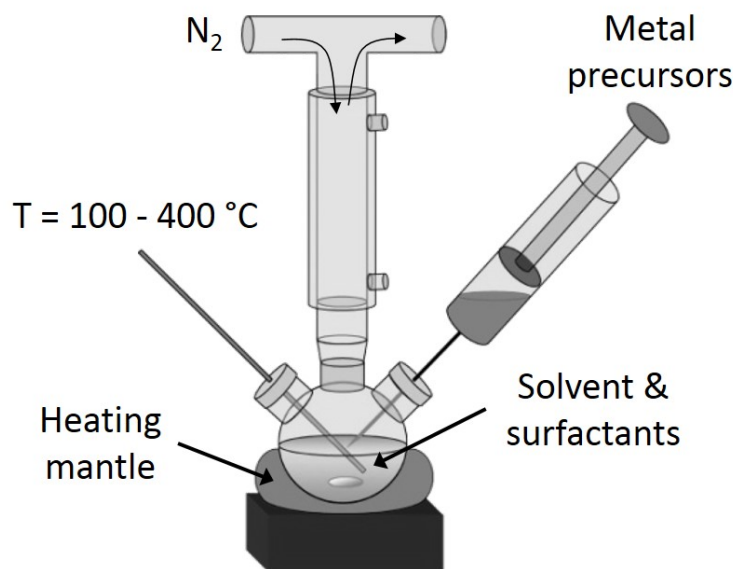
Figure 5.1: Illustration of the hot injection method for colloidal synthesis. Generally, solvents and surfactants are heated to 100 to 400 °C with a heating mantle under an inert atmosphere such as N_2 fed through a Schlenk line. Metal precursors are rapidly injected into the hot solution for a brief nucleation phase followed by growth of nanoparticles.

During a synthesis, the metal salt precursors are reduced to metal atoms (monomers) by a combination of the reducing agent and high temperature. The monomers aggregate to form nuclei that grow by further addition of monomer (Figure 5.2).
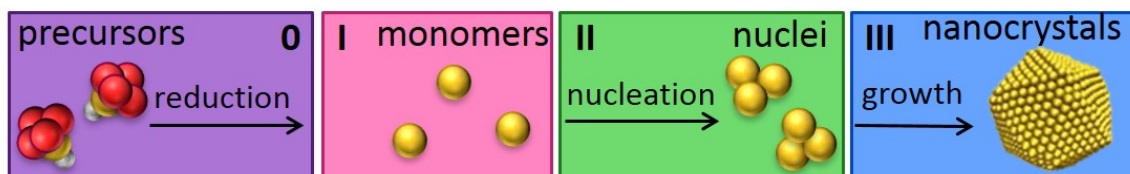
Figure 5.2: Overview of colloidal nanoparticle synthesis in which metal salt precursors are reduced to form metal monomers followed by nucleation and growth. In box 0, precursor molecules, which are commonly metal salts or inorganic compounds, are reduced so that the metal atoms are in the appropriate oxidation state for the eventual nanoparticle. For a metal nanoparticle, the oxidation state is zero. Box I shows the product of precursor reduction, monomers. Monomers are the atomic units that comprise the eventual nanoparticles. In box II, monomers nucleate to form nuclei. In box III, stable nuclei grow to form mature nanocrystals.

The classical theory of nucleation and growth is represented by the LaMer diagram (Figure 5.3). In phase I, monomers accumulate as the metal salts are reduced to metal atoms. Once the monomers reach the critical concentration for nucleation, C_n, they begin to form nuclei in phase II. Nucleation is favorable when the free energy of nucleation ΔG_{nuc} is negative.
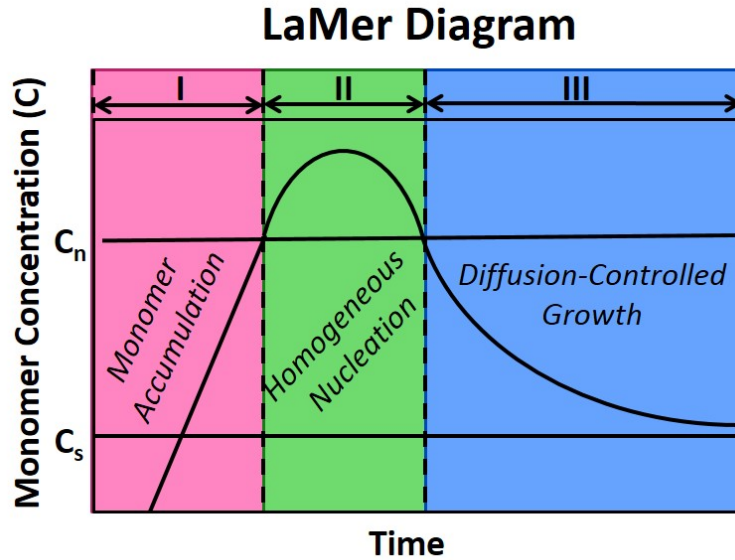
LaMer Diagram

Figure 5.3: The LaMer diagram illustrates the three time-isolated phases in colloidal nanoparticle synthesis: monomer accumulation, nucleation, and growth.

$$\begin{aligned}
\Delta \mathrm{G_{nuc}} &= \Delta \mu_v + \Delta \mu_s \\
&= \frac{4}{3}\pi r^3 \Delta \mathrm{G}_v + 4\pi r^2 \gamma \\
&= \frac{4}{3}\pi r^3 \left(\frac{k_B T}{\Omega}\right) \ln\left(\frac{C}{C_s}\right) + 4\pi r^2 \gamma
\end{aligned} \tag{5.1}$$

where $\Delta \mu_v$ is the free energy change for a spherical nucleus with radius r, $\Delta \mu_s$ is the change in surface energy for a spherical nucleus, $\Delta \mathrm{G}_v$ is the change in free energy per unit volume of the solid phase, γ is the surface energy per unit area, Ω is the atomic volume, C is the concentration of the monomer, and C_s is the solubility of the monomer. From a plot of $\Delta \mathrm{G_{nuc}}$ versus particle radius (Figure 5.4), it is clear that a nucleus is stable only when its radius exceeds a critical size $r*$.[56]

$$r* = \frac{2\gamma\Omega}{k_B T \ln\frac{C}{C_s}} \tag{5.2}$$

During phase II, the monomer concentration continues to rise for a brief time as reduction is still occurring but falls rapidly as burst nucleation outpaces precursor reduction. When the monomer concentration falls below the nucleation threshold, no more nuclei can form, but the nuclei formed in phase II can grow to become nanoparticles. The monomer concentration must remain above the solubility threshold to prevent the nanoparticles from dissolving.

Nanoparticle growth can be achieved in two different domains—size sharpening and Ostwald ripening. In the size sharpening regime, the monomer concentration remains high during the phase III growth. Small nanoparticles have a larger free energy because of their high surface atom to bulk atom ratio, so they grow faster and preferentially over the larger
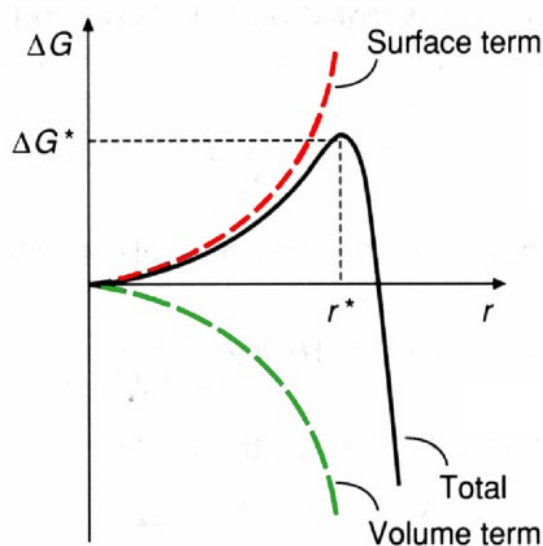
Figure 5.4: Free energy of nucleation versus particle radius showing the critical radius threshold for stable nuclei. Reproduced with permission from Cao and Wang[56]. Copyright 2004 by World Scientific.

particles. Monodispersity (uniformity in size) is achieved by this difference in growth rate because the smaller particles grow rapidly to the size of the larger particles. Conversely, in the Ostwald ripening regime, the monomers have been depleted so the smaller particles cannot grow to reach the size of the larger ones. In fact, the smallest nanoparticles are unstable enough that they dissolve. This reintroduces new monomer into the solution but does not raise the monomer concentration above the nucleation threshold, so the remaining largest nanoparticles grow. Syntheses utilizing Ostwald ripening typically require a longer reaction time and produce larger particles than syntheses achieving monodispersity through the size sharpening method.

There are a few general synthetic strategies used to achieve larger nanoparticles. 1) Increasing the ligand concentration may stabilize the precursor so that monomer production continues into the growth phase for a greater supply of monomers during growth and smaller number of nuclei formed. 2) A lower reaction temperature can lead to larger nanoparticles by reducing the number of nuclei formed since the activation energy for nucleation is greater than that for growth. 3) Using a more stable precursor allows for the formation of larger nanoparticles by a similar mechanism as increasing ligand concentration. 4) Decreasing the amount of precursor used effectively increases ligand concentration to achieve larger nanoparticles. These strategies can be reversed to achieve smaller nanoparticles.[57]

We use these general principles for colloidal nanoparticle synthesis to make various plasmonic nanoparticles for carbon dioxide reduction (CO_2R).

Synthesis of 15 nm Gold Nanospheres

Gold seeds were synthesized by mixing 15 mL of 0.1 M cetyltrimethylammonium bromide (CTAB) and 0.5 mL of of 0.01 M gold (III) chloride ($HAuCl_4$, Alfa Aesar). 1.2 mL of chilled
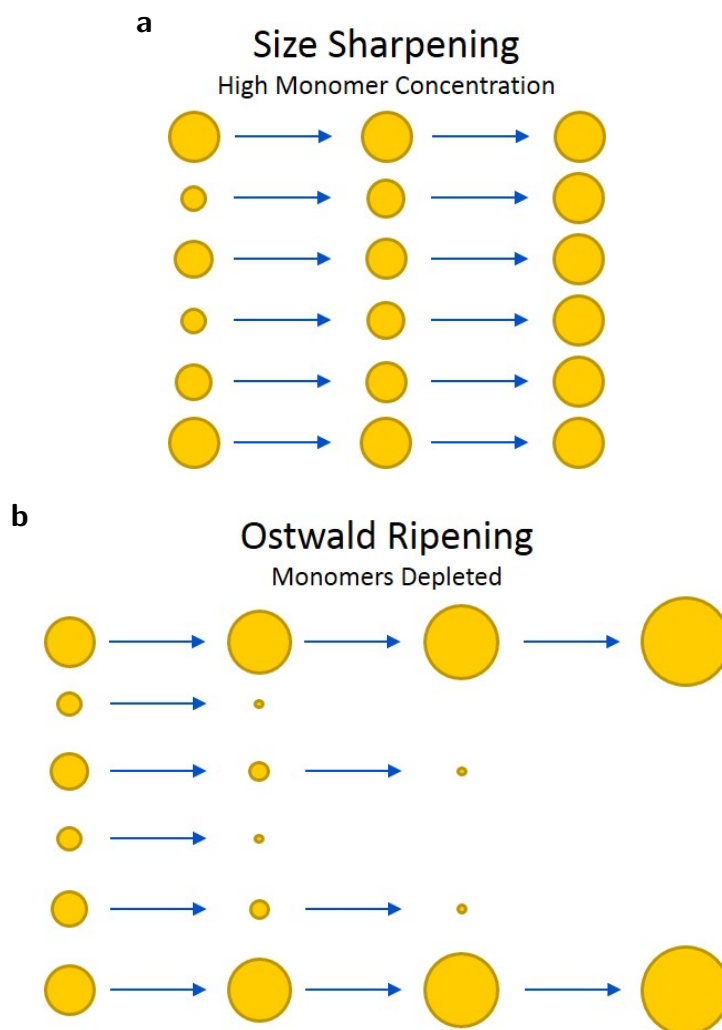
Figure 5.5: Schematic representations of nanoparticle growth regimes. (a) In size sharpening, smaller nanoparticles grow faster. (b) In Ostwald ripening, smaller nanoparticles dissolve and their constituents are incorporated into larger nanoparticles.

0.01 M sodium borohydride ($NaBH_4$) was added to the solution, and the entire solution was inverted rapidly for 30 s. The seed synthesis was complete after the solution rested at room temperature for 1 h.

"15 nm Au spheres" were grown from the gold seeds in a method based on Fang et al.[58] First, 0.8 mL of 0.01 M gold (III) chloride was diluted in ultrapure water to 32 mL of ultrapure water. 6.4 mL of 0.1 M CTAB, 3.8 mL of 0.1 M L-(+)-ascorbic acid, and 40 µL of the gold seed solution were added to the gold salt solution with 10 s of stirring. The growth was complete after the solution sat undisturbed overnight. Transmission electron microscope (TEM) shows aggregated 15 nm gold spheres with a few long rods (Figure 5.6a). All TEM images were collected on a Jeol JEM-2100F 200 kV Field-Emission TEM.
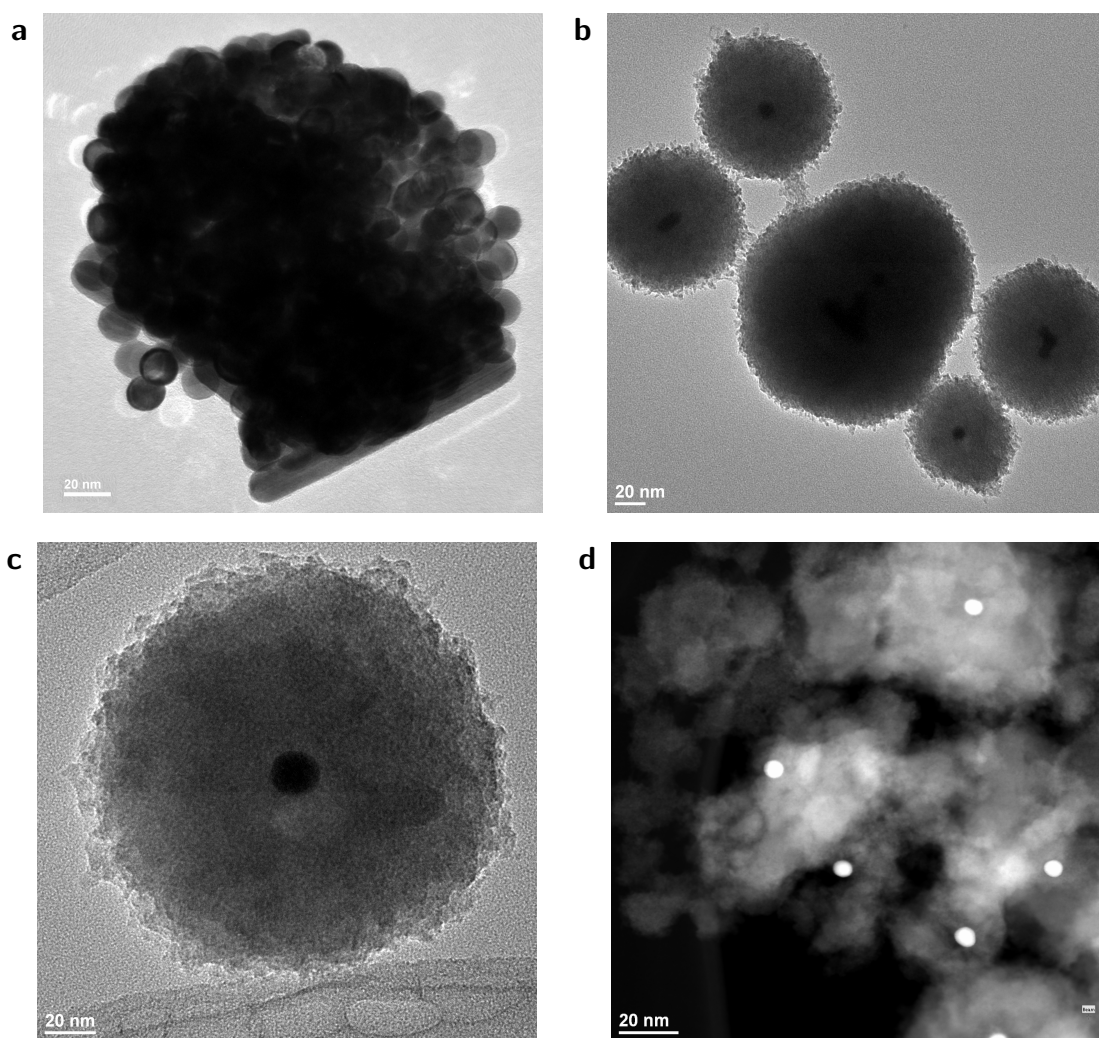
Figure 5.6: TEM images of colloidal (gold core)/(titania shell) nanoparticles. (a) 15 nm Au nanosphere cores, (b) (Gold core)/(titania shell) nanoparticles, and (c) a single (gold core)/(titania shell) nanoparticle, and (d) dark field image of (gold core)/(titania shell) nanoparticles. The gold particles appears as dark circles in a-c and as white circles in d.

Synthesis of (Gold Core)/(Titania Shell) Nanoparticles

(Gold core)/(titania shell) nanoparticles were synthesized by growing titania shells around gold seeds based on the procedure outlined in Fang et al.[58] The the tiania shell was selected to protect the gold nanoparticles from sintering during annealing or electrochemistry. Additionally, the Schottky barrier typically formed at the interface between gold and titania may increase the lifetime of excited charge carriers. The plasmonic hot electrons from the gold may be injected into the titania conduction band and be unable to return to the gold due to the barrier (Figure 5.7).

The titania shell was made by first adding 0.17 g of titanium (III) chloride ($TiCl_3$) to degassed 0.1833 mL of hydrochloric acid (HCl) and 600 µL of water. 200 µL of this solution
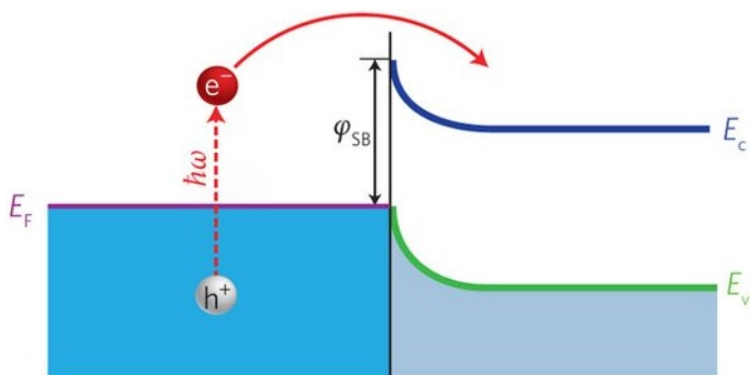
Figure 5.7: Diagram of the Schottky metal-semiconductor interface formed between Au and TiO_2. Plasmonic hot electrons generated above E_F are injected over the Schottky barrier into the conduction band of the TiO_2. E_C is the conduction band minimum of TiO_2, and E_V is the valence band maximum. Filled states in the metal are shaded blue. Filled states in the semiconductor are shaded gray. Reprinted with permission from Clavero[23] Copyright 2014 Nature.

was added to thoroughly degassed 6 mL of water, making a purple solution. 3.8 mL of degassed 0.93 M sodium bicarbonate ($NaHCO_3$) was added drop-wise to the $TiCl_3$ solution, forming a gray solution. 10 mL of 15 nm Au nanospheres was centrifuged at 8,000 rpm for 7 min then redispersed in 5 mL water. Ligand exchange was carried out by adding the centrifuged Au nanoparticles to a solution of 0.02 g of polystyrene sulfonate (PSS) in 5 mL of water drop-wise with rapid stirring. The ligand exchange process occurred as the solution sat undisturbed for 4 h. Then, the Au nanoparticle solution was centrifuged at 11,000 rpm for 7 min and redispersed in 200 µL of water. The Au nanoparticle solution was added to the $TiCl_3$ solution immediately after the addition of $NaHCO_3$, forming a grayish purple solution. After 15 min of reaction time, the combined solution was centrifuged twice at 11,000 rpm for 7 min, redispersing each time in 2.5 mL of water. TEM shows polydisperse particles with gold cores and thick, polycrystalline titania shells (Figure 5.6b).

In an effort to reduce the titania shell thickness, the same titania shell growth procedure was repeated except with half the amount of $TiCl_3$ and a reaction time of 1 min. TEM shows that the titania shells were no less thick and many Au nanoparticles did not have a complete titania shell (Figures 5.6c and 5.6d).

Synthesis of 10 nm Gold Nanospheres

Synthesis of 10 nm Au nanospheres was adapted from Shen et al.[59] 0.3246 g of gold (III) chloride (Alfa Aesar, 64.4 %), 5.351 mL of oleylamine, 53.51 mL toluene, and 100 µL of oleic acid were combined in a 3-neck roundbottom flask open to air. Nitrogen was blown into the flask while stirring for 30 minutes. The flask was capped under nitrogen atmosphere and continued to stir while the solution was heated to 65 °C. The solution was kept stirring at 65 °C for 22 h. The solution turned from red to orange to yellow to burgundy during this time.

The nanoparticles were washed with reagent alcohol and centrifugred at 6,000 rpm for 5

min. The pellet was easily resuspended in 15 mL toluene. The solution was washed with 15 mL reagent alcohol, centrifuged, and pellet resuspended in toluene twice. For size selection, a small amount of reagent alcohol was added until the solution started to become cloudy due to the largest nanoparticles precipitating. This solution was centrifuged again, and most of the nanoparticles precipitated. The supernatant with small nanoparticles was discarded, and the pellet was resuspended in hexane. The larger nanoparticles in the pellet are 9 to 10 nm in diameter by TEM imaging (Figure 5.8) and have a well-defined plasmon absorption peak in solution at 525 nm (Figure 5.9).
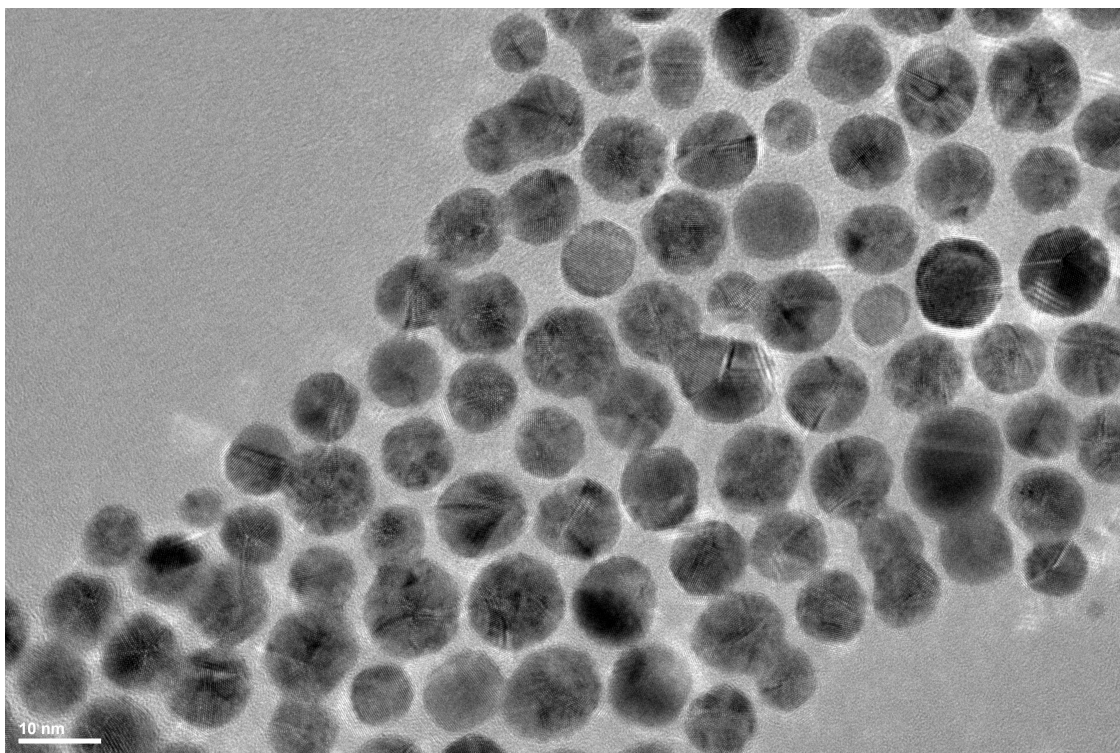
Figure 5.8: TEM image of colloidal 10 nm Au nanospheres.

Synthesis of Ag Nanocubes

Ag nanocubes of approximately 40 nm on a side were synthesized according to the procedure outlined in Zhang et al.[60] First, 60 mL of ethylene glycol was heated to 150 °C with 300 rpm stirring. After 50 min of heating, argon flow into the sealed flask, across the surface of the liquid, and out through a water bubbler at 10 psi was started. After 10 min, 0.7 mL of 3 mM sodium hydrosulfide (NaHS hydrate, Sigma) in ethylene glycol was injected quickly into the hot ethylene glycol followed shortly by a rapid injection of 15 mL of 20 $mg\,mL^{-1}$ of polyvinylpyrrolidone (PVP, Aldrich 55,000 molecular weight). 8 min later, 5 mL of 48 $mg\,mL^{-1}$ silver nitrate ($AgNO_3$, Sigma, > 99.0 %) in ethylene glycol was injected into the hot solution. The solution turned orange immediately and was stirred for 20 min while maintaining the elevated temperature. After 8 min, the solution turned greenish-brown, indicating formation of the Ag nanocubes. The reaction was quenched in an ice bath and
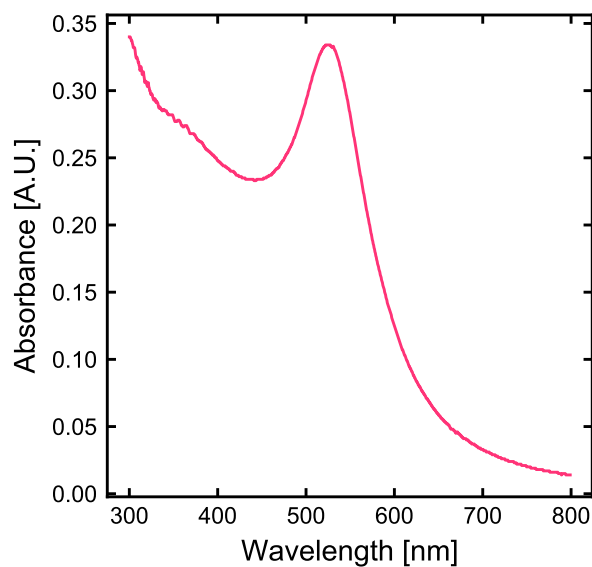
Figure 5.9: Ultraviolet (UV)-visible absorbance spectra of colloidal 10 nm Au nanospheres in hexane as measured in a 1 cm path length cuvette.

washed with acetone and water, centrifugation at 10,000 rpm for 8 min, and pellet redispersal via sonication in water.

Synthesis of 3 and 5 nm Ag Nanospheres

Ag nanoparticles were synthesized as described in Peng et al.[61] Briefly, 40 mL of oleylamine, 0.1 mL oleic acid, and 0.34 g $AgNO_3$ (Sigma, 99.0 %) were combined in a 250 mL round bottom flask. The solution was heated to 60 °C while cycling the headspace between vacuum and nitrogen three times. The solution was degassed under vacuum at 60 °C for 30 minutes. After switching to a nitrogen atmosphere, the temperature of the flask was increased to 180 °C over 30 minutes. During this heating, the solution changed from light yellow and clear to light orange and clear to dark brown. The solution was stirred at 180 °C for one hour. The flask was cooled by removing from heat.

Washing and size selection was performed by separating the solution into two centrifuge tubes and adding 20 mL of acetone to each. The tubes were centrifuged at 8,500 rpm for 8 min. Larger nanoparticles were precipitated by the acetone, and smaller nanoparticles remain dissolved in the supernatant. The pellet was redispersed in hexanes, and TEM on a Jeol JEM-2100F shows that the particles are highly monodisperse spheres of $5 - 6$ nm in diameter (Figure 5.10a). These nanoparticles will be referred to as "5 nm Ag spheres." The Ag spheres have a strong plasmon absorption peak at 424 nm (Figure 5.11). The supernatant was washed twice more with additional acetone and centrifuged. The pellet from the second centrifugation was redispersed in hexanes, and TEM shows that the particles are 1.5 to 4 nm spheres that readily self-assemble (Figure 5.10b). The smaller particles will be referred to as "3 nm Ag spheres."
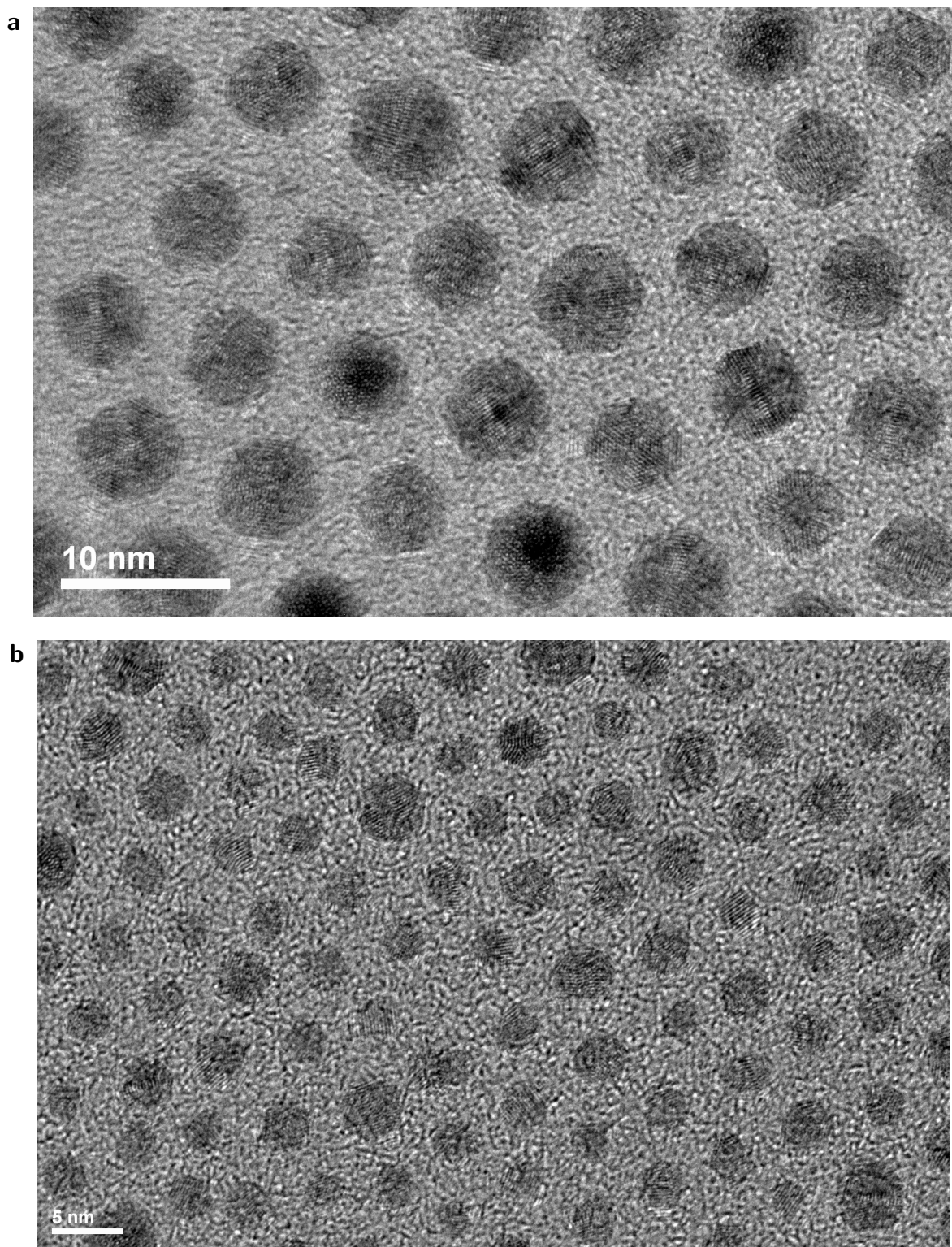
Figure 5.10: TEM images of colloidal Ag nanospheres. (a) 5 nm Ag nanospheres and (b) 3 nm Ag nanospheres made in the same synthesis but separated by centrifuge size separation.
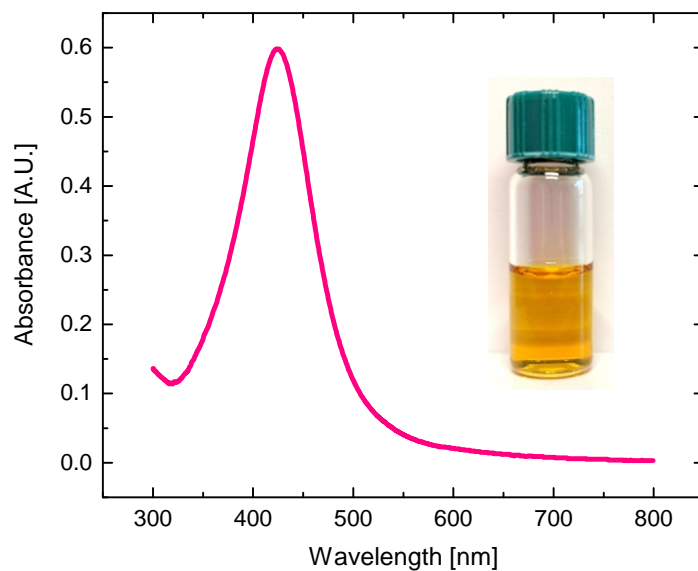
Figure 5.11: UV-visible absorbance spectra of colloidal 5 nm Ag nanospheres diluted 1 : 900 v:v in hexane as measured in a 1 cm path length cuvette. Inset is a photo of 5 nm Ag nanosphere solution in a cuvette.

Synthesis of Hydrophilic 5 nm Ag Nanospheres

Hydrophilic 5 nm Ag nanoparticles were synthesized as described in Agnihotri et al.[62] 50 mL of an aqueous solution of 2 mM sodium borohydride (NaBH$_4$) and 4.28 mM sodium citrate was made by mixing 71.2 mg of NaBH$_4$ (Aldrich, $\geq$98.0 %) and 60.1 mg of sodium citrate (J. T. Baker, ultrapure bioreagent) in 50 mL of ultrapure water. This solution was heated at 60 °C in a flask open to air for 30 min. 2 mL of 1 mM AgNO$_3$ (Aldrich) was added dropwise to the hot solution over 2 min. The temperature of the solution was increased to 90 °C, and the pH was increased from 10.0 to 10.5 using 0.1 M sodium hydroxide (NaOH, Amresco ACS grade). The solution was stirred at 90 °C for 20 min.

The nanoparticles were washed by centrifuging the solution at 11,000 rpm for 5 min. The supernatant was pipetted off as the pellet was not compacted. The precipitate was redispersed in 2 to 4 mL of ultrapure water. This washing procedure was repeated twice more, and the nanoparticles were finally redispersed in 2 mL of ultrapure water.

5.1.2   Drop-Cast Electrodes

Drop-casting is a simple method in which a solution containing a dispersed solid is dropped onto a surface and allowed to dry, forming a thin film of the solid. While this method requires no special tools or time-intensive procedures, it also usually produces a non-uniform film. Here, drop-casting is used to deposit colloidal nanoparticle solutions onto conductive electrode surfaces as a quick method for screening nanoparticle (photo)electrochemical activity.

Drop-Cast 15 nm Gold Nanospheres on Carbon Paper

400 µL of 15 nm Au nanospheres were drop-cast onto a P75 carbon paper electrode and allowed to dry for 7 hours. Carbon paper is hydrophobic, so the aqueous solution pooled rather than spread over the electrode. Nanospheres and nanorods were visible on the electrode after drying in scanning electron microscopy (SEM) images (Figure 5.12). However, there is no change in the optical properties of the carbon paper after nanoparticle deposition. Likely, the black carbon paper already absorbs near 100 % at the plasmon resonance of the nanoparticles, so there is no increase in absorption.
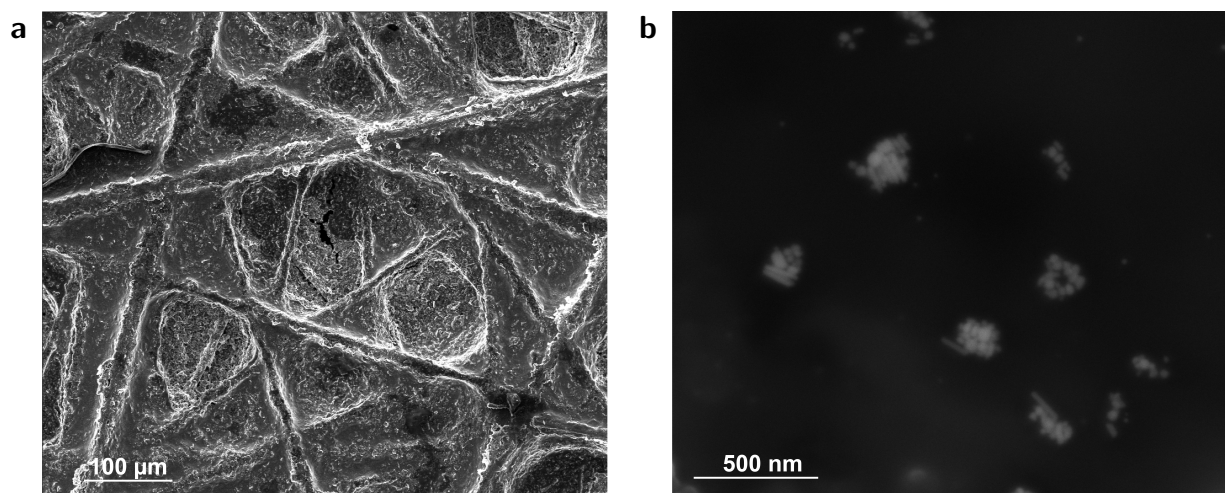
Figure 5.12: SEM images of colloidal 15 nm Au nanospheres on P75 carbon paper.
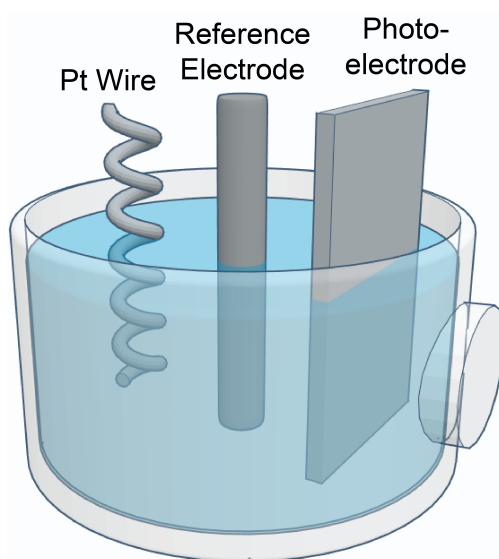
Figure 5.13: Drawing of a beaker electrochemical cell with quartz window in the three-electrode configuration.
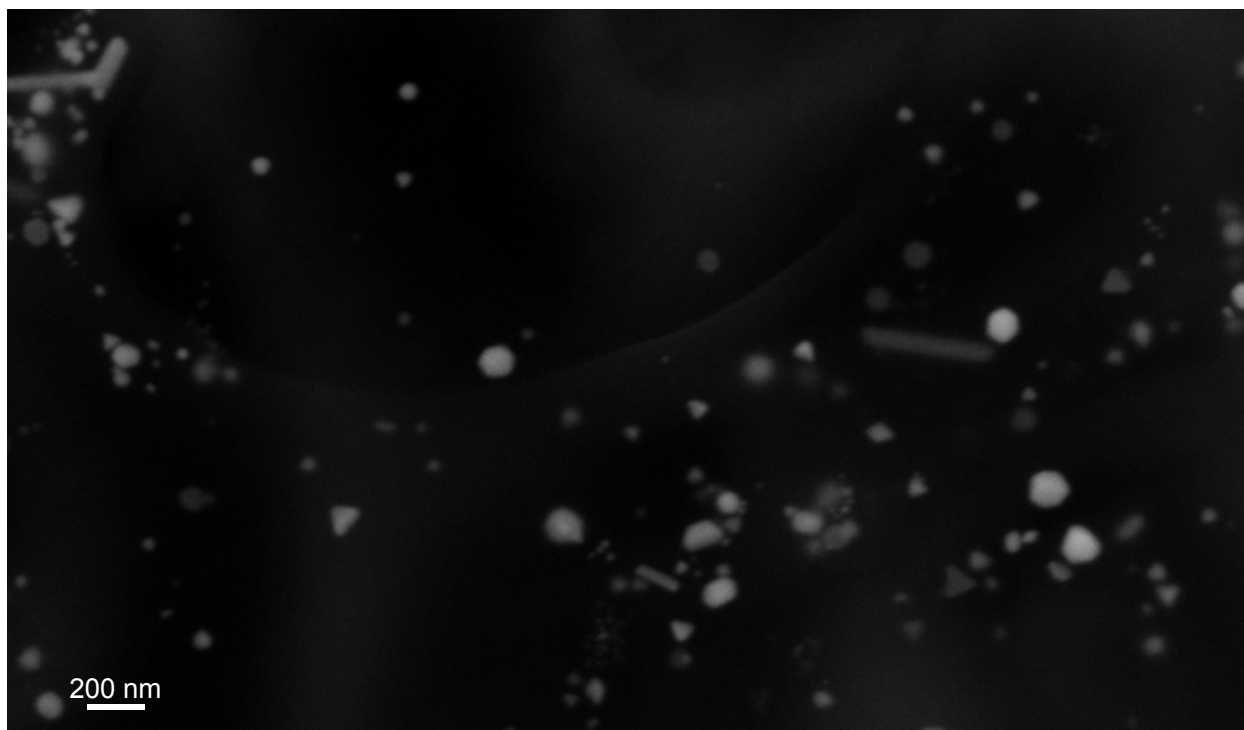
Figure 5.14: SEM image of colloidal 15 nm Au nanospheres on P75 carbon paper after annealing at $180\,°C$ for 14 h in air.

The bare carbon paper electrode and the carbon paper electrode with 15 nm Au nanospheres showed little to no photocurrent under 30 s chopped-light solar simulator illumination in 0.05 M K_2CO_3 saturated with CO_2 in chronoamperometry (CA) measurements from open circuit voltage (OCV) to -1.2 Volts versus the reversible hydrogen electrode (V_{RHE}) in a beaker electrochemical cell with a quartz window (Figure 5.13). It is possible that the light flux was too low to observe significant photocurrent without a lock-in amplifier.

When a drop-cast 15 nm Au nanospheres on P75 carbon paper electrode was annealed at $180\,°C$ for 14 hours in air, the particles showed obvious signed of sintering. The particles were, on average, larger and more varied in shape including many triangles (Figure 5.14).

Drop-Cast (Gold Core)/(Titania Shell) Nanoparticles on Silicon Wafers

Both sets of (gold core)/(titania shell) nanoparticles were deposited onto a silicon wafer that had been sonicated in isopropanol. For the first set of core-shell nanoparticles, 1 mL of nanoparticle solution was centrifuged at 8,000 rpm for 5 min, half the supernatant was removed, 3 mL of ethanol was added, and the solution was centrifuged again. The pellet was redispersed in 0.5 mL of ethanol, and 5 drops of that solution were drop-cast onto a silicon wafer that was immediately covered by a vial cap to slow solution evaporation and decrease the coffee ring effect. For the second set of core-shell nanoparticles, 3 drops of the prepared nanoparticle solution were drop-cast onto a silicon wafer. Both wafers were annealed in air at $450\,°C$ for 2 h to remove organic ligands.

Electrodes were prepared by connecting copper wire to the back of the silicon electrodes

with Circuit Works CW2400 conductive Ag epoxy. The conductive epoxy and exposed copper wire was coated in Loctite 9460 Hysol epoxy to insulate them from the electrolyte.

Neither electrode showed any photoactivity in alternating illuminated and unilluminated 0.1 M KHCO$_3$ cyclic voltammetry (CV)s under solar simulator illumination. It is possible that the light flux was too low to observe significant photocurrent without a lock-in amplifier.

Drop-Cast 10 nm Gold Nanospheres on Various Substrates

Electrodes were made by drop-casting 100 µL of the 10 nm Au nanospheres onto three substrates that were rinsed in hexane prior to drop-casting. Two additional aliquots of 100 µL of the 10 nm Au nanospheres after allowing the solvent to evaporate slowly (while the substrate was covered with an inverted Petri dish).

A glass slide with electron beam (e-beam)-deposited 70 nm of TiO$_2$ on top of 30 nm of Ag on top of 3 nm of Ti shows negligible photocurrent under 300 to 500 mW cm^{-2} solar simulator illumination in CO$_2$-saturated 0.05 M K$_2$CO$_3$ in a beaker cell with quartz window (Figure 5.13). However, the same electrode substrate with 10 nm Au nanospheres drop cast on top exhibits a noticeable photoresponse. However, due to adhesion issues of both the e-beam-deposited film and the nanoparticles, this approach was not pursued further.

Drop-Cast Ag Nanocubes

300 µL of Ag nanocube solution was drop-cast onto P75 carbon paper and onto a glass slide with e-beam-deposited 30 nm of Ag on top of a 3 nm titanium adhesion layer. Both substrates were rinsed with water before depositing nanoparticles. In chopped-light CA measurements in CO$_2$-saturated 0.05 M K$_2$CO$_3$ with 300 mW cm^{-2} light intensity from a solar simulator, the Ag nanocubes on the TiO$_2$/Ag thin film show 200 µA of photocurrent at -1.1 V$_{RHE}$. The TiO$_2$ layer seems to be important for achieving photoactivity because Ag nanocubes deposited on the same type of electrode but without the TiO$_2$ layer exhibits little to no photoactivity in the same conditions. The TiO$_2$ conduction band may serve as an electron collector, lengthening the lifetime of the plasmonic hot electrons. Alternatively, the TiO$_2$ may stabilize the colloidal nanoparticles and prevent aggregation or delamination. After performing electrochemistry on many different Ag thin film electrodes with various drop-cast nanoparticles on top, the nanoparticles would be found floating on the electrolyte surface in the beaker. Thus, nanoparticle adhesion to electrode surfaces needed to be improved.

The Ag nanocubes on carbon paper produced 2 mA of photocurrent, but the carbon substrate itself produced 1 mA of photocurrent in the same conditions (Figure 5.15). While the photocurrent over the carbon paper photocathode increased with addition of Ag nanocubes, the ideal electrode substrate is conductive but does not contribute to photoactivity. In order to carefully explore the role of plasmonics in electrochemical CO$_2$R, the plasmonic catalyst should be the only light absorber in the system so that all photoactivity can be attributed to the plasmonic effect, not the supporting absorber. Thus, carbon paper was rejected as a photocathode conductive support.
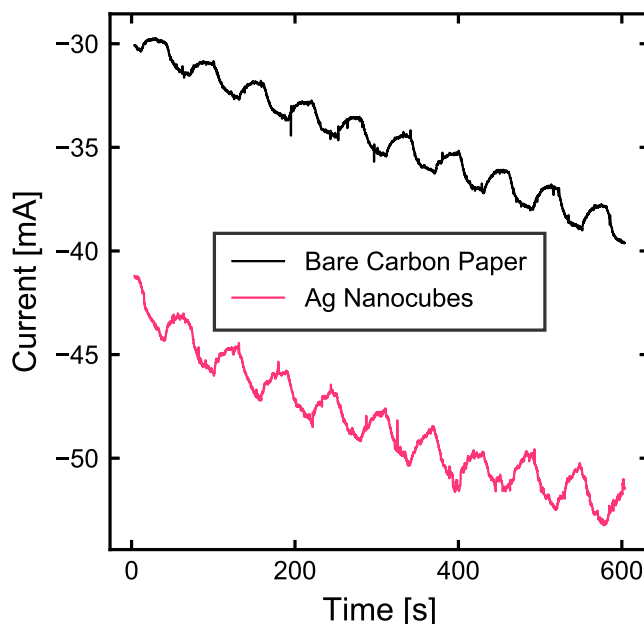
Figure 5.15: Chopped-light CA over Ag nanocubes drop-cast on P75 carbon paper and bare P75 carbon paper in CO_2-saturated 0.05 M K_2CO_3 with 300 mW cm^{-2} solar simulated light. The current magnitude increases when the photocathode is illuminated and decreases when the light is blocked. Note that the electrodes do not have the same geometric surface area, and the current is not normalized to the electrode area.

Drop-Cast 5 nm Ag Nanospheres

40 µL of 5 nm Ag spheres were drop-cast onto a circular 0.5 cm^2 area of a 30 nm thin film of e-beam evaporated Ag on a 3 nm film of e-beam evaporated titanium on glass using a Teflon mask to keep the nanoparticles from spreading out beyond the well-defined surface area (Figure 5.16). This electrode produced a maximum of 300 µA cm^{-2} of photocurrent in linear sweep voltammetry (LSV) from 0.2 to 1.2 V_{RHE} in CO_2-saturated 0.05 M K_2CO_3 with 500 mW cm^{-2} solar-simulated illumination (Figure 5.17a) as compared to 30 µA cm^{-2} for the same electrode without nanoparticles. The photocurrent density increases with increasing cathodic voltages until it reaches a maximum at -0.9 V_{RHE} where it begins to decrease.

On subsequent chopped-light LSV scans on the 5 nm Ag nanosphere electrode, the maximum photocurrent density increased and shifted to more anodic potentials (Figure 5.17b). After these three LSV scans, many nanoparticles could be seen floating on the surface of the electrolyte due to their bright color. However, the electrode's photoactivity was still an order of magnitude greater than the same electrode with no nanoparticles. This could indicated that many nanoparticles remained on the electrode surface or that the initial presence of nanoparticles on the Ag thin film electrode altered its morphology to make it more photoactive.

In the following sections, I outline strategies for improving adhesion between colloidal nanoparticles and conductive electrodes.
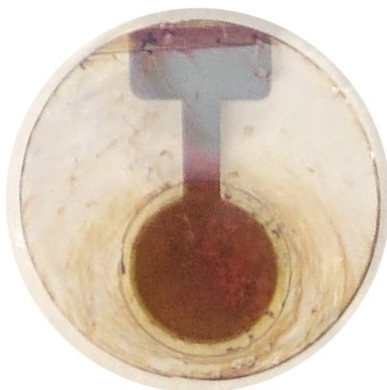
Figure 5.16: Photograph of 5 nm Ag nanospheres drop-cast on a thin film Ag electrode supported on a circular piece of glass. The circular area is immersed in the electrolyte and serves as the electrode. The active area is visibly red-tinted due to the presence of 5 nm Ag nanospheres. The top of the "T" shape above the circular area is used to make electrical contact to the electrode.

5.1.3 Molecular Tethers Between Nanoparticles and Supporting Electrodes

One strategy to improve nanoparticle binding to the conductive electrode is to use a linear molecular tether with one terminal functional group of the molecule bound to the nanoparticle and the other terminal functional group bound to the electrode. Here, we use a strategy inspired by Shein et al.[63] to bind the 5 nm Ag nanospheres to a Ag thin film electrode and improve charge transfer efficiency from the electrode to the nanoparticles using a self-assembled monolayer (SAM) of dithiol linkers according to the scheme in Figure 5.18. The dithiol linkers replace the nanoparticle's organic ligands on the side of the nanoparticle facing the electrode surface due to the higher affinity between the thiol functional group and the Ag metal than the nanoparticle's native ligands.

Glass slides with e-beam deposited 30 nm Ag on top of 5 nm Ti were soaked in 1 mM solutions of 1,2-ethanedithiol (Fluka, $\geq$98 %) and 1,6-hexanedithiol (SAFC, $\geq$ 97 %) in ethanol ($\geq$ 99 %) for 48 hours to form the SAM on the thin Ag surface. The electrodes were then rinsed thoroughly in ethanol and ultrapure water. The electrodes were then soaked in 100 µL of 5 nm Ag nanospheres diluted to 3 mL in hexane for 18 h. The hexane solvent evaporates in this time, so the dry electrodes were rinsed gently in hexane.

photoelectrochemistry (PEC) performance of these electrodes was evaluated using IR-corrected 3 Hz chopped-light LSVs in CO_2-saturated 0.05 M K_2CO_3 in a quartz-windowed beaker (Figure 5.13) with a lock-in amplifier and solar simulator lamp with a convex lens to increase the light intensity incident on the cell to > 300 mW cm^{-2}. Bare Ag thin film electrodes did not exhibit any photocurrent or reductive peaks. Ag thin film electrodes modified with 1,2-ethanedithiol SAMs exhibited a reductive peak at -1.0 V$_{RHE}$ on the first reductive LSV scan; those with 1,2-hexanedithiol SAMs exhibited a reductive peak at -1.1 V$_{RHE}$ on the first reductive LSV scan. The reductive peaks are likely the result of the reduction of the unbound thiol group of the molecular tethers. Both dithiol SAM electrodes
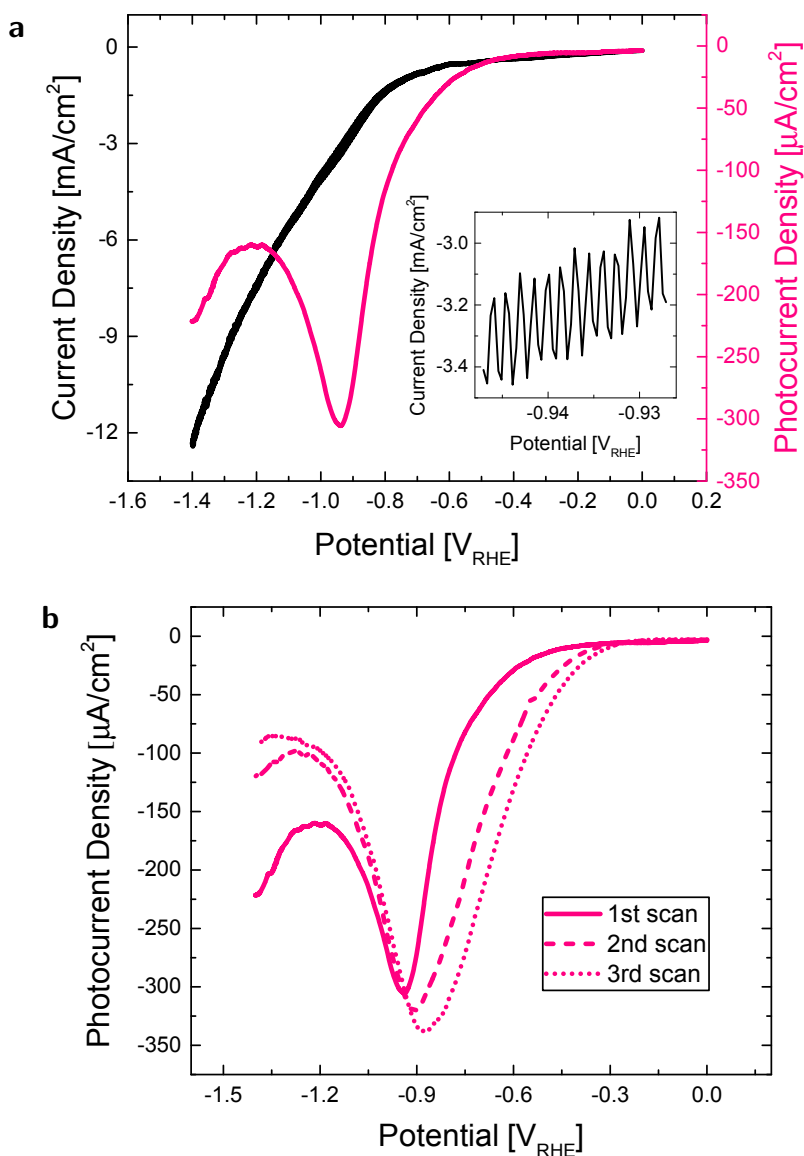
Figure 5.17: Chopped-light LSV over 5 nm Ag nanospheres drop-cast on a Ag thin film substrate in CO_2-saturated 0.05 K_2CO_3 under 1 Hz modulated 500 $mW\,cm^{-2}$ solar-simulated illumination. (a) Total current density and photocurrent density for the first chopped-light LSV. The inset shows the total current density enlarged for visualization of the increase and decrease in current magnitude as the light was turned on and off, respectively. (b) Photocurrent density comparison among three chopped-light LSV sweeps.
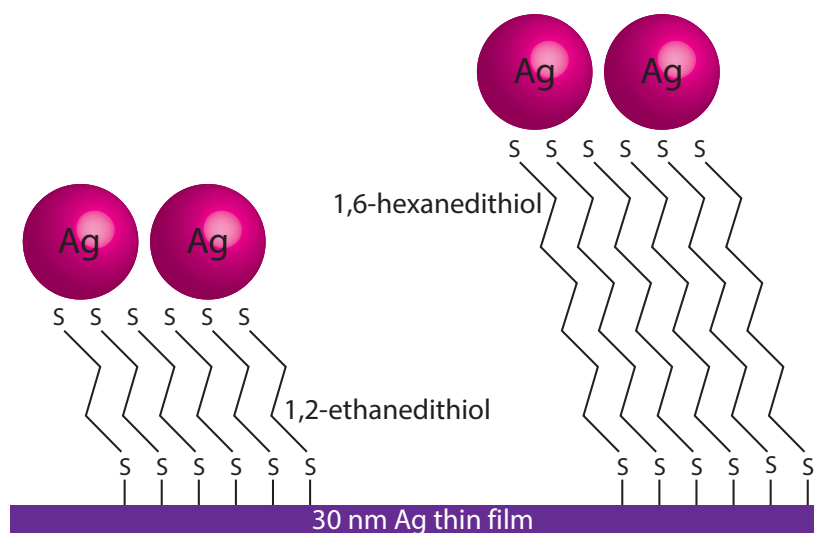
Figure 5.18: Schematic representation of two types of dithiol SAM-modified thin film Ag electrodes. Electrodes are modified with either 1,2-ethanediothiol or 1,6-hexanedithiol and then subsequently modified with a monolayer of 5 nm Ag nanospheres. This cartoon is not drawn to scale as the diameter of the nanoparticles is much larger than the length of the molecular tethers.

exhibited a sharp decrease in photocurrent at the thiol reduction potential and at -0.65 V_{RHE}. Subsequent LSV scans show no reductive peaks or dips in photocurrent, but the photocurrent magnitude is significantly lower than the photocurrent in the first LSV scan. The high photocurrent on the first scan was likely due to electron transfer to the unreduced thiol groups.

Dithiol SAM electrodes with 5 nm Ag nanospheres showed no visible reduction peak in the LSV at potentials down to -1.1 V_{RHE}, but they do show a dip in photocurrent at -0.65 V_{RHE}. The cathodic limit of the LSV scan was set based on the reduction potential of the dithiol electrode without nanoparticles. The ethanedithiol-tethered Ag nanosphere electrode exhibited a stable photocurrent maximum of 13 µA at -0.9 V_{RHE}. The hexanedithiol-tethered Ag nanosphere electrode's photocurrent decreased slighty with each subsequent scan. The ethanedithiol molecular tethers may bind the Ag nanospheres more strongly or may form a SAM with fewer defects than the hexanedithiol tether SAM. However, additional studies are needed to determine the mechanism for the difference in performance between the ethanedithiol and hexanedithiol tethers. The photocurrent magnitude of nanoparticle-tethered electrodes were comparable to their SAM-only counterparts. The PEC performance trends were the same when dry solvents were used and the dithiol molecular tethers and the nanoparticles were self-assembled under inert atmosphere.

To increase photocurrent, the number density of tethered nanoparticles should be increased. Gold has an especially high affinity for thiol groups, so switching to gold nanoparticles and a gold substrate as in Shein et al.[63] may improve adhesion. The integrity of the dithiol SAM may be improved by (1) modifying the metal film with the SAM shortly after metal film deposition to minimize metal oxidation, (2) increasing the temperature during self-

assembly to $> 25\,°C$, (3) decreasing the self-assembly time to 12 to 18 h, and (4) limiting light exposure which may cause the thiols to react photochemically.[64,65] This route was not pursued further due to the electrochemical instability of the dithiol tethers. Other promising molecular tether options are benzene-1,4-dithiol, 1,4-diethynylbenzene, cysteamine, 1,4-dicyanobenzene, and ethylenediamine due to their short chain lengths and symmetric binding groups. Conjugated molecular tethers may improve charge transfer over alkyl-based tethers due to their increase charge conductivity. Amine or ethynyl binding groups may improve electrochemical stability when binding Ag nanoparticles. Ultimately, molecular tethers will likely limit the electrochemical potential window of these electrodes.

5.1.4 Sputter Deposition over Drop-Cast Nanoparticles

The goal of this strategy for improving colloidal nanoparticle adhesion to electrodes is to deposit a thin layer of metal over the nanoparticles on an electrode to adhere them to each other and the electrode. Nanoparticles are drop-cast onto the conductive electrode substrate and a thin film of metal of the same element as the nanoparticles is sputter deposited over the them. To prepare the nanoparticle electrodes, 2.5 to $40\,µL$ of 5 nm Ag nanospheres was drop-cast through a Teflon mask onto a 0.5 cm^2 circular area of a thin film Ag electrode (30 nm Ag on 5 nm Ti on glass). 1 nm of Ag was sputter-deposited over the dried electrodes.

PEC performance of these electrodes was evaluated using IR-corrected 3 Hz chopped-light LSV and CA in CO_2-saturated 0.05 M K_2CO_3 in a quartz-windowed beaker (Figure 5.13) with a lock-in amplifier and solar simulator lamp. The sputtered nanoparticle electrodes exhibited photocurrent maxima at -0.8 V$_{RHE}$ ranging from 100 to $400\,µA\,cm^{-2}$ with the higher loadings of nanoparticles having higher photocurrent (Figure 5.19a). All nanoparticle-containing electrodes exhibited higher photocurrent than a similar electrode without nanoparticles except the electrode with $2.5\,µL$ of nanoparticles. The first LSV scan of the nanoparticle-containing electrodes exhibited little enhancement in photocurrent over the nanoparticle-free electrode, but the photocurrent in subsequent chopped-light LSV scans increased dramatically (Figure 5.19b). The electrochemical enhancement may be caused by electrochemical conditioning and morphology changes that enhance the plasmonic activity similar to that seen in Chapter 4.

Over 20 min of CA at -0.8 V$_{RHE}$, the photocurrent over the $40\,µL$ nanoparticle electrode decreased by 30 %, indicating that the sputter-deposition adhesion was not completely effective. However, a thin film Ag electrode with 1 nm of sputtered Ag but no nanoparticles also suffered a large decrease in the photocurrent magnitude over 20 min, indicating that an electrochemically induced change in the underlying Ag thin film may contribute to the decrease in photocurrent when nanoparticles are present.

In the next section, I discuss another method for depositing small amount of metal to bind the nanoparticles to the electrode and to each other.

5.1.5 Nanoelectrowelding

In this technique, like metal sputtering, a thin layer of metal is deposited to bind the drop-cast electrodes to the substrate and to each other. In this case, the metal is deposited by electrochemical reduction of metal ions in solution (Figure 5.20). The electrodeposition of Ag
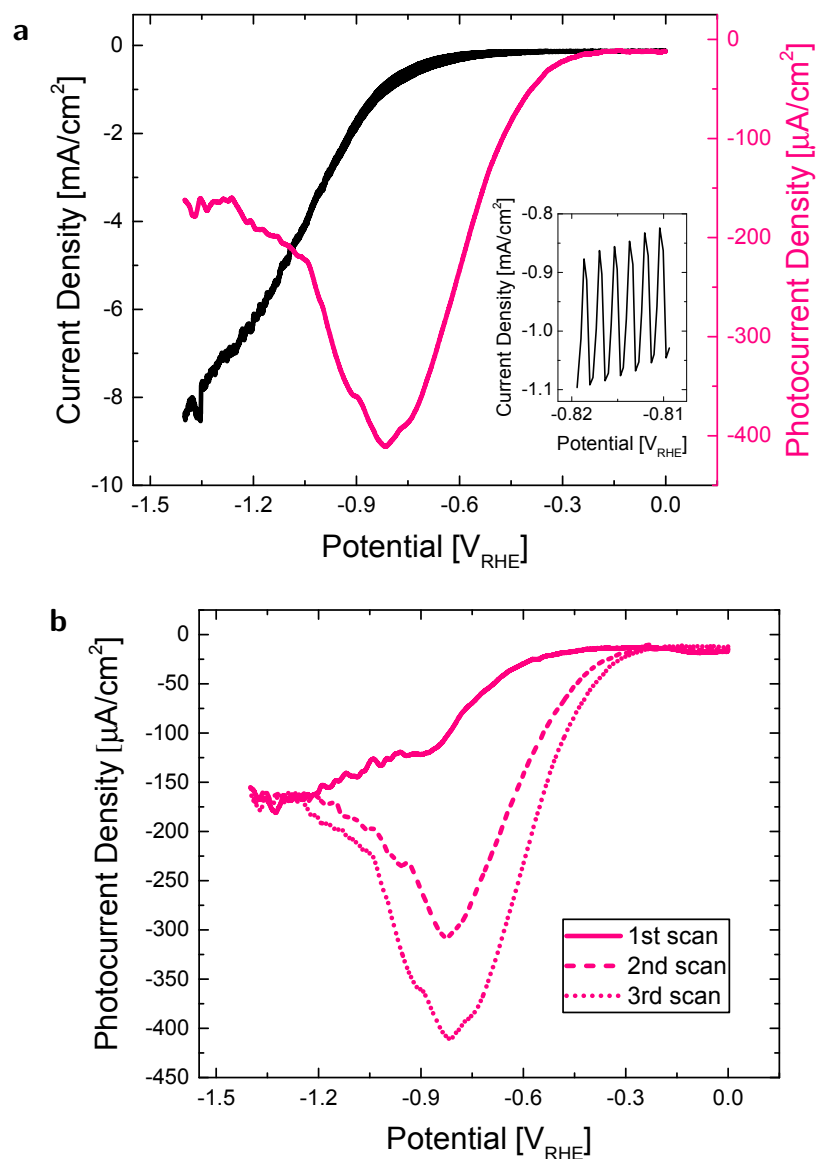
Figure 5.19: Chopped-light LSV over 40 μL of 5 nm Ag nanospheres drop-cast and coated with 1 nm of sputter-deposited Ag on a 0.5 cm^2 Ag thin film substrate in CO_2-saturated 0.05 K_2CO_3 under 1 Hz modulated 500 mW cm^{-2} solar-simulated illumination. (a) Total current density and photocurrent density for the third chopped-light LSV scan. The inset shows the total current density enlarged for visualization of the increase and decrease in current magnitude as the light was turned on and off, respectively. (b) Photocurrent density comparison among three chopped-light LSV sweeps.
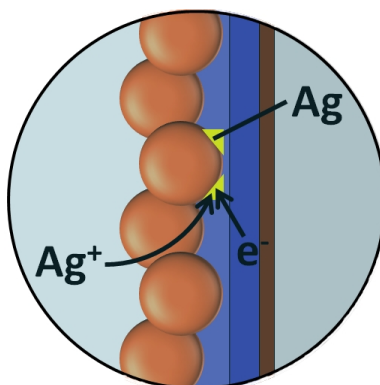
Figure 5.20: Idealized graphic of nanoelectrowelding where Ag ions (Ag^+) from the electrolyte solution are reduced by the electrons (e^-) passed from the electrode to form a solid Ag binding layer between the Ag electrode and the Ag nanoparticles.

is performed following the recipe for creating smooth and compact films of Ag in Zarkadas et al.[66]

Two nanoparticle loadings of 5 nm Ag nanospheres were deposited on thin film Ag electrodes. 10 or 40 µL of 5 nm Ag nanospheres were drop-cast through a Teflon mask onto a 0.5 cm^2 circular area of a thin film Ag electrode (30 nm Ag on 5 nm Ti on glass). After these electrodes dried, they were used as cathodes in the electrodeposition to achieve nanoelectrowelding of the nanoparticles to the Ag electrode substrate.

The electrodeposition electrolyte was a 25 mL aqueous solution of 0.2 M AgNO$_3$ (Sigma-Aldrich $\geq$99.9 %), 0.0015 M DL-tartaric acid (Aldrich, 99 %), and 0.03 M nitric acid (HNO$_3$) which had a pH of 1.64. Electrodeposition in the nanoelectrowelding was performed in the two-electrode configuration with the active surface of the nanoparticle electrode facing the platinum anode. If electrodeposition for 47 min at 0.02 A cm^{-2} gives a Ag film of approximately 60 µm, then a 1 nm thick Ag thin film over an electrode of 0.5 cm^2 will be deposited in 0.047 s at 0.01 A or in 0.94 s at 0.5 mA, assuming that all current is Faradaic, not capacitive. To account for the capacitive effect, two electrodes for each nanoparticle loading were nanoelectrowelded at 0.5 mA—one for 0.94 s and one for 3.76 s (four times as long). The electrodes that were nanoelectrowelded for 3.76 s visibly appeared more silver in color after the deposition.

PEC performance of these electrodes was evaluated using IR-corrected 3 Hz chopped-light LSV and CA in CO$_2$-saturated 0.05 M K$_2$CO$_3$ in a quartz-windowed beaker (Figure 5.13) with a lock-in amplifier and solar simulator lamp. The nanoelectrowelded electrodes exhibited photocurrent maxima at -0.8 V$_{RHE}$ ranging from 140 to 350 µA cm^{-2} with the higher loading of nanoparticles having higher photocurrent. The performance of these electrodes was very similar to the performance of the sputter deposited nanoparticle electrodes in that the maximum photocurrent increased in the three LSV scans over the previous scan and the photocurrent over 20 min at -0.8 V$_{RHE}$ diminished significantly. This result indicates that nanoelectrowelding does not seem to be an effective strategy in stabilizing colloidal nanoparticle electrodes for PEC CO$_2$R.

5.1.6 Nafion Binding of Nanoparticle Electrodes

Nafion, which is a sulfonated tetrafluoroethylene polymer, has been widely studied as a binding agent and cation conducting membrane in fuel cells and other applications due to its high chemical stability and ease of handling through solution-based processing.[67] Several studies have used Nafion to bind nanoparticles (including colloidal nanoparticles) to conductive substrates for electrochemical applications.[68,69] Here, hydrophilic 5 nm Ag nanospheres are Nafion-bound to a Ag thin film surface as a CO_2R photocathode.

The Nafion binder solution was made by mixing 100 µL isopropanol with 100 µL Nafion 117 (Aldrich, 5 % Nafion in a mixture of lower aliphatic alcohols and water). Hydrophilic 5 nm Ag nanospheres were deposited by drop-casting 0.68 mL on a circular 0.5 cm² Ag thin film e-beam deposited electrode (30 nm Ag on 5 nm Ti on glass) targeting a Ag concentration of 1.414 mg cm^{-2}. 14 µL of the Nafion binder solution was drop-cast over the nanoparticles after the solvent had evaporated.

PEC performance of these electrodes was evaluated using IR-corrected 3 Hz chopped-light LSV sweeps from 0 to -1.2 V$_{RHE}$ in CO_2-saturated 0.05 M K_2CO_3 in a quartz-windowed beaker (Figure 5.13) with a lock-in amplifier and solar simulator lamp. The Nafion-bound nanoparticle electrodes exhibited photocurrent maxima of 350 µA cm^{-2} at -1 V$_{RHE}$ on the first scan. Unlike the Nafion-free drop cast nanoparticle electrodes, the Nafion-bound nanoparticle electrodes maintained similar photocurrent density for at least six LSV sweeps. However, the Nafion-only thin film Ag electrode exhibited photocurrent maxima of 300 µA cm^{-2} at -0.9 V$_{RHE}$ on the first scan and maintained similar photocurrent for at least six LSV sweeps. We are not able to determine whether the photoactivity over Nafion in CO_2-saturated electrolyte was caused by Nafion-induced CO_2R or degradation of the Nafion itself without CO_2R product analysis. The Nafion-only electrode did not exhibit measurable photocurrent in Ar-saturated electrolyte. The most likely reason for the increased photoactivity of the Nafion-coated electrode is the UV absorption of the polymer,[70] although Nafion may also serve to increase the CO_2 concentration at the surface of the electrode by preferentially solubilizing the CO_2 over inert, nonpolarizable gases. Despite the improvement in stability achieved through Nafion binding, Nafion is not a suitable adhesion solution for a fundamental study of plasmonic PEC CO_2R in which all photoactivity is derived from the plasmonic effect given the photoactivity induced by the Nafion film itself.

5.1.7 Suggested Next Steps

While I was unable to find a method to achieve stable binding of colloidal nanoparticles to a cathode surface, there are several promising methods that I have not yet explored. The organic ligands seem to be the largest barrier to using colloidal nanoparticles as the plasmonic catalyst for PEC CO_2R due to their electrochemical instability and blocking a stable interface between the conductive support and nanoparticle. Here, I outline two possible techniques for synthesizing ligand-free nanoparticles.

Annealing

When a colloidal nanoparticle film is annealed in the presence of oxygen, the organic ligands are burnt away, leaving only the inorganic cores. However, small metal nanoparticles such as Au or Ag nanoparticles sinter under only moderate heating conditions[71] because their surface energy is so high. Many metal oxides do not suffer the same fate under annealing conditions; a thin shell of metal oxide such as TiO_2, SiO_2, or Al_2O_3 coating a plasmonic nanoparticle may not only prevent agglomeration but also help to facilitate charge separation through injection of plasmonic hot electrons or holes into the metal oxide. The (gold core)/(titania shell) colloidal synthesis needs to be improved to increase the yield of core-shell nanoparticles and decrease the titania shell thickness.

Alternatively, metal nanoparticles can be co-synthesized with a porous metal oxide in sol-gel synthesis techniques[72–75] or grown on a metal oxide or carbon black support[76] followed by annealing to remove the ligands. The metal oxide serves as a physical barrier for sintering. Of note, metal oxide stability is a critical consideration when biasing electrodes the reductive potentials necessary for CO_2 reduction. Therefore, probing reductive stability of any nanoparticles that contain a metal oxide shell should be among the first properties studied of these materials.

Ligand-Free Synthesis Methods

Solution-based monodisperse nanoparticles can be grown on a solid or polymer support without the need for surface ligands. For example, Ag nanoparticles were electrodeposited from a $AgNO_3$ solution on a Nafion-modified glassy carbon electrode to form an effective electrode for the electroreduction of potassium dichromate ($K_2Cr_2O_7$).[68] However, this reduction reaction occurs at modest potentials, so it is unclear whether a similar electrode would be stable under the strongly reducing conditions in electrochemical CO_2R.

Photoreduction has not been explored here as a solution-based nanoparticle synthesis method, but it may offer improvements in adhesion between the nanoparticles and the substrate which serves as a nucleation point during the synthesis.

5.2 Electron-Beam Lithography[4]

Colloidal nanoparticle synthesis is a "bottom-up", solution-based approach to creating uniform, size-controlled nanoparticles, but another option for creating uniform, size-controlled nanostructures is a "top-down" approach such as e-beam lithography. In e-beam lithography, a focused beam of electrons is used to draw custom shapes on a surface. The advantage of this method over colloidal synthesis is that the nanofeatures and conductive substrate can easily be synthesized in one monolithic material, so adhesion of the nanostructures to the surface is not a challenge. The technique is limited to small surface areas due to the high processing time, chemical resists that change solubility with e-beam exposure, substrates that can be spin-coated with a uniform resist layer, and larger-sized nanofeatures than are available with solution-based synthesis methods.

---

[4]This section describes joint work with Davis Perez. Scott Dhuey performed the e-beam lithography.

Lumerical software was used to perform finite-difference time-domain (FDTD) simulations of an array of gold nanopillars on a gold substrate (Figure 5.21a) to determine the combination of pillar height, spacing, and radius that would result in the maximum absorbance in solar spectrum. A broadband plane wave light source was used in the model along with a near field monitor at the surface of the pillars to measure the enhancement in electric field and a reflection monitor behind the light source to measure light that is not absorbed by the nanopattern (Figure 5.21b). These simulations predict that the highest solar absorption for gold nanopillars can be achieved with a nanopillar height of 58 nm, radius of 30 nm, and nearest-neighbor spacing of 24.8 nm. With these dimensions, the electric field on the sides of the pillars is predicted to be three times the magnitude of the incident field at the point closest to its nearest neighbor pillar (Figure 5.21c). E-beam lithography was used to create the optimized nanopillar pattern.

Initially, an e-beam deposited gold film supported on a glass slide was used as the e-beam lithography substrate. Then, additional gold was deposited through the resist mask to form the gold nanopillars. However, poly(methyl methacrylate) (PMMA) and ZEP 520A (Zeon) do not coat the gold surface well enough to achieve high fidelity lithography.

However, e-beam lithography on Si is a common technique. The inverse of the desired pattern can be formed on a Si wafer, after which gold is deposited to fill the inverse pattern. Upon removal and post-treatment, the desired gold pattern is then achieved. Template stripping is a well-known technique for removing thin metal films from ultra-flat, well-defined substrates such as Si.[77–80] In template stripping, a metal film is deposited on a template surface followed by an adhesion layer to attach a rigid supporting substrate. Finally, the sandwich structure is mechanically cleaved at the weakest interface to reveal the metal surface with the same morphology as the template surface (Figure 5.22).

For lithographied and template-stripped electrodes, the key factor in determining electrode viability is the adhesion layer between the gold film and rigid support. Here, the use of epoxies, double-sided carbon tape, liquid glass, and adhesiveless cold welding are investigated as gold-substrate binding agents.

Loctite EA 615, Torr Seal, and several other epoxy resins were screened for effectiveness as an adhesion layer. However, due to unavoidable imperfections (small tears in the gold film) in the large area (> 3 cm^2) electrode, electrolyte and the resist wash solvent were able to penetrate between the gold film and the substrate resulting in the majority of the gold film peeling off before an electrochemical test could be performed (Figure 5.23a). This delamination was exacerbated by application of a voltage to the electrode, possibly due to the gas evolution at the gold surface. Though the two epoxies listed above have the most promising performance, using any epoxy as the adhesion layer is not a feasible solution for electrode areas 1 cm^2 or larger. Double-sided carbon tape, while easier to ensure a uniform thickness than epoxy (Figure 5.23b), ultimately suffered the same fate as the epoxy-adhered electrodes.

As a chemically inert and mechanically stable adhesion layer, template stripping studies have used sodium silicate solution ("liquid glass") followed by curing under low heat to evaporate all water and convert the material to sodium silicate glass.[78] The liquid glass adhesion technique used here is illustrated and discussed in Figure 5.22. However, the liquid glass adhesive proved to be unsuitable for the gold film on ZEP resist on a Si wafer because
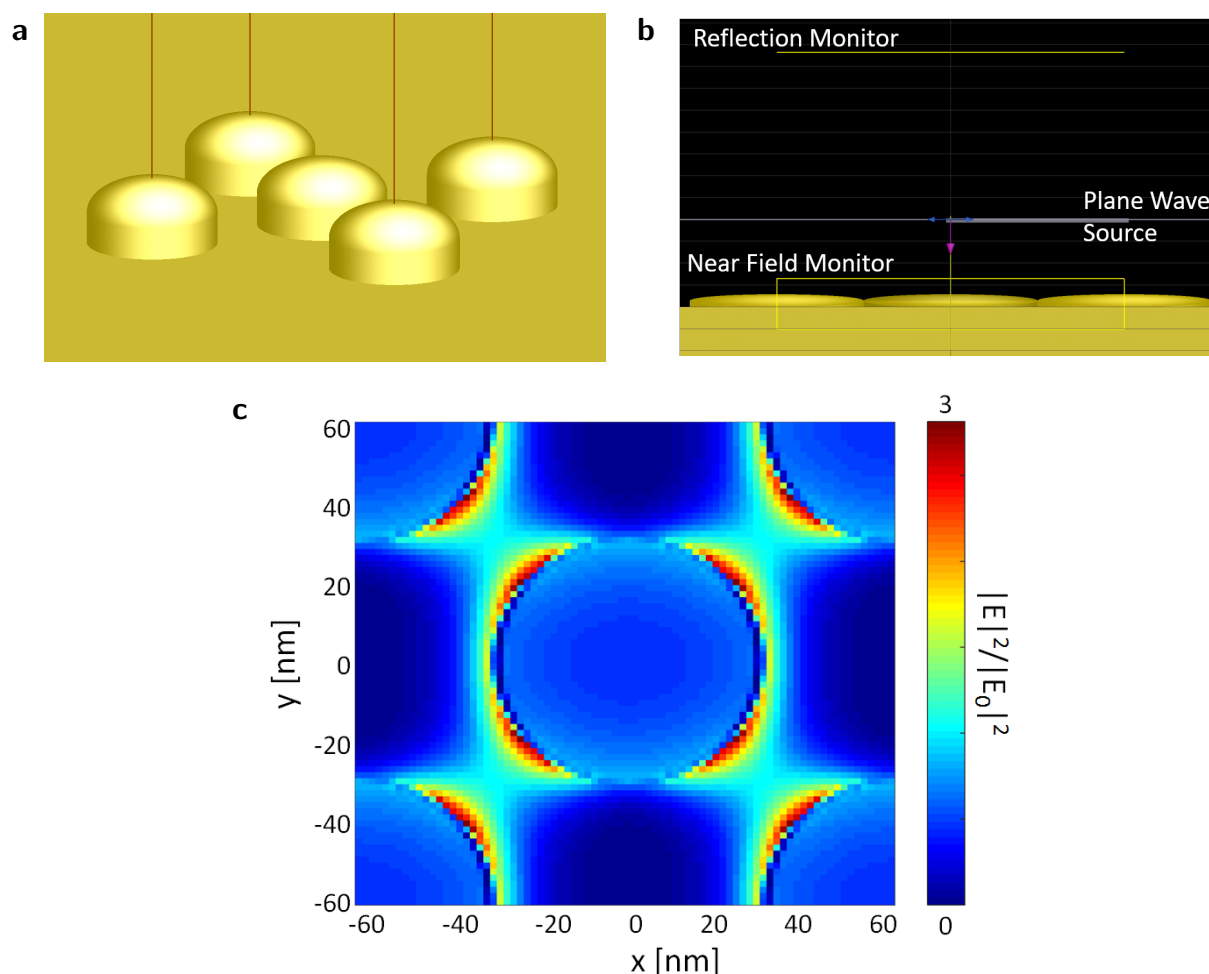
Figure 5.21: FDTD simulation model and field enhancement. (a) Perspective view of the nanopillar model. (b) In-substrate-plane view of the nanopillar model, light source, and monitors with periodic boundary conditions to simulate an infinite square array of nanopillars. (c) Simulated electric field enhancement expressed as a ratio of the square of the magnitude of the electric field generated $|E|^2$ to the square of the magnitude of the incident electric field $|E_0|^2$.

the gold film floated up through the liquid glass as the glass was drying (Figure 5.23c). This behavior was repeatable regardless of the presence of a metal adhesion layer (Ti or Cr) or solid support over the liquid glass during the curing process and regardless of whether the liquid glass was degassed before applying to the gold film. Additionally, the liquid glass usually did not dry in a smooth film but rather formed bubbles and wrinkles, making the substrate likely to crack when compressed in the CO_2R cell described in Chapter 3.

The most promising adhesion technique proved to be cold welding in which two metal surfaces are fused using a combination of hydrostatic pressure and low grade heating.[77,80] In this technique, no binding layer was applied to the gold film on the lithographied substrate. Rather, a thin metal adhesion layer such as Ti or Cr was deposited on the glass slide substrate followed by a layer of Au. The two gold surfaces were pressed together using a heated
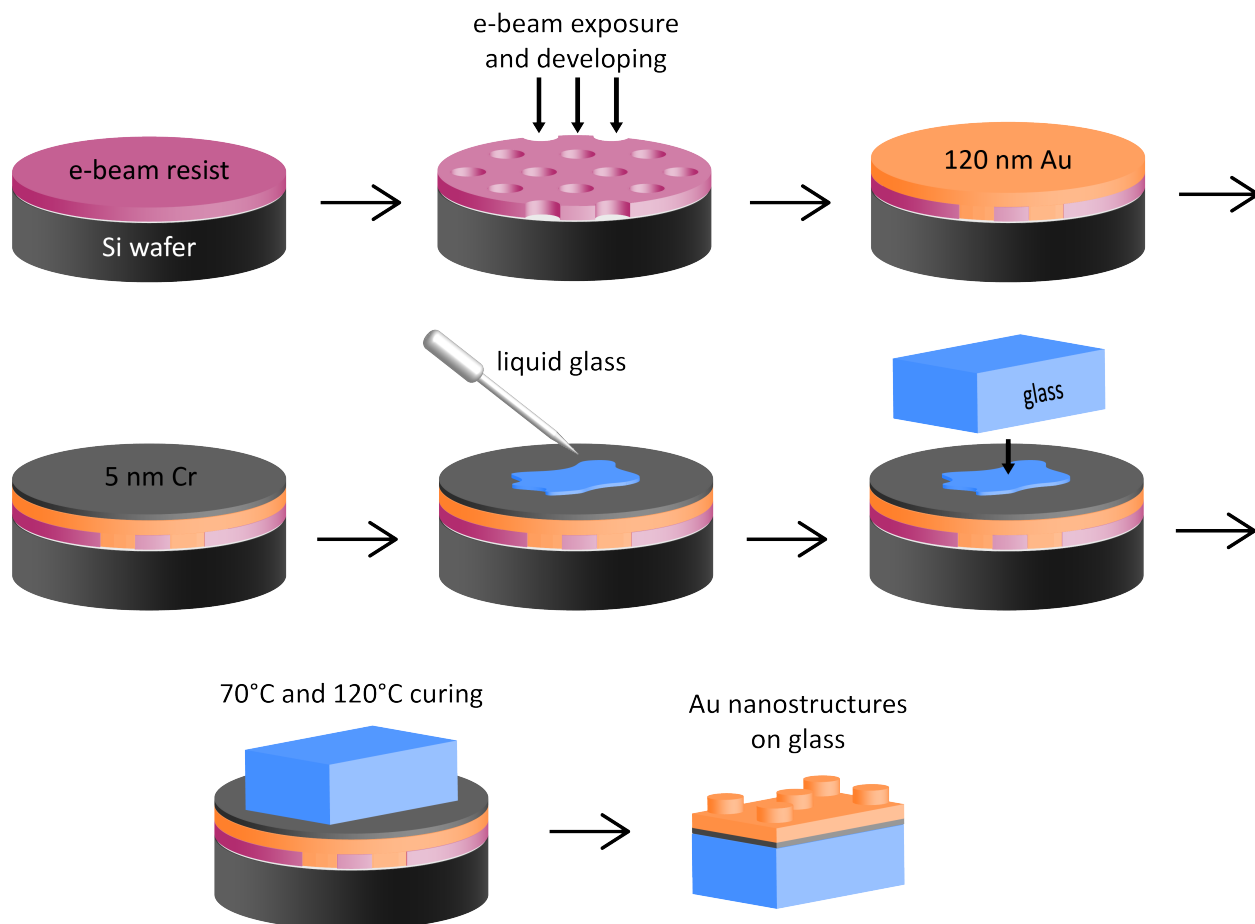
Figure 5.22: Schematic illustrating a typical e-beam lithography and template stripping procedure to create uniform arrays of Au nanopillars. An electron-sensitive film of resist material (ZEP 520A) on a Si wafer is selectively exposed to the electron beam to create the inverse of the desired gold nanofeatures. The resist is developed by a solvent rinse (xylene) to create the nanopillar template by rinsing away the areas in the resist where the nanopillars will be deposited. Next, 120 nm of Au followed by a 5 nm Cr or Ti adhesion layer is e-beam deposited over the developed resist. An adhesive such as liquid glass is applied to the adhesion layer to attach the substrate material. Liquid glass is cured by drying for 12 h at 70 °C followed by 12 h at 120 °C to harden the material. Finally, the film attached to the substrate is peeled off the Si wafer to expose the array of Au nanopillars. Excess resist is dissolved in a solvent such as dichloromethane.
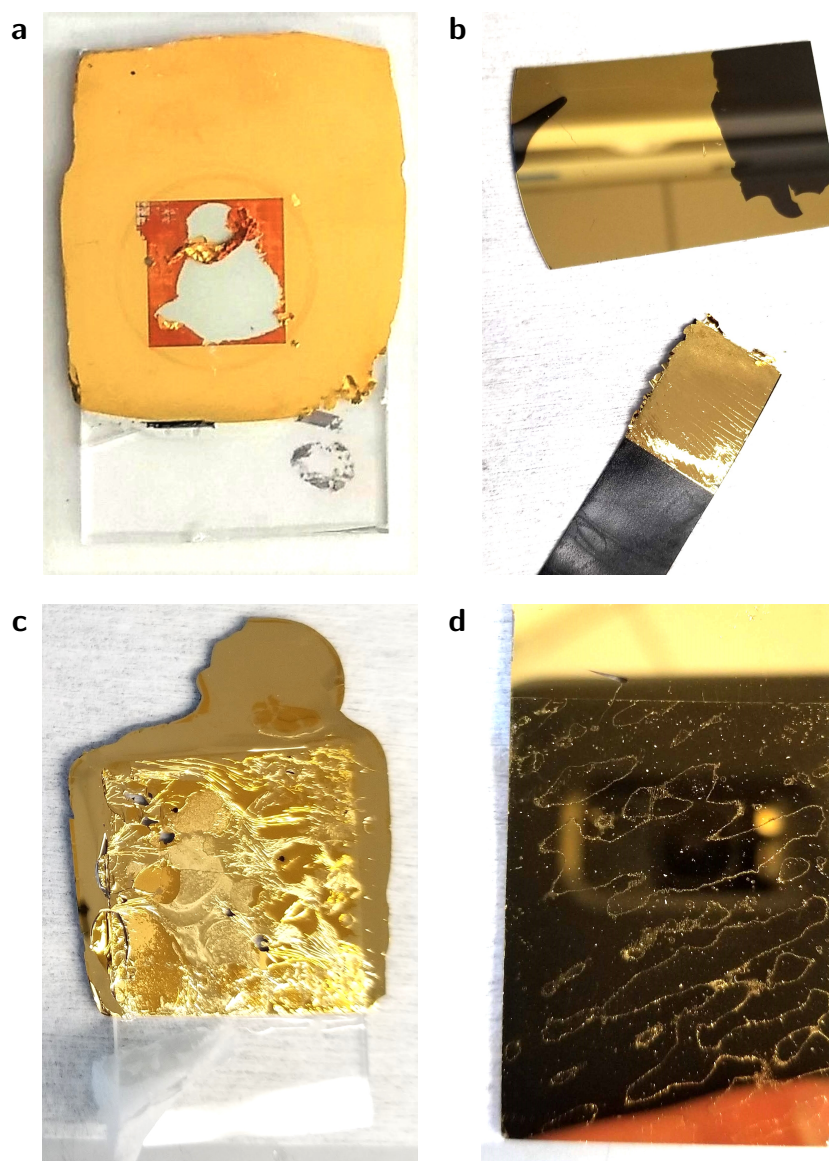
Figure 5.23: Photographs of template-stripped electrodes with four different adhesive strategies. (a) Torr Seal epoxy binder to a glass slide substrate achieves good transfer of the Au film except for micro-tears in the Au film that result in delamination during electrochemical testing. (b) Double-sided carbon tape binder (BOTTOM) achieves imperfect but straightforward film transfer from the substrate (TOP). (c) Liquid glass binder to a glass slide substrate causes the gold film to diffuse through the liquid glass as it is hardening. (d) Gold-to-gold cold welded electrode showing incomplete film transfer to the gold film on the glass slide substrate.

hydraulic press with pressures up to 1 metric ton and temperature set points up to 200 °C. The pressure was limited by the mechanical stability of the glass slide in the uneven bonding stack, and the temperature was limited by the boiling point of ZEP, 156 °C. While the cold welding technique achieved small areas electrochemically stable nanopatterned electrodes (Figure 5.24), the fidelity of the large area nanopattern was poor as complete transfer of the entire 1 cm^2 patterned area was never achieved (Figure 5.23d).
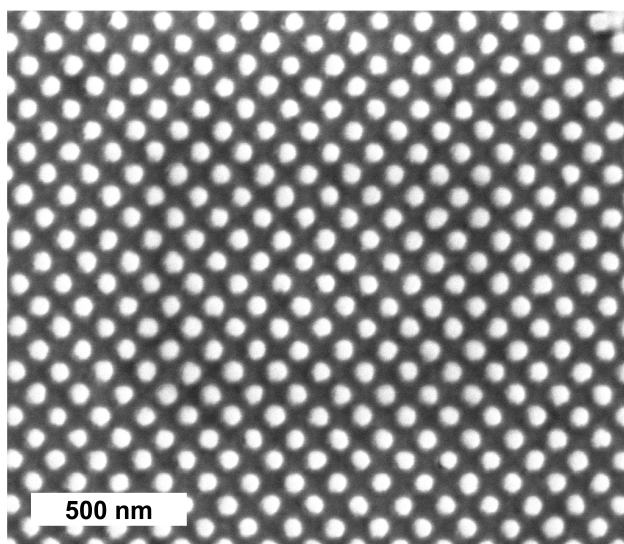
Figure 5.24: SEM image of template-stripped Au nanopillars. The pillars are 63 ± 2 nm in diameter and 30 nm in height.

The cold welding fidelity could be improved by depositing the gold and performing the cold welding in a clean room as soon as possible after metal deposition to limit any surface contamination on the metal which is extremely detrimental to metal-metal bonding.[77] In the case of e-beam deposition and cold welding in typical laboratory conditions, a pliable substrate may be beneficial in improving adhesion.[77] Perhaps the cold welding or liquid glass techniques could be improved by patterning the Si wafer, removing the resist, and using the bare patterned Si to avoid the temperature and chemical limitations of the resist.

5.3 Electrochemically Roughened Electrodes

Electrochemical roughening of electrodes is performed by applying successive oxidative and reductive potentials to metal electrode. During the oxidative cycle, metallic atoms are oxidized into cations that are solubilized in the solution. During the reductive cycle, these metal cations are reduced back to their metallic state on the surface of the electrode. The displacement of the metal atoms from their original position causes restructuring of the surface. It is important that the electrolyte is not stirred during electrochemical roughening because the oxidized metals cations need to be available at the electrode surface during the reduction cycle for redeposition.

1 mm thick Ag foils were wet-sanded with Norton T401 Black Ice 2000 grit sandpaper

followed by thorough rinsing in ultrapure water. The polished foils were electrochemically roughened in 0.1 M KCl in four CVs from -0.3 to $+0.3\,\text{V}$ versus 3 M Ag/AgCl reference electrode at a scan rate of $5\,\text{mV\,s}^{-1}$ followed by CA at -0.3 V versus the same reference for 5 min. The Ag foil electrode that was shiny and silver colored after polishing turned a dark gray during electrochemical roughening. SEM of the roughened Ag foil revealed uniform dendrite-like nanofeatures ranging from 60 to $300\,\text{nm}$ in width (Figure 5.25).
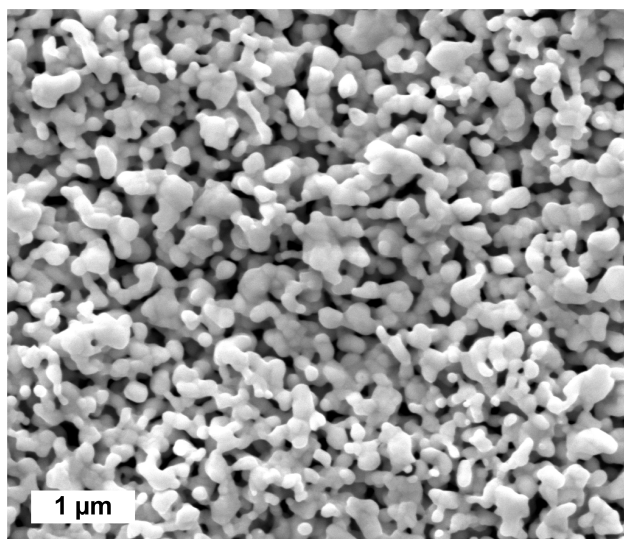
Figure 5.25: SEM image of electrochemically roughened Ag foil.
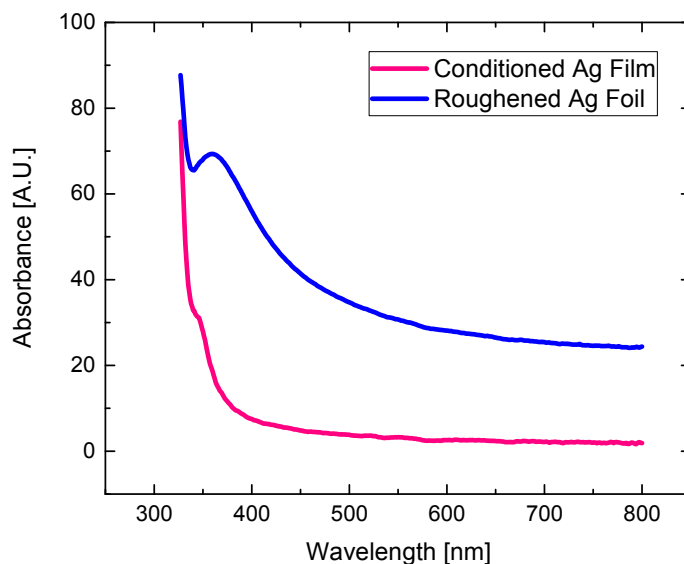
Figure 5.26: UV-visible absorption spectra for electrochemically roughened Ag foil and electrochemically conditioned Ag film. Absorption is calculated as $100\,\% - \%\text{R}$ where %R is the total reflection measured by an integrating sphere.

As is clear by eye, the electrochemically roughened electrodes have significantly higher

UV-visible absorbance across the spectrum than the electrochemically conditioned Ag thin films in Chapter 4 (Figure 5.26). However, the maximum photocurrent in chopped-light LSV sweeps is almost identical for the two electrode types (Figure 5.27). However, the potential of photocurrent maximum for the roughened Ag is anodically shifted by almost 0.2 V relative to that of the conditioned Ag. Additionally, the photocurrent onset potential for the roughened Ag is 0.1 V more anodic than that of the conditioned Ag and only 60 mV above the thermodynamic potential for CO formation.

Figure 5.27: Chopped-light LSV over electrochemically roughened Ag foil and electrochemically conditioned Ag thin film, as was studied in Chapter 4. Black and pink lines represent the total current density and the photocurrent density, respectively, over an electrochemically conditioned Ag film. Gray and blue lines represent the total current density and the photocurrent density, respectively, over an electrochemically roughened Ag foil.
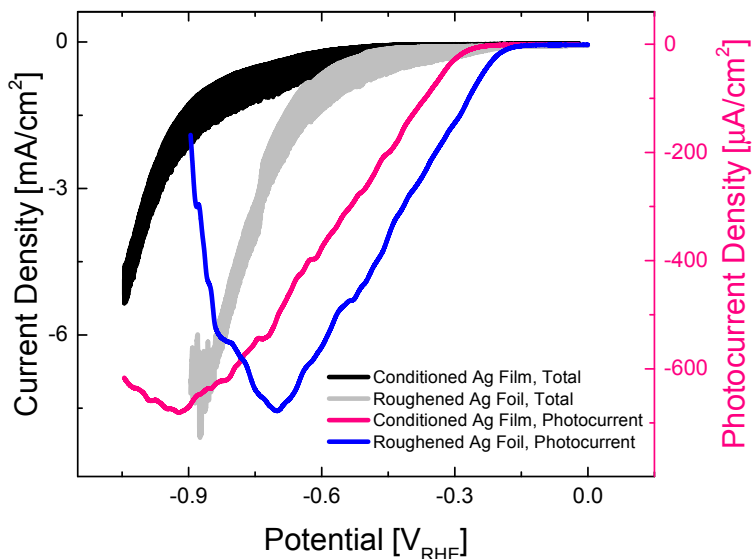
The roughened Ag demonstrated a higher partial current density toward CO at -0.6 and -0.35 V_{RHE}, likely due to its higher total current density and higher electrochemical surface area (ECSA) per geometric area than the conditioned Ag (Figure 5.28a). While the product generation rate was too low at -0.35 V_{RHE} to accurately quantify and H_2 was not detected, I extrapolated the CO calibration curve to smaller peak areas to report the CO partial current density here. The relative increase in Faradaic efficiency and partial current density for CO at -0.6 and -0.35 V_{RHE} was smaller over roughened Ag foil than the relative increase in CO over conditioned Ag thin film. Additionally, the conditioned film exhibits a greater relative suppression in H_2 production at -0.6 V_{RHE} (Figure 5.28b). This may be due to the larger dark current of the roughened electrode compared to the conditioned electrode at these potentials. From the results presented in Chapter 4, we expect that the dark current is substantially related to H_2 evolution close to the current onset, as is the case for both electrodes here. Given that the roughened electrode has a larger dark current at -0.6 and -0.35 V_{RHE}, the Faradaic efficiency for CO formation is slightly lower than the conditioned

electrode.
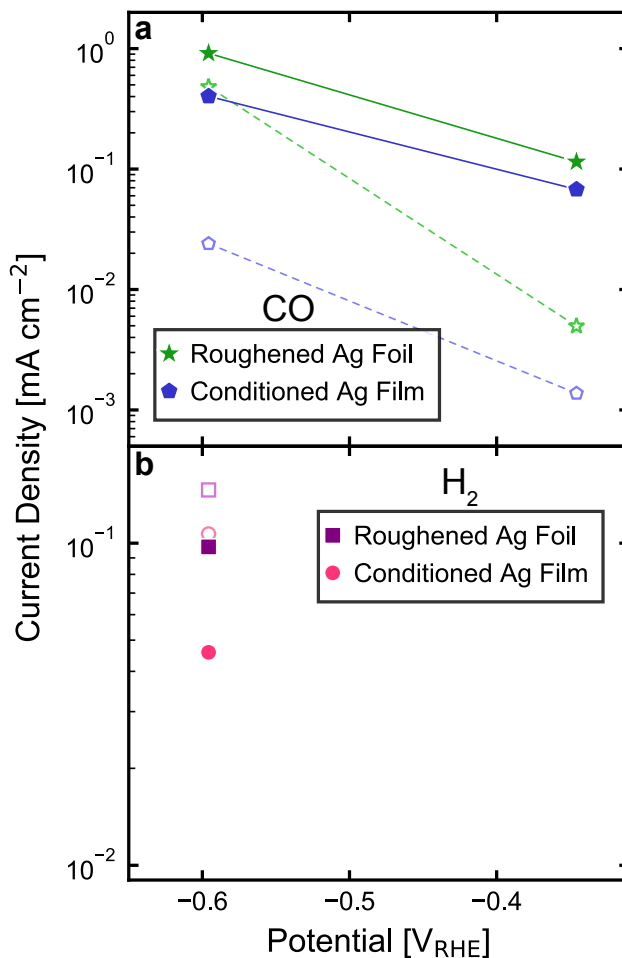
Figure 5.28: Tafel plot of the partial current density for each CO_2R product over an illuminated and dark roughened Ag foil and conditioned Ag film cathode. Filled symbols with solid lines represent data collected under 365 nm LED illumination at 170 mW cm^{-2}. Open symbols with dashed lines represent data collected without illumination. (a) Partial current densities of CO. (b) Partial current densities of H_2.

The roughened Ag electrode also exhibits the same behavior in illuminated and unilluminated LSV sweeps as the conditioned Ag. Illumination increases overall activity during electrolysis in CO_2-saturated electrolyte (Figure 5.29a) but decreases overall activity during electrolysis in Ar-saturated electrolyte (Figure 5.29b). Thus, the roughened and conditioned Ag electrodes both demonstrate selective enhancement of CO_2R and suppression of hydrogen evolution reaction (HER) during electrolysis.

The electrochemically roughened Ag electrodes are promising candidates for improvement over the PEC CO_2R performance seen in the electrochemically conditioned Ag thin film electrodes reported in Chapter 4 due to their significantly higher absorption and lower onset potentials. However, further optimization is needed to achieve higher photocurrent densities and possibly a difference in selectivity versus its conditioned thin film counterpart.
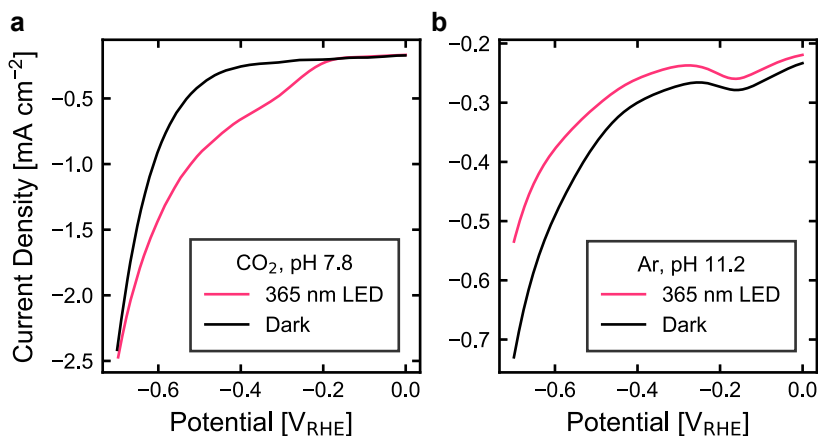
Figure 5.29: Cathodic voltage sweep at 100 mV s^{-1} at an illuminated and dark electrochemically roughened Ag electrode in (a) CO_2- and (b) Ar-saturated 0.5 M K_2CO_3 under 365 nm light-emitting diode (LED) light at 170 mW cm^{-2}.

Suggestions for improvement are decreasing the thickness of the roughened surface to improve mass transport of CO_2 to the buried photoactive nanostructured surface or changing the electrochemical roughening electrolyte to alter the size and morphology of the nanostructures formed by roughening.

5.4   Conclusion

I have presented synthesis and initial characterization of colloidal, lithographic, and electrochemical nanostructured electrodes. Intentionally nanostructured electrodes exhibit promising increases in plasmonic photocurrent and absorbance over thin film polycrystalline Ag electrodes, but their structural and electrochemical stability remains a challenge. The most stable electrodes were the electrochemically roughened electrodes, which indicates that the conditions of synthesis may dictate the environment in which the electrode is most stable.

Chapter 6

Outlook

6.1   Conclusions

Best practices for photoelectrochemistry (PEC) measurements were suggested for reproducibility and comparison of data sets collected under disparate conditions. A PEC carbon dioxide reduction (CO_2R) cell was developed to allow for front illumination of the photocathode and precise gaseous and soluble product quantification. The PEC cell and techniques were used to evaluate the effect of plasmonic excitement on nanostructured cathodes.

6.1.1   Photoelectrochemical CO_2 Reduction Cell

The design of the CO_2R cell that allows for front-illumination of an electrode was based on a well-established compression cell for dark CO_2 electrolysis. The cathode and anode were kept parallel but offset to allow light to shine beneath the anode and through the catholyte to illuminate the photocathode. Due to the large flux of light and the small volume of the electrochemical cell, temperature regulation was paramount. Elevated temperatures increase the overall activity but also promote hydrogen evolution reaction (HER), which would obscure the plasmonic effects of increased overall CO_2R activity and suppression of HER. Critically, the PEC cell allows accurate quantification of both liquid and gaseous products, and the CO_2R performance in the PEC cell matches that in the standard electrochemistry (EC) cell.

6.1.2   Plasmon Driven Changes to CO_2 Reduction Selectivity

The development of the PEC CO_2R cell allowed the efffect of plasmon excitation on CO_2R to be precisely measured for the first time. The photoactivity over a silver thin film electrode was completely selective for the CO_2R reaction over the competing HER. In fact, the overall H_2 generation rate decreased upon plasmonic excitation. Remarkably, the photoeffect decreased the overall activity in Ar-saturated (rather than CO_2-saturated) electrolytes. This behavior may be caused by the plasmonic generation of transient negative ion (TNI)s which promote further reactivity in the case of carbon-containing intermediates and promote desorption induced by electronic transitions (DIET) in the case of HER intermediates.

The CO_2R product promoted by the plasmonic effect depended on the applied potential. The silver thin film is able to generate CO at over 90% Faradaic efficiency at significantly lower overpotentials when illuminated than unilluminated. At low overpotentials, the plasmonic photoactivity is selective for CO production, but at higher overpotentials, the plasmonic photoactivity is selective for soluble products formate and methanol. To date, no comprehensive theory of plasmonic catalysis mechanisms incorporates the effect of a voltage bias. The simultaneous promotion of CO_2R and suppression of HER by plasmonic excitation is a fascinating phenomenon that will spark significant future work in tuning or enhancing the effect and understanding the mechanism for plasmon driven electrochemical CO_2R.

6.2 Suggested Future Work to Explore the Plasmonic Mechanism

6.2.1 Electrochemical Reduction of Possible Intermediates

A popular strategy in mechanistic exploration of CO_2R and other reactions is to introduce a suspected reaction intermediate to the reaction environment and record the activity and product distribution. An enhancement in activity or increased generation of a particular product may indicate that the introduced species is an intermediate in the reaction. While this approach cannot guarantee that a particular species is a reaction intermediate, it can offer valuable clues about the reaction mechanism. CO is a commonly predicted intermediate for many > 2 electron CO_2R products, so CO reduction is used to gather insight into the production of multi-electron products from CO_2.[37,81] However, this strategy has not been employed for Ag cathodes or plasmonic CO_2R. Unilluminated Ag cathodes have a low binding strength for CO and produce little to no > 2 electron CO_2R products,[2,10] making CO reduction unlikely to yield any detectable products. However, the amounts of formate and methanol generated at plasmonically excited Ag cathodes may allow these liquid products to be detected from CO reduction over Ag if CO is an intermediate species.

It is especially important in CO reduction over Ag electrodes that the CO be free of any trace levels of CO_2, a common contaminant in commercially available CO sources, because Ag is so much more active toward CO_2 than CO. CO reduction over Ag will likely only produce trace reduction products if it produces any at all, so it is imperative that all carbon products can be attributed to CO reduction rather than CO_2 contamination.

6.2.2 Surface Sensitive Spectroscopy[5]

Directly detecting the chemical species present at the surface of the electrode under illuminated conditions and comparing them to those under unilluminated conditions may provide insight into the mechanism of plasmon-driven changes to selectivity in electrochemical CO_2R. There are several possible spectroscopies that may allow detection of surface species (e.g. sum frequency generation spectroscopy, in situ surface-enhanced Raman spectroscopy (SERS), and operando attenuated total reflectance (ATR)-Fourier transform (FT) infrared (IR)). Operando

---

[5]This section describes joint work with Davis Perez.
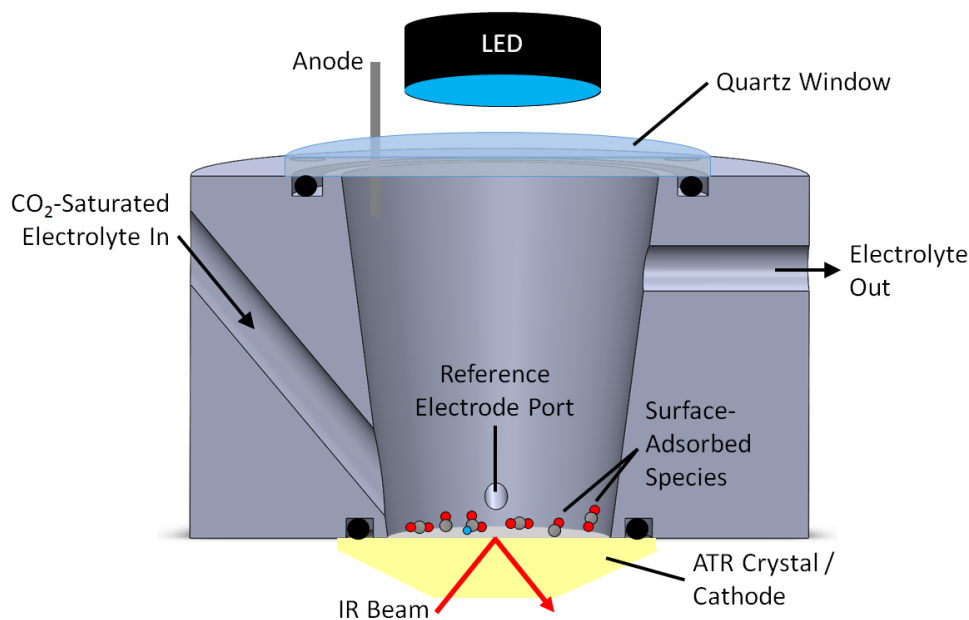
Figure 6.1: Schematic representation of a cross-sectional view of the ATR-FTIR cell. The black circles represent the cross sections of o-rings.

ATR-FTIR and in situ SERS have been used to detect surface species in unilluminated CO_2R.[17,82] An ATR-FTIR spectrometer is available in our lab, and we have designed, fabricated, and tested a preliminary PEC ATR-FTIR cell for CO_2R over a silver thin film deposited over a Si ATR crystal. The cell incorporates electrolyte circulation via peristaltic pump to maintain the supply of CO_2 at the surface of the electrode and provide flow cooling (Figure 6.1).

While Ge provides a wider window of IR-transparency than Si, our initial observations indicate that Ag films deposited on the latter are substantially more stable during electrolysis measurements. Surface CO_2, H_2O, CO, hydroxyl ($-OH$) groups, and hydrogen atoms have been detected during operando CO_2R ATR-FTIR spectroscopy in the window of IR transparency for Si.[82] Any change in surface species between illuminated and unilluminated conditions could indicated that plasmonic excitation promotes the selective adsorption, desorption, or generation of particular species.

Bibliography

1. Stocker, T. F., Qin, D., Plattner, G.-K., Tignor, M. M. B., Allen, S. K., Boschung, J., Nauels, A., Xia, Y., Bex, V., Midgley, P. M., Eds. Climate Change 2013: The Physical Science Basis. In *The Fifth Assessment Report of the Intergovernmental Panel on Climate Change*; IPCC, Cambridge University Press: Cambridge, 2013.

2. Hori, Y. Electrochemical CO_2 reduction on metal electrodes. In *Modern Aspects of Electrochemistry*; Vayenas, C. G., White, R. E., Eds.; Springer, 2008; Vol. 42.

3. Kuhl, K. P.; Cave, E. R.; Abram, D. N.; Jaramillo, T. F. New insights into the electrochemical reduction of carbon dioxide on metallic copper surfaces. *Energy Environ. Sci.* **2012**, *5*, 7050–7059.

4. Rumble, J. R., Ed. *CRC Handbook of Chemistry and Physics*, 98th ed.; CRC Press/Taylor & Francis: Boca Raton, FL., 2018; p 2712.

5. Ooka, H.; Figueiredo, M. C.; Koper, M. T. Competition between hydrogen evolution and carbon Dioxide reduction on copper electrodes in mildly acidic media. *Langmuir* **2017**, *33*, 9307–9313.

6. Wagman, D. D.; Evans, W. H.; Parker, V. B.; Schumm, R. H.; Halow, I.; Bailey, S. M.; Churney, K. L.; Nuttall, R. L. The NBS tables of chemical thermodynamic properties - selected values for inorganic and C_1 and C_2 organic-substances in si units. *J. Phys. Chem. Ref. Data* **1982**, *11*.

7. Kortlever, R.; Shen, J.; Schouten, K. J. P.; Calle-Vallejo, F.; Koper, M. T. M. Catalysts and reaction pathways for the electrochemical reduction of carbon dioxide. *J. Phys. Chem. Lett.* **2015**, *6*, 4073–4082.

8. Shi, C.; Chan, K.; Yoo, J. S.; Norskov, J. K. Barriers of electrochemical CO_2 reduction on transition metals. *Org. Process Res. Dev.* **2016**, *20*, 1424–1430.

9. Kuhl, K. P.; Hatsukade, T.; Cave, E. R.; Abram, D. N.; Kibsgaard, J.; Jaramillo, T. F. Electrocatalytic conversion of carbon dioxide to methane and methanol on transition metal surfaces. *J. Am. Chem. Soc.* **2014**, *136*, 14107–14113.

10. Hatsukade, T.; Kuhl, K. P.; Cave, E. R.; Abram, D. N.; Jaramillo, T. F. Insights into the electrocatalytic reduction of CO_2 on metallic silver surfaces. *Phys. Chem. Chem. Phys.* **2014**, *16*, 13814–13819.

11. Yu, S.; Wilson, A. J.; Kumari, G.; Zhang, X.; Jain, P. K. Opportunities and challenges of solar-energy-driven carbon dioxide to fuel conversion with plasmonic catalysts. *ACS Energy Lett.* **2017**, *2*, 2058–2070.

12. Mukherjee, S.; Zhou, L.; Goodman, A. M.; Large, N.; Ayala-Orozco, C.; Zhang, Y.; Nordlander, P.; Halas, N. J. Hot-electron-induced dissociation of H_2 on gold nanoparticles supported on SiO_2. *J. Am. Chem. Soc.* **2014**, *136*, 64–67.

13. Thomann, I.; Pinaud, B. A.; Chen, Z.; Clemens, B. M.; Jaramillo, T. F.; Brongersma, M. L. Plasmon enhanced solar-to-fuel energy conversion. *Nano Lett.* **2011**, *11*, 3440–6.

14. Lee, J.; Mubeen, S.; Ji, X.; Stucky, G. D.; Moskovits, M. Plasmonic photoanodes for solar water splitting with visible light. *Nano Lett.* **2012**, *12*, 5014–5019.

15. Ingram, D. B.; Linic, S. Water splitting on composite plasmonic-metal/semiconductor photoelectrodes: Evidence for selective plasmon-induced formation of charge carriers near the semiconductor surface. *J. Am. Chem. Soc.* **2011**, *133*, 5202–5205.

16. Hou, W.; Hung, W. H.; Pavaskar, P.; Goeppert, A.; Aykol, M.; Cronin, S. B. Photo-catalytic conversion of CO_2 to hydrocarbon fuels via plasmon-enhanced absorption and metallic interband transitions. *ACS Catal.* **2011**, *1*, 929–936.

17. Kumari, G.; Zhang, X.; Devasia, D.; Heo, J.; Jain, P. K. Watching visible light-driven CO_2 reduction on a plasmonic nanoparticle catalyst. *ACS Nano* **2018**, *12*, 8330–8340.

18. Gurnett, D.; Bhattacharjee, A. *Introduction to Plasma Physics with Space and Laboratory Applications*; Cambridge University Press: Cambridge, 2005.

19. Kreibig, U.; Vollmer, M. Optical Properties of Metal Clusters. In *Springer*; Toennies, J. P., Ed.; Springer, 1995.

20. Maier, S. A. *Plasmonics: Fundamentals and Applications*; Springer: New York, 2007.

21. Centeno, A.; Xie, F.; Breeze, J.; Alford, N. Calculations of scattering and absorption efficiencies of nobel metal nanoparticles. *2011 IEEE Appl. Electromagn. Conf.* **2011**,

22. Sönnichsen, C.; Franzl, T.; Wilk, T.; von Plessen, G.; Feldmann, J.; Wilson, O.; Mulvaney, P. Drastic reduction of plasmon damping in gold nanorods. *Phys. Rev. Lett.* **2002**, *88*, 077402.

23. Clavero, C. Plasmon-induced hot-electron generation at nanoparticle/metal-oxide interfaces for photovoltaic and photocatalytic devices. *Nat. Photonics* **2014**, *8*, 95–103.

24. Mott, N. The electrical conductivity of transition metals. *Proc. R. Soc. London A* **1936**, *153*, 699–717.

25. Thomas, K. G.; Zajicek, J.; Kamat, P. V. Surface binding properties of tetraoctylammonium bromide-capped gold nanoparticles. *Langmuir* **2002**, *18*, 3722–3727.

26. Linic, S.; Christopher, P.; Ingram, D. B. Plasmonic-metal nanostructures for efficient conversion of solar to chemical energy. *Nat. Mater.* **2011**, *10*, 911–921.

27. Lu, X.; Rycenga, M.; Skrabalak, S. E.; Wiley, B.; Xia, Y. Chemical synthesis of novel plasmonic nanoparticles. *Annu. Rev. Phys. Chem.* **2009**, *60*, 167–192.

28. Linic, S.; Aslam, U.; Boerigter, C.; Morabito, M. Photochemical transformations on plasmonic metal nanoparticles. *Nat. Mater.* **2015**, *14*, 567–576.

29. Xiang, C.; Walczak, K.; Haber, J.; Jones, R.; Beeman, J. W.; Guevarra, D.; Karp, C.; Liu, R.; Shaner, M.; Sun, K.; West, W.; Zhou, L. Prototyping Development of Integrated Solar-driven Water-splitting Cells. In *Integrated Solar Fuel Generators*; The Royal Society of Chemistry, 2018; Chapter 11, pp 389–453.

30. Döscher, H.; Geisz, J. F.; Deutsch, T. G.; Turner, J. A. Sunlight absorption in water efficiency and design implications for photoelectrochemical devices. *Energy Environ. Sci.* **2014**, *7*, 2951–2956.

31. Corson, E. R.; Creel, E. B.; Kim, Y.; Urban, J. J.; Kostecki, R.; McCloskey, B. D. A temperature-controlled photoelectrochemical cell for quantitative product analysis. *Rev. Sci. Instrum.* **2018**, *89*, 055112.

32. Zavarine, I. S.; Kubiak, C. P. A versatile variable temperature thin layer reflectance spectroelectrochemical cell. *J. Electroanal. Chem.* **2001**, *495*, 106–109.

33. Tao, F. F.; Salmeron, M. In situ studies of chemistry and structure of materials. *Science* **2011**, *331*, 171–174.

34. Creel, E. E. B.; Corson, E. R. E.; Eichhorn, J.; Kostecki, R.; Urban, J. J.; McCloskey, B. B. D. Directing selectivity of electrochemical carbon dioxide reduction using plasmonics. *ACS Energy Lett.* **2019**, *4*, 1098–1105.

35. Hodnik, N.; Dehm, G.; Mayrhofer, K. J. Importance and challenges of electrochemical in situ liquid cell electron microscopy for energy conversion research. *Acc. Chem. Res.* **2016**, *49*, 2015–2022.

36. Lobaccaro, P.; Singh, M. R.; Clark, E. L.; Kwon, Y.; Bell, A. T.; Ager, J. W. Effects of temperature and gas-liquid mass transfer on the operation of small electrochemical cells for the quantitative evaluation of CO_2 reduction electrocatalysts. *Phys. Chem. Chem. Phys.* **2016**, *18*, 26777–26785.

37. Hori, Y.; Kikuchi, K.; Murata, A.; Suzuki, S. Production of methane and ethylene in electrochemical reduction of carbon dioxide at copper electrode in aqueous hydrogencarbonate solution. *Chem. Lett.* **1986**, 897–898.

38. Azuma, M.; Hashimoto, K.; Hiramoto, M.; Watanabe, M.; Sakata, T. Carbon dioxide reduction at low temperature on various metal electrodes. *J. Electroanal. Chem. Interfacial Electrochem.* **1989**, *260*, 441–445.

39. Azuma, M.; Hashimoto, K.; Hiramoto, M.; Watanabe, M.; Sakata, T. Electrochemical reduction of carbon dioxide on various metal electrodes in low-temperature aqueous KHCO$_3$ media. *J. Electrochem. Soc.* **1990**, *137*, 1772–1778.

40. Kudo, A. Electrochemical reduction of high pressure CO$_2$ on Ni electrodes. *J. Electrochem. Soc.* **2006**, *140*, 1541–1545.

41. Kaneco, S.; Iiba, K.; Ohta, K.; Mizuno, T.; Saji, A. Electrochemical reduction of CO$_2$ on Au in KOH + methanol at low temperature. *Electrochim. Acta* **1998**, *441*, 215–220.

42. Mizuno, T.; Ohta, K.; Sasaki, A.; Akai, T.; Hirano, M.; Kawabe, A. Effect of temperature on electrochemical reduction of high-pressure CO$_2$ with In, Sn, and Pb electrodes. *Energy Sources* **1995**, *17*, 503–508.

43. Dettmer-Wilde, K.; Engewald, W. Theory of Gas Chromatography. In *Practical Gas Chromatography: A Comprehensive Reference*; Dettmer-Wilde, K., Engewald, W., Eds.; Springer: Berlin, 2014; Chapter 2, pp 21–57.

44. Sundararaman, R.; Narang, P.; Jermyn, A. S.; Goddard III, W. A.; Atwater, H. A. Theoretical predictions for hot-carrier generation from surface plasmon decay. *Nat. Commun.* **2014**, *5*, 5788.

45. Vreeland, E. C.; Watt, J.; Schober, G. B.; Hance, B. G.; Austin, M. J.; Price, A. D.; Fellows, B. D.; Monson, T. C.; Hudak, N. S.; Maldonado-Camargo, L.; Bohorquez, A. C.; Rinaldi, C.; Huber, D. L. Enhanced nanoparticle size control by extending LaMer's mechanism. *Chem. Mater.* **2015**, *27*, 6059–6066.

46. Alonso, C. The evaluation of surface diffusion coefficients of gold and platinum atoms at electrochemical interfaces from combined STM-SEM imaging and electrochemical techniques. *J. Electrochem. Soc.* **1990**, *137*, 2161–2166.

47. Kale, M. J.; Avanesian, T.; Christopher, P. Direct photocatalysis by plasmonic nanostructures. *ACS Catal.* **2014**, *4*, 116–128.

48. Brongersma, M. L.; Halas, N. J.; Nordlander, P. Plasmon-induced hot carrier science and technology. *Nat. Nanotechnol.* **2015**, *10*, 25–34.

49. Aslam, U.; Rao, V. G.; Chavez, S.; Linic, S. Catalytic conversion of solar to chemical energy on plasmonic metal nanostructures. *Nat. Catal.* **2018**, *1*, 656–665.

50. Linic, S.; Christopher, P.; Ingram, D. B. Plasmonic-metal nanostructures for efficient conversion of solar to chemical energy. *Nat. Mater.* **2011**, *10*, 911–921.

51. Boerigter, C.; Aslam, U.; Linic, S. Mechanism of charge transfer from plasmonic nanostructures to chemically attached materials. *ACS Nano* **2016**, *10*, 6108–6115.

52. Boerigter, C.; Campana, R.; Morabito, M.; Linic, S. Evidence and implications of direct charge excitation as the dominant mechanism in plasmon-mediated photocatalysis. *Nat. Commun.* **2016**, *7*, 10545.

53. Ho, W. Reactions at metal surfaces induced by femtosecond lasers, tunneling electrons, and heating. *J. Phys. Chem.* **1996**, *100*, 13050–13060.

54. Bard, A. J.; Faulkner, L. R. *Electrochemical Methods: Fundamentals and Applications*, 2nd ed.; John Wiley & Sons, Inc.: New York, 2001.

55. Qian, K.; Sweeny, B. C.; Johnston-Peck, A. C.; Niu, W.; Graham, J. O.; DuChene, J. S.; Qiu, J.; Wang, Y.-C.; Engelhard, M. H.; Su, D.; Stach, E. a.; Wei, W. D. Surface plasmon-driven water reduction: gold nanoparticle size matters. *J. Am. Chem. Soc.* **2014**, *136*, 9842–5.

56. Cao, G.; Wang, Y. *Nanostructures and Nanomaterials: Synthesis, Properties, and Applications*, 2nd ed.; World Scientific Publishing Co. Pte. Ltd.: Hackensack, NJ, 2011; pp 68–69.

57. Shevchenko, E. V.; Talapin, D. V.; Schnablegger, H.; Kornowski, A.; Festin, O.; Svedlindh, P.; Haase, M.; Weller, H. Study of nucleation and growth in the organometallic synthesis of magnetic alloy nanocrystals: the role of nucleation rate in size control of $CoPt_3$ nanocrystals. *J. Am. Chem. Soc.* **2003**, *125*, 9090–9101.

58. Fang, C.; Jia, H.; Chang, S.; Ruan, Q.; Wang, P.; Chen, T.; Wang, J. (Gold core)/(titania shell) nanostructures for plasmon-enhanced photon harvesting and generation of reactive oxygen species. *Energy Environ. Sci.* **2014**, *7*, 3431–3438.

59. Shen, C.; Hui, C.; Yang, T.; Xiao, C.; Tian, J.; Bao, L.; Chen, S.; Ding, H.; Gao, H. Monodisperse noble-metal nanoparticles and their surface enhanced Raman scattering properties. *Chem. Mater.* **2008**, *20*, 6939–6944.

60. Zhang, Q.; Cobley, C.; Au, L.; Mckiernan, M.; Schwartz, A.; Wen, L.-p.; Chen, J.; Xia, Y. Production of Ag nanocubes on a scale of 0.1 g per batch by protecting the NaHS-mediated polyol synthesis with argon. *Appl. Mater. Interfaces* **2009**, *1*, 2044–2048.

61. Peng, S.; McMahon, J. M.; Schatz, G. C.; Gray, S. K.; Sun, Y. Reversing the size-dependence of surface plasmon resonances. *Proc. Natl. Acad. Sci.* **2010**, *107*, 14530–14534.

62. Agnihotri, S.; Mukherji, S.; Mukherji, S. Size-controlled silver nanoparticles synthesized over the range $5 - 100$ nm using the same protocol and their antibacterial efficacy. *RSC Adv.* **2014**, *4*, 3974–3983.

63. Shein, J. B.; Lai, L. M. H.; Eggers, P. K.; Paddon-Row, M. N.; Gooding, J. J. Formation of efficient electron transfer pathways by adsorbing gold nanoparticles to self-assembled monolayer modified electrodes. *Langmuir* **2009**, *25*, 11121–11128.

64. Hamoudi, H.; Guo, Z. A.; Prato, M.; Dablemont, C.; Zheng, W. Q.; Bourguignon, B.; Canepa, M.; Esaulov, V. A. On the self assembly of short chain alkanedithiols. *Phys. Chem. Chem. Phys.* **2008**, *10*, 6836–6841.

65. Love, J. C.; Estroff, L. A.; Kriebel, J. K.; Nuzzo, R. G.; Whitesides, G. M. Self-assembled monolayers of thiolates on metals as a form of nanotechnology. **2005**, *105*, 1103–1169.

66. Zarkadas, G. M.; Stergiou, A.; Papanastasiou, G. Silver electrodeposition from AgNo3solutions containing organic additives: Electrodeposition from binary water-methanol solvent systems in the presence of tartaric acid. *J. Appl. Electrochem.* **2004**, *34*, 607–615.

67. Parthasarathy, A.; Srinivasan, S.; Appleby, A. J.; Martin, C. R. Electrode kinetics of oxygen reduction at carbon-supported and unsupported platinum microcrystallite/Nafion℗ interfaces. *J. Electroanal. Chem.* **1992**, *339*, 101–121.

68. Xing, S.; Xu, H.; Chen, J.; Shi, G.; Jin, L. Nafion stabilized silver nanoparticles modified electrode and its application to Cr(VI) detection. *J. Electroanal. Chem.* **2011**, *652*, 60–65.

69. Zhao, S.; Zhang, K.; Bai, Y.; Yang, W.; Sun, C. Glucose oxidase/colloidal gold nanoparticles immobilized in Nafion film on glassy carbon electrode: Direct electron transfer and electrocatalysis. *Bioelectrochemistry* **2006**, *69*, 158–163.

70. de Almeida, S. H.; Kawano, Y. Ultraviolet-visible spectra of Nafion membrane. *Eur. Polym. J.* **1997**, *33*, 1307–1311.

71. Hu, Y.; Liu, Y.; Sun, Y. Mesoporous colloidal superparticles of platinum-group nanocrystals with surfactant-free surfaces and enhanced heterogeneous catalysis. *Adv. Funct. Mater.* **2015**, *25*, 1638–1647.

72. Epifani, M.; Giannini, C.; Tapfer, L.; Vasanelli, L. Sol-gel synthesis and characterization of Ag and Au nanoparticles in SiO_2, TiO_2, and ZrO_2 thin films. *J. Am. Ceram. Soc.* **2004**, *83*, 2385–2393.

73. Kočí, K.; Matěj, K.; Obalová, L.; Krejčíková, S.; Lacný, Z.; Plachá, D.; Čapek, L.; Hospodková, A.; Šolcová, O. Effect of silver doping on the TiO_2 for photocatalytic reduction of CO_2. *Appl. Catal. B Environ.* **2010**, *96*, 239–244.

74. Lee, M. S.; Hong, S. S.; Mohseni, M. Synthesis of photocatalytic nanosized TiO_2-Ag particles with sol-gel method using reduction agent. *J. Mol. Catal. A Chem.* **2005**, *242*, 135–140.

75. Zhao, B.; Chen, Y. W. Ag/TiO_2 sol prepared by a solgel method and its photocatalytic activity. *J. Phys. Chem. Solids* **2011**, *72*, 1312–1318.

76. Ma, S.; Lan, Y.; Perez, G. M.; Moniri, S.; Kenis, P. J. Silver supported on titania as an active catalyst for electrochemical carbon dioxide reduction. *Chem. Sus. Chem.* **2014**, *7*, 866–874.

77. Blackstock, J. J.; Li, Z.; Jung, G. Template stripping using cold welding. *J. Vac. Sci. Technol. A Vacuum, Surfaces, Film.* **2004**, *22*, 602–605.

78. Hugall, J. T.; Finnemore, A. S.; Baumberg, J. J.; Steiner, U.; Mahajan, S. Solvent-resistant ultraflat gold using liquid glass. *Langmuir* **2012**, *28*, 1347–1350.

79. Mosley, D. W.; Chow, B. Y.; Jacobson, J. M. Solid-state bonding technique for template-stripped ultraflat gold substrates. *Langmuir* **2006**, *22*, 2437–2440.

80. Vogel, N.; Zieleniecki, J.; Köper, I. As flat as it gets: Ultrasmooth surfaces from template-stripping procedures. *Nanoscale* **2012**, *4*, 3820–3832.

81. Wang, L.; Nitopi, S. A.; Bertheussen, E.; Orazov, M.; Morales-Guio, C. G.; Liu, X.; Higgins, D. C.; Chan, K.; Nørskov, J. K.; Hahn, C.; Jaramillo, T. F. Electrochemical carbon monoxide reduction on polycrystalline copper: Effects of potential, pressure, and pH on selectivity toward multicarbon and oxygenated products. *ACS Catal.* **2018**, *8*, 7445–7454.

82. Firet, N. J.; Smith, W. A. Probing the reaction mechanism of CO_2 electroreduction over Ag films via operando infrared spectroscopy. *ACS Catal.* **2017**, *7*, 606–612.

Glossary

Notation	Description	Page List
anode	electrode where oxidation occurs	1, 2, 24, 55, 56, 91
cathode	electrode where reduction occurs	1, 2, 6, 21, 23, 24, 34, 35, 40–57, 89, 91, 92
counter electrode	electrode that provides the current balance to the working electrode	25, 26, 31, 35, 55
double layer	array of charged species and oriented dipoles at the electrode-electrolyte interface	42, 58
electrochemical cell	a device that generates electrical energy from chemical reactions or uses electrical energy to cause chemical reactions	1, 2, 19, 20, 22, 23, 34, 57, 70
electrode	the electronic conductor from which charge is passed in an electrochemical cell	4, 17–24, 26, 30–35, 42–44, 46–48, 51, 55, 58, 90
electrolyte	the ionic conducting substance that completes the electrical circuit between the anode and cathode	1, 2, 5, 17–20, 23–27, 30–33, 35, 37, 40–42, 44, 46, 49, 55, 56
Faradaic current	current caused by changes to the electrode-electrolyte interface in which charge does not cross the interface	42, 58
Faradaic efficiency	proportion of charge passed that is transferred to a particular reaction	5, 31–34, 41, 44, 46, 47, 50, 51, 54, 56, 57, 92

Notation	Description	Page List
heterogeneous catalysis	catalysis where the catalyst state of matter is different from the reactant state of matter	1
onset potential	potential at which current starts to increase due to the start of a reaction	5, 6, 46
Ostwald ripening	the dissolution of small solid colloidal particles and redeposition onto large solid colloidal particles in a liquid medium	61, 62
overpotential	additional potential beyond the thermodynamic requirement needed to drive a reaction at a certain rate	3, 5
reduction	flow of electrons from an electrode into the electrolyte	17, 21, 23, 24
reference electrode	an electrode of fixed potential relative to which the working electrode potential is observed or controlled	26, 27, 29, 31, 35, 55, 56
sinter	coalesce into a solid mass by heating without liquefaction	81
working electrode	electrode where the reaction of interest occurs	18, 23, 24, 26, 29, 31, 34, 56